UAB
Universitat Autònoma de Barcelona

Heat Transport in Layered Semiconductors

Sebin Varghese

ADVERTIMENT. L'accés als continguts d'aquesta tesi queda condicionat a l'acceptació de les condicions d'ús establertes per la següent llicència Creative Commons: https://creativecommons.org/licenses/?lang=ca

ADVERTENCIA. El acceso a los contenidos de esta tesis queda condicionado a la aceptación de las condiciones de uso establecidas por la siguiente licencia Creative Commons: https://creativecommons.org/licenses/?lang=es

WARNING. The access to the contents of this doctoral thesis it is limited to the acceptance of the use conditions set by the following Creative Commons license: https://creativecommons.org/licenses/?lang=en

Heat Transport in Layered Semiconductors

Doctoral Thesis

by

Sebin Varghese

Advisor: Prof. Klaas-Jan Tielrooij

Tutor: Prof. Javier Rodríguez Viejo









ICN2 – Institut Català de Nanociència i Nanotecnologia

BIST – Barcelona Institute of Science and Technology

UAB – Universitat Autònoma de Barcelona

TU/e – Eindhoven University of Technology

October 2024

The research work presented in this thesis was carried out between September 2019 and August 2024. This research was funded by the Spanish Ministry of Economy through the FPI-SO2018 grant and by the European Union's Horizon 2020 research and innovation program under grant agreement No. 804349 (ERC starting grant CUHL).







Thesis advisor:

Prof. Klaas-Jan Tielrooij

Thesis committee:

Prof. Dr. Stefan Dilhaire (University of Bordeaux, France)
Prof. Dr. Ilaria Zardo (University of Basel, Switzerland)
Dr. Sebastian Reparaz (ICMAB - Institut de Ciència de Materials de Barcelona, Spain)

Substitutes:

Dr. Aitor Lopeandia Fernández (Universitat Autònoma de Barcelona, Spain)
Dr. Guillermo Brinatti Vázquez (ICFO - Institut de Ciències Fotòniques, Spain)

Barcelona, 21 de Agosto, 2024

El **Prof. Klaas-Jan Tielrooij**, líder del grupo Ultrafast Dynamics in Nanoscale Systems (UDNS) del Institut Català de Nanociència i Nanotecnologia (ICN2) y profesor asociado en la Eindhoven University of Technology (TU/e), y el **Prof. Javier Rodríguez Viejo**, líder del grupo Thermal properties of Nanoscale Materials (GTNaM) del Institut Català de Nanociència i Nanotecnologia y profesor titular del departamento de física de la Universitat Autònoma de Barcelona (UAB), en calidad de tutor de tesis,

CERTIFICAN:

Que **Sebin Varghese** ha realizado bajo su dirección y tutoría el trabajo que lleva por título **"Heat Transport in Layered Semiconductors"**. Dicho trabajo ha sido desarrollado dentro del programa de doctorado de Física y constituye su memoria de tesis doctoral, para optar por el grado de doctor por la Universitat Autònoma de Barcelona (UAB).



Prof. Klaas-Jan Tielrooij
Senior Group Leader, Ultrafast Dynamics in Nanoscale Systems,
Institut Català de Nanociència i Nanotecnologia (ICN2), Spain &
Associate Professor, Applied Physics and Science Education,
Eindhoven University of Technology (TU/e), The Netherlands

Prof. Javier Rodríguez Viejo
Senior Group Leader, Thermal Properties of Nanoscale Materials,
Institut Català de Nanociència i Nanotecnologia (ICN2), Spain &
Full Professor, Department of Physics,
Universitat Autònoma de Barcelona (UAB), Spain

To Jeenamma, Appachan, and all loved ones...

ജീനാമ്മയ്ക്കും, അപ്പച്ചനും, പിന്നെ എല്ലാ സ്നേഹിതർക്കും...

"A man, after he has brushed off the dust and chips of his life, will have left only the hard, clean questions: Was it good or was it evil? Have I done well — or ill?"

— John Steinbeck, East of Eden

Abstract

It has been a longstanding goal of physicists to understand how heat flows and how it affects the thermal properties of materials. This quest has been driven not only by the pursuit of knowledge but also by the tremendous importance of heat in daily life. The discovery of new materials has introduced challenges in understanding fundamental properties such as heat transport, while also opening avenues for technological advancements.
In this thesis, we investigate the heat transport properties of a class of layered materials known as transition metal dichalcogenides (TMDs). We study these materials using two different optical techniques: the conventional technique of Raman thermometry and a novel spatiotemporal pump-probe thermometry technique that we have developed.
With this new technique, we directly quantify the in-plane thermal diffusivity in TMDs. The thermal diffusivities obtained for $MoSe_2$, down to a thickness of 3 layers, are consistent with results obtained from Raman thermometry. Interestingly, in monolayer and bilayer samples, we observe a transition in heat transport behaviour—from diffusive in thicker samples to viscous with very low diffusivity in ultrathin samples. We attribute this viscous transport to the hydrodynamic flow of heat, a phenomenon that has never been observed in TMDs at any temperature.

Resumen

Ha sido un objetivo prolongado de los físicos entender cómo fluye el calor y cómo afecta las propiedades térmicas de los materiales. Esta búsqueda ha sido impulsada no solo por la búsqueda del conocimiento, sino también por la tremenda importancia del calor en la vida diaria. El descubrimiento de nuevos materiales ha introducido desafíos en la comprensión de propiedades fundamentales como el transporte de calor, al tiempo que ha abierto avenidas para avances tecnológicos.

En esta tesis, investigamos las propiedades de transporte de calor de una clase de materiales estratificados conocidos como dicalcohenuros de metales de transición (TMDs). Estudiamos estos materiales utilizando dos técnicas ópticas diferentes: la técnica convencional de termometría Raman y una novedosa técnica de termometría de bomba-sonda espaciotemporal que hemos desarrollado.

Con esta nueva técnica, cuantificamos directamente la difusividad térmica en el plano en los TMDs. Las difusividades térmicas obtenidas para $MoSe_2$, hasta un grosor de 3 capas, son consistentes con los resultados obtenidos mediante termometría Raman. Interesantemente, en muestras de monocapa y bicapa, observamos una transición en el comportamiento del transporte de calor—de difusivo en muestras más gruesas a viscoso con una difusividad muy baja en muestras ultrafinas. Atribuimos este transporte viscoso al flujo hidrodinámico de calor, un fenómeno que nunca se ha observado en TMDs a ninguna temperatura.

Contents

Abstract vii

Resumen ix

List of publications xiv

1 Introduction 1
- 1.1 Heat transport: An overview . . . 1
  - 1.1.1 Layered materials . . . 3
  - 1.1.2 Experimental techniques . . . 4
- 1.2 This thesis . . . 5

2 Heat transport: Theoretical background 7
- 2.1 Transition metal dichalcogenides . . . 8
  - 2.1.1 Crystal structure . . . 8
  - 2.1.2 Electronic band structure of TMDs . . . 8
  - 2.1.3 Excitons in TMDs . . . 9
  - 2.1.4 Phonon band structure of TMDs . . . 11
- 2.2 Fourier description of heat transport . . . 12
  - 2.2.1 Solution to heat diffusion equation . . . 13
- 2.3 Boltzmann Transport Equation . . . 14
  - 2.3.1 Relaxation Time Approximation . . . 15
- 2.4 Phonon scattering mechanisms . . . 17
- 2.5 Thermal transport beyond Fourier . . . 18
  - 2.5.1 Ballistic phonon transport . . . 19
  - 2.5.2 Phonon hydrodynamics in Ziman regime . . . 20
  - 2.5.3 Phonon hydrodynamics in nanoscale . . . 23

3 Fabrication of suspended TMDs 25
- 3.1 Introduction . . . 26
- 3.2 Fabrication of samples . . . 26
  - 3.2.1 Preparation of PDMS and exfoliation . . . 26
  - 3.2.2 Deterministic dry transfer . . . 27
- 3.3 Characterization of the samples . . . 29
  - 3.3.1 Thickness determination . . . 30
  - 3.3.2 Roughness and crystallinity . . . 32
  - 3.3.3 Raman: Strain characterization . . . 33

3.4 Optical measurements . . . 34
3.4.1 Absorption measurements at 532 nm . . . 35
3.4.2 UV-Vis spectroscopy . . . 36
3.5 Summary . . . 37

4 Spatiotemporal pump-probe microscopy: Experimental setup 39
4.1 Experimental setup: Description and characterization . . . 40
4.1.1 General concept . . . 40
4.1.2 Experimental setup . . . 41
4.1.3 Beam overlapping and spatial scanning . . . 43
4.2 Tracking diffusion on gold . . . 49
4.3 Summary: Outlook to study heat transport . . . 50

5 Spatiotemporal thermometry: Quantifying heat diffusion in bulk TMDs 53
5.1 Introduction . . . 54
5.2 Temporal dynamics . . . 55
5.3 Emergence of long-lived signal . . . 56
5.3.1 Dependence on probe wavelength . . . 56
5.3.2 Lorentz oscillator model . . . 57
5.3.3 Estimation of temperature rise . . . 58
5.4 Spatiotemporal mapping at $\Delta t = 0$ and $\Delta t = 13$ ns . . . 60
5.5 Heat accumulation: Schematics . . . 61
5.6 Simulations: Solving Fourier's heat law . . . 62
5.7 Experimental results and comparison: Bulk TMDs . . . 64
5.8 Modulation dependent spatial profiles . . . 67
5.9 Describing in-phase and quadrature lock-in signals . . . 68
5.10 Evaluation of spatiotemporal thermometry . . . 70
5.11 Summary . . . 72

6 Raman thermometry: Steady-state heat transport down to monolayer 75
6.1 Introduction . . . 76
6.2 Raman thermometry . . . 76
6.3 Experimental results . . . 78
6.3.1 Calibration measurements . . . 78
6.3.2 Raman thermometry for varying flake thickness . . . 80
6.4 Thermal conductivity and microscopic insights . . . 81
6.5 Summary . . . 83

7 Heat transport: From diffusive to viscous 85
7.1 Introduction . . . 86
7.2 Diffusive heat transport with flake thickness, $f_{mod} = 240$ kHz . . . 87
7.2.1 Linearity with pump fluence . . . 87
7.2.2 Effect of flake thickness . . . 88
7.2.3 Comparison with Raman thermometry . . . 89
7.3 Viscous heat transport . . . 90
7.3.1 Experimental results . . . 90
7.3.2 Effective Fourier description . . . 91

7.3.3 Discussion 93
7.4 Summary 95

8 Conclusion **97**
8.1 Summary 97
8.2 Outlook 100

A Appendix **I**

Acknowledgements **VII**

Bibliography **IX**

Curriculum Vitae **XX**

List of publications

• **S. Varghese**, D. Saleta Reig, J. D. Mehew, A. Block, A. El Sachat, E. Chavez-Angel, M. Sledzinska, B. Ballesteros, C. M. S. Torres, and K. J. Tielrooij. "Fabrication and characterization of large-area suspended $MoSe_2$ crystals down to the monolayer". Journal of Physics: Materials. 4(4), 046001, 2021, see Chapter 3.

• **S. Varghese**, J. D. Mehew, A. Block, D. Saleta Reig, P. Woźniak, R. Farris, Z. Zanolli, P. Ordejón, M. J. Verstraete, N. F. van Hulst, and K. J. Tielrooij. "A pre-time-zero spatiotemporal microscopy technique for the ultrasensitive determination of the thermal diffusivity of thin films". Review of Scientific Instruments, 94, 034903, 2023, see Chapter 5.

• D. Saleta Reig, **S. Varghese**, R. Farris, A. Block, J. D. Mehew, O. Hellman, P. Woźniak, M. Sledzinska, A. El Sachat, E. Chávez-Ángel, S. O. Valenzuela, N. F. van Hulst, P. Ordejón, Z. Zanolli, C. M. S. Torres, M. J. Verstraete, and K. J. Tielrooij. "Unraveling heat transport and dissipation in suspended $MoSe_2$ from bulk to monolayer". Advanced Materials, 34(10), 2108352, 2022, see Chapter 6.

• **S. Varghese**, J. Tur Prats, J. D. Mehew, D. Saleta Reig, R. Farris, J. Camacho, J. A. Haibeh, A. Sokolov, P. Ordejón, S. Huberman, A. Beardo, F. X. Alvarez, and K. J. Tielrooij. "Non-diffusive heat transport in ultrathin layered semiconductors at room temperature". *In preparation*, see Chapter 7.

• V. Babacic, D. Saleta Reig, **S. Varghese**, T. Vasileiadis, E. Coy, K. J. Tielrooij, and B. Graczykowski. "Thickness-dependent elastic softening of few-layer free-standing $MoSe_2$". Advanced Materials, 33(23), 2170179, 2021

• K. J. Tielrooij, A. Principi, D. Saleta Reig, A. Block, **S. Varghese**, S. Schreyeck, K. Brunner, G. Karczewski, I. Ilyakov, O. Ponomaryov, T. VAG de Oliveira, M. Chen, J. C. Deinert, C. Gomez Carbonell, S. O. Valenzuela, L. W. Molenkamp, T. Kiessling, G. V. Astakhov, and S. Kovalev. "Milliwatt terahertz harmonic generation from topological insulator metamaterials". Light: Science and Applications, 11, 315, 2022

• A. Block, R. Yu, I. W. Un, **S. Varghese**, M. Liebel, N. F. van Hulst, S. Fan, K. J. Tielrooij, and Y. Sivan. "Observation of negative effective thermal diffusion in gold films". ACS Photonics, 10(4), 1150-1158, 2023

• F. Morabito, K. Synnatschke, J. D. Mehew, **S. Varghese**, C. J. Sayers, G. Folpini, A. Petrozza, G. Cerullo, K. J. Tielrooij, J. Coleman, V. Nicolosi, C. Gadermaier. "Long lived photogenerated charge carriers in few-layer transition metal dichalcogenides obtained from liquid phase exfoliation". Nanoscale Advances, 6, 1074-1083, 2024

• R. Farris, O. Hellman, Z. Zanolli, D. Saleta Reig, **S. Varghese**, P. Ordejón, K. J. Tielrooij, and M. J. Verstraete. "Microscopic understanding of the in-plane thermal transport properties of 2H transition metal dichalcogenides". Physical Review B, 109, 125422, 2024

• **S. Varghese**, J. D. Mehew, H. I. Wang, M. Wuttke, Y. Zhou, K. Müllen, A. Narita, A. W. Cummings, and K. J. Tielrooij. "Ultrafast charge and exciton diffusion in monolayer films of 9-armchair graphene nanoribbons". *Under Review*

1
Introduction

"Somewhere, something incredible is waiting to be known." - Carl Sagan

1.1 Heat transport: An overview

Heat is energy in transfer from one physical system to another or from one region within a physical system to another, driven by a temperature difference. It is an integral part of our daily lives and the universe at large. Heat influences many natural processes, fuels our homes, cooks our food, and powers our industries. From the warmth of a summer's day to the chill of a winter's night, from the steam rising from a hot cup of coffee to the cold air on a snowy day, heat is everywhere.

Consider a metal rod that is uniformly heated at one end. Over time, heat diffuses through the metal rod, spreading from the hotter end to the cooler regions. This process continues until the temperature gradient along the rod diminishes and the heat is evenly distributed within the metal rod. A similar process occurs when a metal spoon in a hot soup becomes warm as heat diffuses from the soup into the spoon. In industries, the principle of heat diffusion is harnessed in various ways to manage thermal energy. For instance, in electronics and semiconductor manufacturing, managing heat diffusion is crucial to maintaining device performance and reliability. Thermal management solutions, such as heat sinks and thermal interface materials, are employed to efficiently dissipate heat from electronic components, preventing overheating and ensuring optimal functionality.



Figure 1.1: Schematic representation of heat flowing from hot to cold region.

Heat transport, a problem that has intrigued scientists for centuries, is a process that

can occur through conduction, convection, and radiation. Newton provided the earliest understanding of heat flow with his law of cooling, which describes how the temperature changes in an object due to heat exchange with its environment [1]. In the early 19th century, Fourier expanded this understanding with his mathematical description of heat conduction, stating that the rate of heat transfer through a material is proportional to the temperature difference across it and the area through which heat is transferred, meaning that heat flows from regions of higher temperature to regions of lower temperature (see Figure 1.1). This principle, known as Fourier's law [2], provided a robust mathematical framework for analyzing heat flow in solids. A few decades later, Fick discovered that the movement of salt in water, driven by the random motion of molecules [3], follows the same principles as Fourier's law of heat conduction. This analogy between heat and mass transport highlighted the fundamental principles governing both phenomena, paving the way for understanding how heat in solids can be transported by the random motion of microscopic particles.

The kinetic theory of gases later provided a microscopic description of heat transport, explaining how the random motion of particles drives diffusion [4], a principle that applies not just to gases but also to liquids and solids. This theory forms the basis for our understanding of how individual particles move and interact, and how their collective behaviour results in heat transport. Finally, in the early 20th century, Einstein provided a statistical description of Brownian motion—the random motion of particles suspended in a fluid [5]. Einstein demonstrated that this random motion at the microscopic level leads to macroscopic diffusion, effectively bridging the gap between the statistical mechanics of microscopic particles and the macroscopic description of heat transport.

The general picture is as follows: In metallic solids, free electrons are the main carriers of heat, and they obey Fermi-Dirac statistics. In contrast, in non-metallic solids, heat is primarily transported by phonons, which are quantized lattice vibrations that follow Bose-Einstein statistics. Both phonons and electrons in most situations travel an average distance, known as the mean free path before they scatter [6]. This scattering can occur between phonons themselves, between electrons, at the boundaries of the material, with impurities, defects, and dislocations within the material, or due to isotope scattering. When the mean free path is relatively short compared to the system size, frequent collisions ensure that Fourier's law of heat conduction can accurately describe the heat transport.

However, there are situations in which the classical framework of Fourier's law does not hold. This can happen, for example, in nanoscale systems and novel materials such as carbon nanotubes, nanowires, and two-dimensional (2D) materials like graphene [7]. This is primarily due to the effects of nanoscale confinement, where the mean free path of heat carriers becomes comparable to or larger than the size of the system itself, as well as the

dominance of momentum-conserving normal scattering in these material systems. This has led to the observation of new phenomena in thermal transport. For example, in ballistic transport [8], heat carriers move through the material without scattering, whereas in hydrodynamic transport [9], the collective behaviour of heat carriers becomes the dominant mechanism of heat transport. While significant strides have been made in studying these materials, our understanding of heat transport in them is still evolving, and they continue to be an active area of research.

1.1.1 Layered materials

A layered material can be broadly defined as any material where the atoms within each layer are strongly bonded by covalent forces, while the adjacent layers are held together by weak van der Waals forces. This unique bonding allows for the mechanical exfoliation of individual layers, a breakthrough achieved with graphene in 2004 [10]. The ability to isolate such thin layers has facilitated the exploration of their properties at the atomic scale. For example, graphene, a semimetal, exhibit exceptional properties including high carrier mobility [11], remarkable tensile strength [12], and superior thermal conductivity [13]. These attributes enable graphene to be utilized in a variety of applications, including photodetectors [14, 15], energy storage [16, 17], and more [18]. The rapid and prosperous development of graphene has spurred significant interest in other layered materials, each with unique properties. This diverse class includes insulators (hBN), semiconductors (MoS_2), half-metals (CrO_2), metals (VO_2), and superconductors ($NbSe_2$) (see Figure 1.2).

In this broad category of layered materials, transition metal dichalcogenides (TMDs) have gained considerable interest over the past decade. Despite the relatively modest mobility of about 200 $cm^2/V/s$ [19, 20] reported for these materials, compared to that of 200,000 $cm^2/V/s$ for graphene [21] at room temperature, TMDs exhibit fascinating electro-optical properties. Notably, TMDs exhibit a direct bandgap in their monolayer form [22, 23], which differs from their bulk counterparts. This direct bandgap, coupled with the presence of excitons with large binding energies, leads to strong light emission. These properties make TMDs particularly promising for various optoelectronic applications, such as photodetectors and light-emitting devices [24–27].

Among the most promising applications of TMDs is transistor technology. TMD-based transistors [19] benefit from a high on/off ratio and low subthreshold swing, critical factors for enhancing the performance and energy efficiency of electronic circuits. Their ability to be scaled down to atomic thickness allows for significant miniaturization of transistors, pushing the boundaries of Moore's Law [29] and facilitating the development of more

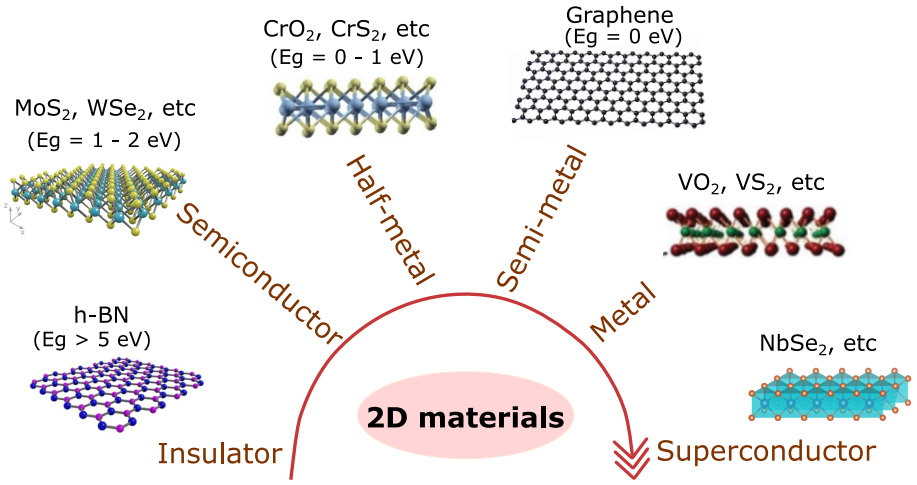


Figure 1.2: An overview of the 2D-materials family. Eg: band gap. Adapted from Ref. [28].

compact and efficient electronic components.

IMEC, a prominent nanoelectronics research institute, has highlighted the role of layered materials, including TMDs, in their roadmap for scaling down the dimensions of the transistors [30]. This roadmap emphasizes the necessity of integrating these materials to achieve better performance and energy efficiency in semiconductor devices. While optoelectronic properties of the TMDs have been rigorously studied over the last years, we lack a comprehensive understanding of heat transport in these materials. Moreover given their technological relevance, it is essential to study and understand their thermal properties.

1.1.2 Experimental techniques

Several electrical and optical experimental techniques have been developed to measure the thermal transport properties of thin films. Electrical methods include AC calorimetry [31], 3ω [32], and micro heater [33] techniques. These often require nanofabrication of heaters and thermometers near the thin film or metal electrodes contacting the material. Scanning thermal microscopy, which measures temperature variations with a nanoscale thermal probe, provides higher spatial resolution [34, 35] but has limitations such as slow data acquisition and nontrivial analysis [36].

Optical methods are often preferred for thin films due to their non-invasive, contact-free nature. Steady-state Raman spectroscopy, for instance, is widely used to determine the thermal conductivity [13, 37]. This method involves locally heating a sample and monitoring the Raman frequency shift to obtain the thermal conductivity. Despite requiring strong heating and precise calibration, it has been applied to various thin films, including silicon membranes, nanotubes, and 2D materials [38, 39].

Transient pump-probe techniques, such as time-domain thermoreflectance [40] and frequency-domain thermoreflectance [41], measure the thermal properties of thin films and interfaces. In these methods, a pump pulse deposits heat into a metal transducer, and a probe pulse monitors the cooling dynamics by measuring changes in the reflectance of the transducer. The thermal properties are obtained by analyzing these cooling dynamics, typically using a complicated heat transport model [36, 42].
Transient thermal grating (TTG) is another optical technique used to measure thermal and acoustic properties [43]. Two laser pulses create a sinusoidal interference pattern on the sample plane, producing a thermal grating. Analyzing the decay of various grating periods allows for the quantification of the thermal diffusivity. TTG can measure diffusivities across various materials [44], although its application is limited to large-area samples due to the required laser spot sizes.
Despite the widespread use of various electrical and optical methods to investigate heat transport properties, there is currently no technique that combines the following features: (i) minimal sample fabrication (ii) contactless measurements, (iii) sensitivity to small temperature changes (less than 10 K), (iv) mathematical modelling with no material input parameters, (v) high spatial and temporal resolution, and (vi) applicability to small (micron-sized) samples.
This PhD thesis is motivated by the need for a technique that combines all these advantages to measure the heat transport properties of thin films, and by the limited understanding of heat transport mechanisms in layered semiconductors. Given the pivotal role of layered materials in next-generation technological applications, it is crucial to thoroughly quantify their thermal transport properties.

1.2 This thesis

- In Chapter 2, we introduce the fundamental concepts of heat diffusion in solids, providing an overview of the theoretical framework and the intuitive concepts required to follow the experimental observations.
- Following that, in Chapter 3, we provide a detailed account of the fabrication process for suspended TMD flakes using a custom-built dry-transfer stage, followed by a comprehensive characterization of these samples.
- Chapter 4 explores the foundational components of spatiotemporal pump-probe microscopy employed in our experiments. We explain the fundamental concept and provide detailed insights into several important measurement procedures, including beam overlap in both spatial and temporal domains, for precise heat transport

measurements. As a demonstration of feasibility, we present the analysis of spatiotemporal diffusion dynamics in gold.

- Subsequently, in Chapter 5, we demonstrate the strength of our spatiotemporal pump-probe thermometry technique by using it to determine the thermal diffusivity of layered semiconductors. In particular, we quantify the thermal diffusivity of four prototypical TMDs.
- Next, in Chapter 6, we employ Raman thermometry to systematically study the in-plane thermal conductivity of $MoSe_2$ starting from bulk down to the monolayer limit. Our experiments reveal that the thermal conductivity does not change much with thickness — less than a factor of two between the bulk and the monolayer case, which is further explained by *ab initio* calculations.
- In Chapter 7, we study the thickness dependence of thermal diffusivity in $MoSe_2$ and MoS_2 using spatiotemporal pump-probe thermometry. Notably, we observe a dramatic reduction in thermal diffusivity for ultrathin $MoSe_2$ and MoS_2 at room temperature, which we attribute to hydrodynamic heat transport.
- Finally, in Chapter 8, we provide a brief summary of this thesis and an outlook for potential future developments based on these findings.

2

Heat transport: Theoretical background

"If I have seen further, it is by standing upon the shoulders of giants".
- Sir Issac Newton

This chapter introduces the general topic of heat transport in solids. We briefly overview the crystal structure, electronic band structure, and phonon band structure of transition metal dichalcogenides (TMDs). We then discuss the fundamental physics of heat transport via diffusion at the macroscopic level, presenting solutions for the diffusion equation with an initial Gaussian heat source. Following this, we briefly explain the microscopic theory (phonon kinetic theory), specifically the Boltzmann transport equation, and phonon scattering mechanisms. Finally, we discuss the non-diffusive transport phenomena, including ballistic and hydrodynamic heat transport mechanisms.

Acknowledgements: I heartily acknowledge Dr Albert Beardo from the University of Colorado Boulder for the invaluable discussions and assistance while writing this thesis chapter. I also thank Dr Roberta Farris from the Institut Català de Nanociència i Nanotecnologia for providing the calculated data for plotting the $MoSe_2$ phonon band structure in Figure 2.4.

2.1 Transition metal dichalcogenides

2.1.1 Crystal structure

A typical TMD, MX_2, is depicted in Figure 2.1, where M represents a transition metal (M = Mo, W, etc.) and X represents a chalcogen (X = S, Se, etc.) atom. The lattice structure consists of triangular lattices, with the metal atom positioned between two chalcogen atoms. From an out-of-plane perspective, the system exhibits a hexagonal lattice similar to graphene, but a monolayer consists of three atomic planes, resulting in a thickness of approximately 0.7 nm. The bonds within the M-X layer are covalent, while MX_2 layers are weakly coupled by van der Waals forces. In this system, the metal and chalcogen atoms are arranged in different coordinations, with the most common being trigonal (with hexagonal symmetry H) and octahedral (with tetragonal symmetry T), as shown in Figure 2.1 [45].

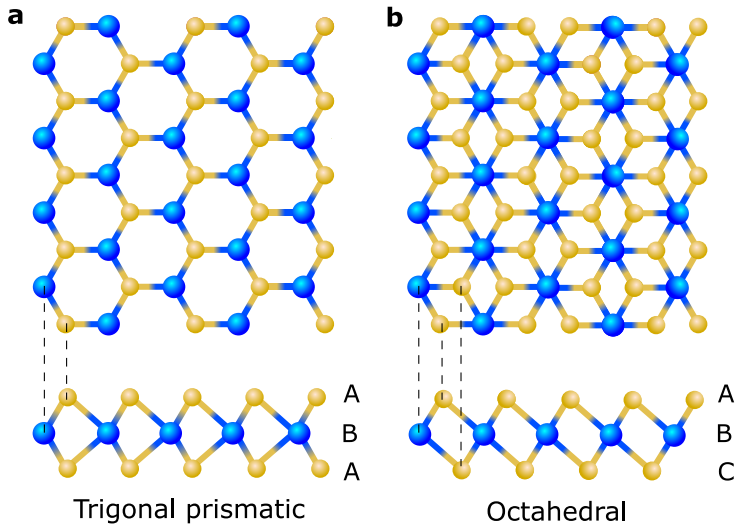


Figure 2.1: TMD crystal structure. (a) Trigonal and **(b)** octahedral atomic coordination as viewed out-of-plane (top) and in-plane (bottom). Transition metal atoms are in blue, chalcogen atoms are in yellow. Adapted from Ref. [45].

2.1.2 Electronic band structure of TMDs

In bulk TMDs, the electronic band structure typically exhibits an indirect band gap. For example, in bulk $MoSe_2$, the valence band maximum (VBM) is at the Γ point, while the conduction band minimum (CBM) is located between the Γ and K points (see Figure 2.2a). This indirect band gap results in less efficient optical transitions because the electron transition requires a change in momentum, involving a phonon, which reduces the probability of these transitions. However, when TMDs are thinned down to a monolayer,

significant changes occur in the band structure. Monolayer TMDs display a direct band gap [22, 23] at the K point in the Brillouin zone because they have both their VBM and CBM located at the K point (see Figure 2.2b).

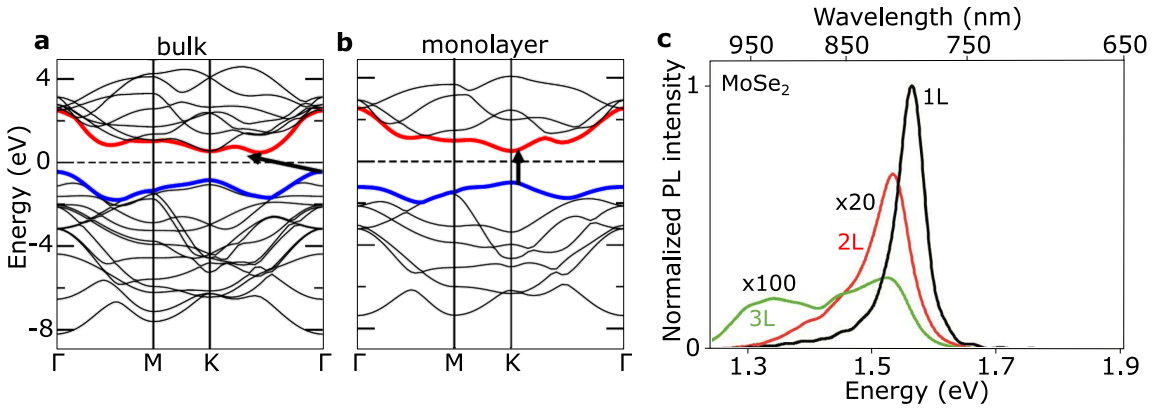


Figure 2.2: Electronic band structure and PL. **(a, b)** Electronic band structure of (a) bulk and (b) monolayer $MoSe_2$ (from Ref. [46]). **(c)** Photoluminescence spectra for mono, bi and trilayer $MoSe_2$. Reprinted/Adapted with permission from Ref. [47].

The main consequence of transitioning from an indirect to a direct band gap is a significant increase in photoluminescence (PL) emission efficiency. This arises because the lowest energy transition can now occur without needing to interact with a phonon to satisfy momentum conservation. Consequently, the PL intensity of monolayer TMDs is greatly enhanced compared to bilayer or thicker samples. This enhancement is depicted in Figure 2.2c, showing the PL spectra of monolayer, bilayer, and trilayer $MoSe_2$. This strong coupling to light makes monolayer TMDs highly desirable for optoelectronic applications [24].

2.1.3 Excitons in TMDs

The absorption of a photon with energy above the bandgap in a TMD results in creating an electron-hole pair. Through the attractive Coulomb interaction between the electron and the hole, they can combine to form a bound state known as an exciton. In TMDs, the reduced dimensionality and weak screening give rise to a notably strong Coulomb interaction, leading to the formation of tightly bound excitons that remain stable even at room temperature [48]. The strong Coulomb interaction results in a high exciton binding energy (typically $0.5 - 1.1$ eV for monolayers) [49], which is the energy required to dissociate the exciton into a free electron and hole. This high binding energy also means that the optical bandgap, defined as the energy of the excitonic transition, is lower than the electronic bandgap, which is the energy difference between the conduction band minimum and the valence band maximum.

In TMDs, strong spin-orbit coupling causes both the conduction and the valence bands to split. This splitting leads to the formation of various types of excitons, including A-excitons and B-excitons [50]. These excitons arise from electronic transitions near the K and K' points in the Brillouin zone [51], with B-excitons having higher energy than A-excitons. The excitons can interact with phonons, transferring energy and momentum to them. In this thesis, we use this concept of excitons transferring energy to phonons and the temperature-dependent broadening of exciton linewidth [52] to investigate heat transport in TMDs.

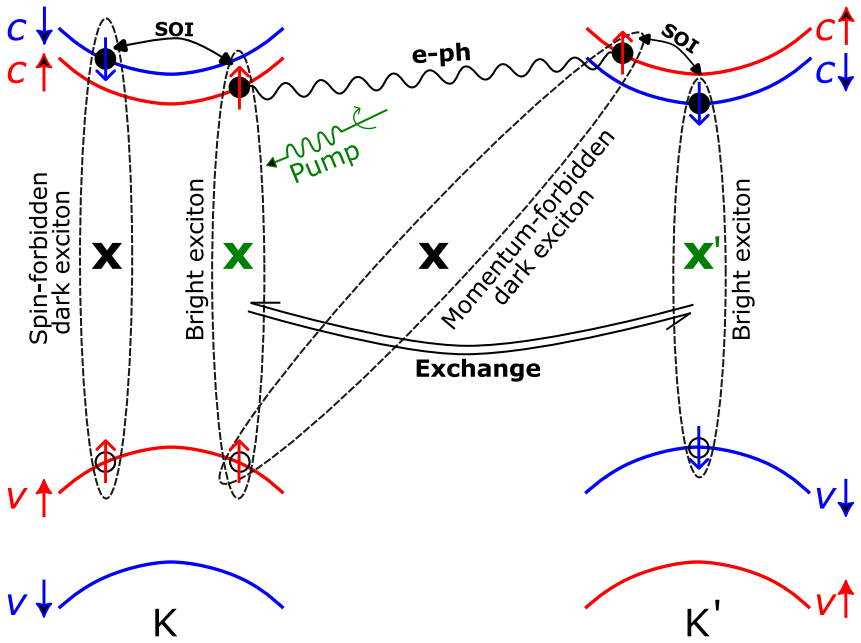


Figure 2.3: Bright and dark excitons. The intervalley bright exciton transition and bright-to-dark exciton transition processes in TMD systems. SOI: spin-orbit interaction. Adapted from Ref. [53].

Excitons in TMDs can be divided into two primary categories: bright excitons and dark excitons [54]. Bright excitons can recombine radiatively, resulting in the emission of photons. They typically manifest at the K and K' points in the Brillouin zone and play a direct role in light emission processes. Bright excitons hold significant importance for optoelectronic applications, such as light-emitting devices and photodetectors [55]. On the other hand, dark excitons cannot recombine radiatively due to either momentum or spin constraints (see Figure 2.3). These excitons may have their electron and hole components positioned at different points in the Brillouin zone or possess different spins. Despite not directly contributing to light emission, it has been shown that an increase in relative spectral positions between dark and bright excitonic states can decrease the overall photoluminescence efficiency of TMD materials [54].

2.1.4 Phonon band structure of TMDs

In metals, which have a high charge density, electrons significantly contribute to heat transport. This is governed by the Wiedemann-Franz law, which relates the thermal conductivity of a metal to its electrical conductivity. However, in non-metallic solids and semiconductors, where the charge density is lower, the primary carriers of heat are phonons [6]. Phonons are quanta of lattice vibrations and play a key role in determining a material's thermal transport properties.

The vibrational properties of TMDs are often compared to those of graphene, but they exhibit lower phonon frequencies due to the higher masses of atoms in TMDs. The phonon dispersion in bulk TMDs is characterized by a variety of vibrational modes. These include both in-plane and out-of-plane vibrations within each layer, as well as interlayer vibrations between different layers. The in-plane vibrations are typically higher in energy due to the stronger covalent bonding within the layers, while the interlayer vibrations are lower in energy due to the weaker van der Waals forces.

A monolayer TMD is essentially a single layer of the bulk crystal and thus lacks the interlayer vibrations present in the bulk material. This results in a simplified phonon dispersion with fewer vibrational modes. Each unit cell in a TMD monolayer consists of three atoms: one transition metal atom and two chalcogen atoms. This configuration results in a total of nine phonon branches in the phonon dispersion: three acoustic and six optical modes. Figure 2.4 shows the phonon dispersion of monolayer $MoSe_2$ as a typical example.

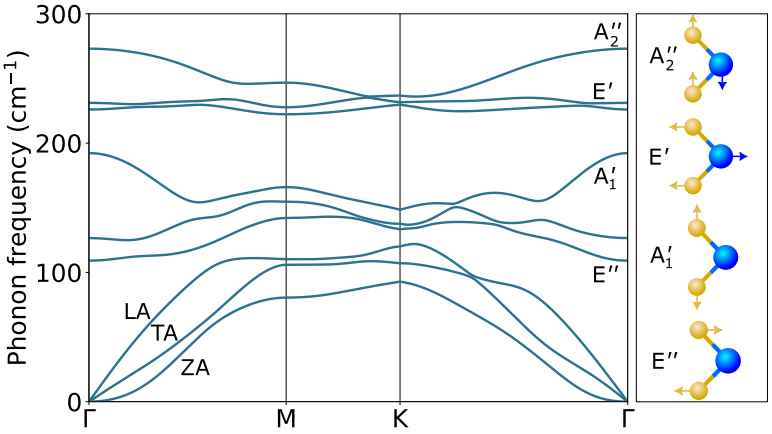


Figure 2.4: Phonon band structure. Phonon dispersion relation of monolayer $MoSe_2$ along with atomic vibrations representing the phonon modes.

At the Γ point in the Brillouin zone, the optical phonons of monolayer $MoSe_2$ are typically classified based on their symmetry and activity in Raman and infrared (IR) spectroscopies. Figure 2.4 (side panel) shows the atomic displacements associated with the optical phonons

at the Γ point. Of these, the E' mode is both Raman and infrared active due to its in-plane vibrational nature, while the A_1' mode is Raman active and represents out-of-plane vibrations. The A_2'' mode is infrared active, and the E'' mode, although Raman active, is typically suppressed in backscattering Raman experiments [56] due to polarization selection rules. Consequently, the primary Raman features observed in the Raman spectrum of monolayer $MoSe_2$ arise from the E' and A_1' modes. Understanding these phonon modes is not only essential for characterizing the vibrational properties but also for exploring the thermal transport behaviour.

2.2 Fourier description of heat transport

Heat transport phenomena are typically formulated at two levels of description: the microscopic level, which focuses on the evolution of the phonon distribution function, and the mesoscopic (or macroscopic) level, which considers the evolution of temperature and heat flux contributed by the full phonon population. At the mesoscopic (or macroscopic) level, Fourier's law is the simplest constitutive relation between the temperature and the heat flux. This law effectively describes the heat transport at the macroscale and serves as a benchmark model at the nanoscale.

Fourier's law of heat conduction states that the heat transfer rate is proportional to the temperature gradient. Similarly, Fick's law describes mass diffusion, where the flux is proportional to the concentration gradient. Both laws, developed in the 19th century, are foundational in describing transport phenomena and have played pivotal roles in understanding various physical phenomena and engineering applications related to heat and mass transfer.

The Fourier heat diffusion equation is expressed in terms of the heat flux ($\mathbf{q}$), thermal conductivity (κ), and temperature gradient (∇T) as follows [2]:

$$\mathbf{q} = -\kappa \nabla T \tag{2.1}$$

From the principle of energy conservation,

$$C_{\mathrm{v}} \frac{dT}{dt} = -\nabla \cdot \mathbf{q} + \sum_i S_i \tag{2.2}$$

where $\sum_i S_i$ represents internal sources of heat within the system and C_{v} is the volumetric heat capacity. Here, $\nabla \cdot \mathbf{q}$ denotes the divergence of the heat flux vector $\mathbf{q}$, representing the rate at which heat is spreading out from a point. From these equations above, one arrives at the spatiotemporal evolution of the temperature profile,

$$C_{\mathrm{v}}\frac{\partial T}{\partial t} = \nabla(\kappa\nabla T) + \sum_i S_i \tag{2.3}$$

In an isotropic medium and in the absence of external heat sources, this reduces to the following form:

$$\frac{\partial T}{\partial t} = D\left(\frac{\partial^2 T}{\partial x^2} + \frac{\partial^2 T}{\partial y^2} + \frac{\partial^2 T}{\partial z^2}\right) \tag{2.4}$$

where D is thermal diffusivity, defined as the ratio of thermal conductivity and volumetric heat capacity:

$$D = \frac{\kappa}{C_{\mathrm{v}}} \tag{2.5}$$

Material	***D*** **(cm^2/s)**	**Reference**
Aluminium	0.94	[57]
Copper	1.15	[57]
Gold	1.27	[58]
Silver	1.61	[57]
Silicon	0.88	[59]

Table 2.1: Thermal diffusivity values of some common solids.

The thermal diffusivity D is a key parameter in understanding the dynamics of heat transfer within a material. It quantifies how quickly heat diffuses through a material relative to its ability to store heat. The thermal diffusivity has been extensively measured across various materials, with typical values for common solids provided in Table 2.1. However, the exploration of thermal properties in novel two-dimensional materials, like TMDs, remains relatively less studied.

2.2.1 Solution to heat diffusion equation

By utilizing Equations 2.4 and 2.5, with a constant D for a one-dimensional problem, the heat equation can be expressed in the following form:

$$\frac{\partial T}{\partial t} = D\frac{\partial^2 T}{\partial x^2} \tag{2.6}$$

where T represents the temperature distribution at position x and time t. The fundamental solution to this equation $T(x,t)$, arises from an initial Dirac delta function $T(x,\,0) = \delta(x)$. This solution, given by [60]:

$$\Theta(x,t) = \frac{1}{\sqrt{(4\pi Dt)^n}} \exp\left(-\frac{|x|^2}{4Dt}\right) \tag{2.7}$$

represents an n-dimensional (here $n = 1$) normalized Gaussian function with a standard width $\sigma_{\mathrm{D}} = \sqrt{2Dt}$. In our context, we are interested in scenarios where the initial condition is a Gaussian profile $G_{\mathrm{a}}(x)$:

$$G_a(x) := T(x,0) = A^n \exp\left(-\frac{|x|^2}{2\sigma_0^2}\right) \tag{2.8}$$

A Gaussian profile often arises experimentally, such as from the spatial distribution of a laser beam focused onto a sample. Setting the boundary condition far away as $T(\pm\infty, t) = 0$ reflects the exponential decay of the Gaussian function, indicating that information from the initial perturbation propagates at the pace of the diffusion process. To determine the solution, we can convolve the fundamental solution $T(x,t)$ with the initial Gaussian profile $Ga(x)$:

$$T(x,t) = \frac{A^n}{\sqrt{1 + 2Dt/\sigma_0^2}^n} \exp\left(-\frac{|x|^2}{2(\sigma_0^2 + 2Dt)}\right) \tag{2.9}$$

This solution maintains a Gaussian profile, with both amplitude and width varying over time. The width broadens according to:

$$\sigma(t) = \sqrt{\sigma_0^2 + 2Dt} \tag{2.10}$$

This description accurately summarizes the problem and its solution, providing insight into the time-dependent behaviour of an initial Gaussian temperature profile under heat diffusion.

However, at the nanoscale, the diffusive description can become inadequate. For instance, when the mean free path (MFP) of the phonon modes becomes comparable to the length scales of the experiment, such as the width of the laser excitation or size of the system, non-Fourier behaviour emerges. There are several such evidences of non-Fourier type heat flow at the nanoscale [7]. To address these effects, phonon kinetic theory, specifically the Boltzmann Transport Equation (BTE) is used. The BTE is a general model that can explain both diffusive and non-diffusive transport phenomena and helps understand the microscopic processes that give rise to macroscopic heat transport observables.

2.3 Boltzmann Transport Equation

The BTE describes the distribution function $f_{\mathbf{k}}(\mathbf{r}, t)$, which quantifies the number of phonons near the position $\mathbf{r}$ at time t in the state (or mode) $\mathbf{k}$. Each state $\mathbf{k}$ is characterized

by the phonon wavevector $\mathbf{k}$ and frequency $\omega_{\mathbf{k}}$. When the system is in equilibrium, meaning that no external field or temperature gradient is imposed, the distribution of phonons follows the Bose-Einstein distribution [61], given by:

$$f_{\mathbf{k}}^{\mathrm{eq}} = \frac{1}{e^{\hbar\omega_{\mathbf{k}}/k_B T} - 1} \tag{2.11}$$

where $f_{\mathbf{k}}^{\mathrm{eq}}$ is the equilibrium distribution function for phonons, $\hbar$ is the reduced Planck's constant, $\omega_{\mathbf{k}}$ is the phonon frequency, k_{B} is the Boltzmann constant and T is the absolute temperature. When a phonon distribution is not in equilibrium, it undergoes changes through various processes, which can be described by the BTE. This equation was first introduced by Peierls in 1929 [62], who adapted the equations initially formulated for gases by Boltzmann in 1892 [63] to apply to solids.
Two primary mechanisms are involved in this evolution. The first is the drift of the distribution caused by the motion of phonons, which is represented by the drift operator in the BTE. The second mechanism involves the interactions of phonons with other phonons or particles, represented by the collision operator in the BTE. These two mechanisms collectively describe the evolution of the phonon distribution according to the BTE. This leads to the following BTE equation for phonons:

$$\frac{\partial f_{\mathbf{k}}}{\partial t} + \mathbf{v}_{\mathbf{k}} \cdot \nabla_{\mathbf{r}} f_{\mathbf{k}} = C(f_{\mathbf{k}}) \tag{2.12}$$

where the left-hand side of Equation 2.12 is called the drift operator, $\mathbf{v}_{\mathbf{k}}$ is the group velocity of phonons, given by $\mathbf{v}_{\mathbf{k}} = \nabla_{\mathbf{k}}\omega_{\mathbf{k}}$, and $C(f_{\mathbf{k}})$ is the collision term accounting for the scattering of phonons.

2.3.1 Relaxation Time Approximation

To make the BTE more treatable, it is necessary to introduce simplifying assumptions because of the intricate and nonlinear nature of the collision operator. The collision term in the BTE represents the rate of change of the distribution function due to phonon-phonon interactions and other scattering processes. In the Relaxation Time Approximation (RTA), the collision term is approximated by assuming phonons relax to their equilibrium distribution $f_{\mathbf{k}}^{\mathrm{eq}}$ over a characteristic relaxation time $\tau_{\mathbf{k}}$:

$$C(f_{\mathbf{k}}) = -\frac{f_{\mathbf{k}} - f_{\mathbf{k}}^{\mathrm{eq}}}{\tau_{\mathbf{k}}} \tag{2.13}$$

In the RTA, relaxation times are typically approximated by combining the momentum-destroying collisions (Umklapp) scattering time, scattering time due to lattice defects, and the momentum-conserving phonon-phonon (Normal) scattering time using Matthiessen's

rule. Despite its simplicity, RTA has limitations. It does not guarantee the conservation of energy in collisions, treating scattering events as Umklapp/resistive, leading to potential inaccuracies in certain scenarios [64, 65].

Nevertheless, the simplification of the collision operator $C(f_{\mathbf{k}})$ facilitates a straightforward interpretation of transport phenomena. For instance, within the framework of the RTA, it allows us to define the concept of the phonon MFP $\Lambda_{\mathbf{k}} = v_{\mathbf{k}}\tau_{\mathbf{k}}$. The MFP represents the average distance an excited non-equilibrium phonon travels before colliding. It is also possible to obtain the microscopic expression for thermal conductivity for isotropic media within the RTA. Using the RTA form of the collision operator, the BTE simplifies to:

$$\frac{\partial f_{\mathbf{k}}}{\partial t} + \mathbf{v}_{\mathbf{k}} \cdot \nabla_{\mathbf{r}} f_{\mathbf{k}} = -\frac{f_{\mathbf{k}} - f_{\mathbf{k}}^{\mathrm{eq}}}{\tau_k} \tag{2.14}$$

Assuming a stationary temperature gradient along the x-direction (distribution function will only change in x-direction), and for systems not far from equilibrium, meaning $\frac{\partial f_{\mathbf{k}}}{\partial x} \approx \frac{\partial f_{\mathbf{k}}^{\mathrm{eq}}}{\partial x}$, $f_{\mathbf{k}}$ simplifies to:

$$f_{\mathbf{k}} \approx f_{\mathbf{k}}^{\mathrm{eq}} - \tau_{\mathbf{k}} v_x \frac{\partial f_{\mathbf{k}}^{\mathrm{eq}}}{\partial T} \frac{dT}{dx} \tag{2.15}$$

and the thermal conductivity κ is obtained by applying the definition of the heat flux $\mathbf{q}$, which in terms of phonons reads: $\mathbf{q} \equiv \sum_{\mathbf{k}} \hbar\omega_{\mathbf{k}} \mathbf{v}_{\mathbf{k}} f_{\mathbf{k}}$. For an isotropic material, the thermal conductivity is then given by:

$$\kappa = \frac{1}{n} \sum_{\mathbf{k}} C_{\mathbf{k}} \mathbf{v}_{\mathbf{k}}^2 \tau_{\mathbf{k}} \tag{2.16}$$

where the specific heat of mode $\mathbf{k}$ is given by: $C_{\mathbf{k}} = \hbar\omega_{\mathbf{k}} \frac{\partial f_{\mathbf{k}}^{\mathrm{eq}}}{\partial T}$ and n is the dimensionality of the material (for example, $n = 3$ for silicon, germanium or diamond, and $n = 2$ for graphene). This linearization method simplifies the BTE and provides an initial approximation to calculate the thermal conductivity. The phonon relaxation time $\tau_{\mathbf{k}}$, or phonon lifetime, is a critical parameter in determining thermal conductivity. It characterizes the average time between phonon-scattering events, which can be affected by various scattering mechanisms such as phonon-phonon interactions, boundary scattering, isotope scattering, and impurity scattering.

In summary, the BTE provides a comprehensive framework for understanding phonon transport and calculating important thermal properties such as phonon MFP and thermal conductivity. The RTA simplifies the analysis, allowing us to relate microscopic phonon properties to macroscopic thermal behaviour. Thus, while the relaxation time approximation provides a simplified framework for understanding phonon transport, its limitations necessitate more accurate approaches, such as exact solutions of the BTE [66] or a hydro-

dynamic treatment [67] (as discussed in Section 2.5), especially at low temperatures, and for semiconductors and low-dimensional materials.

2.4 Phonon scattering mechanisms

Phonons populating a mode $\mathbf{k}$ have a defined energy $\hbar\omega_{\mathbf{k}}$ and a defined crystal momentum $\hbar\mathbf{k}$. All phonon collisions conserve energy. Therefore, for a three-phonon process involving modes $\mathbf{k}_1$ and $\mathbf{k}_2$ resulting in mode $\mathbf{k}_3$, the energy conservation condition is:

$$\omega_{\mathbf{k}_1} + \omega_{\mathbf{k}_2} = \omega_{\mathbf{k}_3} \tag{2.17}$$

Similarly, for a three-phonon process involving mode $\mathbf{k}_1$ resulting in modes $\mathbf{k}_2$ and $\mathbf{k}_3$, the energy conservation condition is:

$$\omega_{\mathbf{k}_1} = \omega_{\mathbf{k}_2} + \omega_{\mathbf{k}_3} \tag{2.18}$$

The collision operator in the BTE accounts for phonon scattering mechanisms, which can be broadly categorized into two types: Normal (N) processes and Umklapp (U) processes.

In Normal processes, the total crystal momentum of the phonons is conserved. During these collisions, the phonon wavevectors remain within the first Brillouin zone, and the overall momentum balance is maintained. Mathematically, this can be expressed as:

$$\mathbf{k}_1 + \mathbf{k}_2 = \mathbf{k}_3 \tag{2.19}$$

Normal scattering generally results in less resistance to heat flow compared to Umklapp processes. At room temperature, Normal scattering tends to be weaker compared to Umklapp scattering in most materials [6], contributing to the significant damping effect on heat flow in solids.

Umklapp processes do not conserve the total crystal momentum of phonon particles. These scatterings alter the direction of phonon propagation, typically leading to direct thermal resistance and significantly affecting thermal conductivity. The key feature of Umklapp processes is the transfer of momentum to the crystal lattice, resulting in a net phonon momentum loss and thus the impeding heat flow. These processes can be represented mathematically as:

$$\mathbf{k}_1 + \mathbf{k}_2 = \mathbf{k}_3 + \mathbf{G} \tag{2.20}$$

where $\mathbf{G}$ is a reciprocal lattice vector, indicating that the resulting phonon wavevector is outside the first Brillouin zone and is effectively folded back into it. At room temperature,

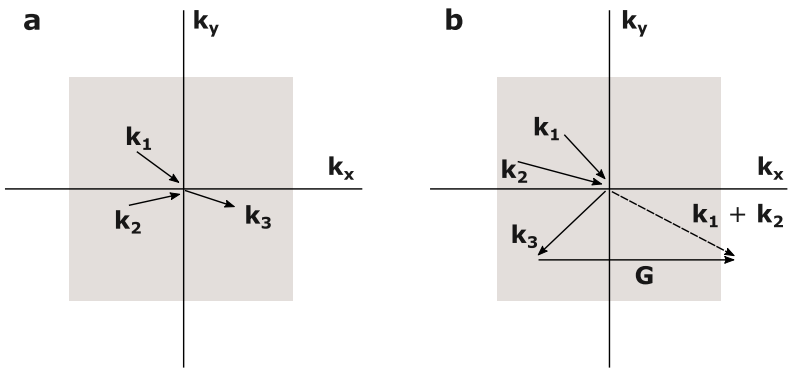


Figure 2.5: Three phonon scattering processes. (a) Normal and **(b)** Umklapp (resistive) scattering mechanisms are illustrated in a two-dimensional square lattice. The square represents the first Brillouin zone.

Umklapp processes generally dominate and contribute significantly to the damping of heat flow in solids [6]. These two scattering processes are schematically depicted in Figure 2.5 and they give rise to diffusive and non-diffusive transport phenomena.

2.5 Thermal transport beyond Fourier

Thermal transport behaviours beyond the Fourier description in a material are observed under both collective and nanoscale conditions. The collective conditions are when the momentum-conserving collisions dominate over the momentum-destroying collisions and are typically defined as the Ziman regime. In this regime, under a small thermal gradient, the phonon distribution displaces slightly, with a mode-independent drift velocity. This means that the phonons gain excess momentum from the temperature gradient. This excess momentum is differently affected by Normal and Umklapp scatterings [68].
When Umklapp scatterings dominate, a diffusive transport regime emerges, where the heat flux follows Fourier's law of heat conduction (see Figure 2.6a). Umklapp scattering destroys the excess momentum, causing phonons to relax back to local equilibrium. Conversely, a non-diffusive type of heat transport emerges when Normal collisions dominate. The excess momentum is exchanged among phonons through Normal scatterings, leading all phonon modes to exhibit the same drift velocity and approach a displaced distribution (collective behaviour). This behaviour is analogous to fluid dynamics, where all collisions are Normal (as in momentum-conserving), and is traditionally associated with hydrodynamic heat conduction [68] (see Figure 2.6b).
To quantify the thermal transport properties in such cases, one model that extends beyond the RTA is the Callaway model [69]. In this model, Normal collisions relax the distribution back to the displaced one, while resistive collisions relax the distribution back to equilibrium. These two effects happen independently and simultaneously according to

the Callaway model. This model has proven useful for predicting bulk thermal conductivity in materials where pure RTA fails, such as at low temperatures [70]. The Callaway model explains why the conductivity of silicon [71] is slightly larger than what RTA predicts. Yet, it has been shown inadequate to predict the thermal conductivity of some 2D materials like boron antimonide and boron arsenide [72].

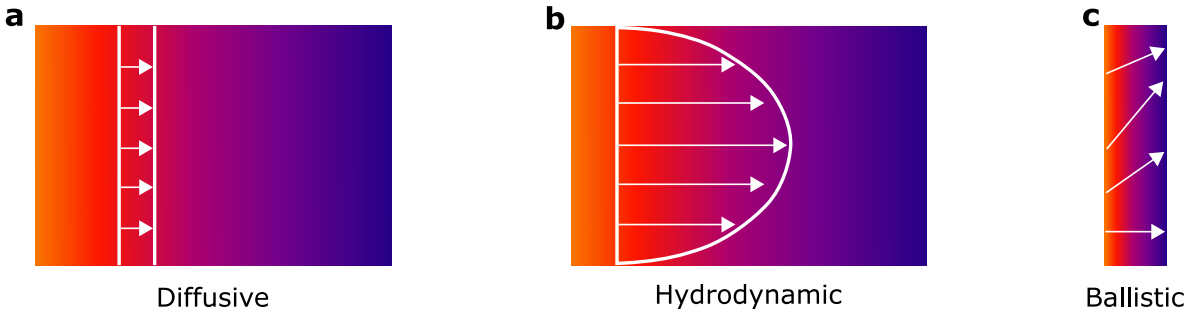


Figure 2.6: Heat flux profiles. Schematic of phonon heat flux profile: **(a)** diffusive, **(b)** hydrodynamic and **(c)** ballistic. Adapted from Ref. [68].

Under nanoscale conditions, where the MFP Λ of phonons becomes comparable to the system size, two primary phenomena emerge: the ballistic (see Figure 2.6c) and the hydrodynamic (nanoscale) regimes. In 3D bonded materials like silicon (bulk), phonons with MFPs longer than 1 micron contribute to half of the thermal conductivity [73]. Whereas in 2D bonded materials, for example, in monolayer (bilayer) of $MoSe_2$, more than 30% (20%) of the thermal conductivity is governed by modes with $\Lambda > 1$ μm [74].
In the ballistic case, internal phonon scattering is absent, and phonons interact with the boundaries or impurities present in the material, undergoing either diffuse or specular scattering. Boundaries limit the mean free path, and therefore thermal conductivity becomes smaller, as observed in silicon [75], for example. On the other hand, the hydrodynamic regime in nanoscale conditions can emerge if there is a slow relaxation of the heat flux. In this case, it is not necessary to have a dominant normal scattering event compared to Umklapp scattering as in the Ziman regime.
The emergence of hydrodynamic behaviour in the Ziman regime ($N \gg U$) is well-established and not under debate. However, at the nanoscale regime, the correct interpretation—ballistic or hydrodynamic—remains a topic of active discussion [9, 76–79].

2.5.1 Ballistic phonon transport

The transition from diffusive to ballistic regimes can be captured by incorporating the phonon MFP into the heat transport equations. When the system size L is much smaller than the phonon MFP Λ ($L \ll \Lambda$), ballistic transport dominates. Conversely, when $L \gg \Lambda$, the transport becomes diffusive. However, when the system size L is comparable to the

MFP ($L \sim \Lambda$), the phonon transport enters the quasi-ballistic regime. In this regime, for phonons with $\Lambda > L$, their effective MFP is limited by L, leading to quasi-ballistic heat transport.

In an isotropic solid, as shown in the previous section, the thermal conductivity κ is given by

$$\kappa = \frac{1}{n} \sum_{\mathbf{k}} C_{\mathbf{k}} \mathbf{v}_{\mathbf{k}} \Lambda_{\mathbf{k}} \tag{2.21}$$

In conditions where the phonon MFP is comparable to L, the system enters the Casimir limit. In this case, the effective MFP is limited by the system size. Assuming a constant phonon group velocity v, the thermal conductivity becomes proportional to both the system size and the specific heat, as described by Casimir [80]. In thin films and nanowires, when the MFP is limited by the system size, significant size effects on thermal conductivity are observed [75, 81, 82]. Ballistic heat transport was observed in silicon membranes at room temperature using the transient thermal grating method [83], while more recently, quasi-ballistic heat transport has been reported in MoS_2 using time-domain thermoreflectance technique [84]. It is also important to note that such size effects can also occur when the size of the heat source is comparable with phonon MFP [85–87].

2.5.2 Phonon hydrodynamics in Ziman regime

The approximations in the RTA model do not fully capture the complexity of phonon interactions, as they consider each phonon mode to evolve independently. This is an inadequate approximation because the collision operator in the BTE is not diagonal [88] and cannot be represented merely in terms of a relaxation time for each mode. This simplification neglects the specific transitions between phonon modes that induce correlations and collective phenomena. While this assumption of independent evolution can predict heat transport properties in bulk materials reasonably well, it fails in other cases, particularly at low temperatures and at the nanoscale [70, 72].

In this context, one can go beyond the RTA model to describe the phonon hydrodynamic phenomena. The hydrodynamic model can capture the collective effects in the presence of small thermal gradients, thereby explaining a variety of phenomena primarily related to the dependency of thermal conductivity on temperature or size. The seminal work by R. A. Guyer and J. A. Krumhansl [89] significantly advanced this understanding by developing a new approach which contributed to extracting physical insights from the BTE for phonons using fundamental conservation laws (see Section 2.4). Their approach separates the collision operator into two components:

$$C(f_{\mathbf{k}}) = N(f_{\mathbf{k}}) + R(f_{\mathbf{k}}) \tag{2.22}$$

where $N(f_{\mathbf{k}})$ represents the Normal processes that conserve momentum, and $R(f_{\mathbf{k}})$ represents the resistive processes that do not. They considered situations where the Normal collisions dominate over resistive collisions ($N(f_{\mathbf{k}}) \gg R(f_{\mathbf{k}})$) and group velocity $\mathbf{v}_{\mathbf{k}} = v$ is constant. The solution is based on developing the BTE for isotropic materials in terms of the eigenvectors of the symmetrized N-operator. This operator must conserve both energy and crystal momentum, resulting in four independent distribution functions with a null eigenvector: the zeroth-order element, $|0\rangle$, which is related to the deviation of energy from the equilibrium energy, and three first-order elements, $|1, i\rangle$, which are related to the crystal momentum of the system in the three spatial directions, $i = x, y, z$ [89].

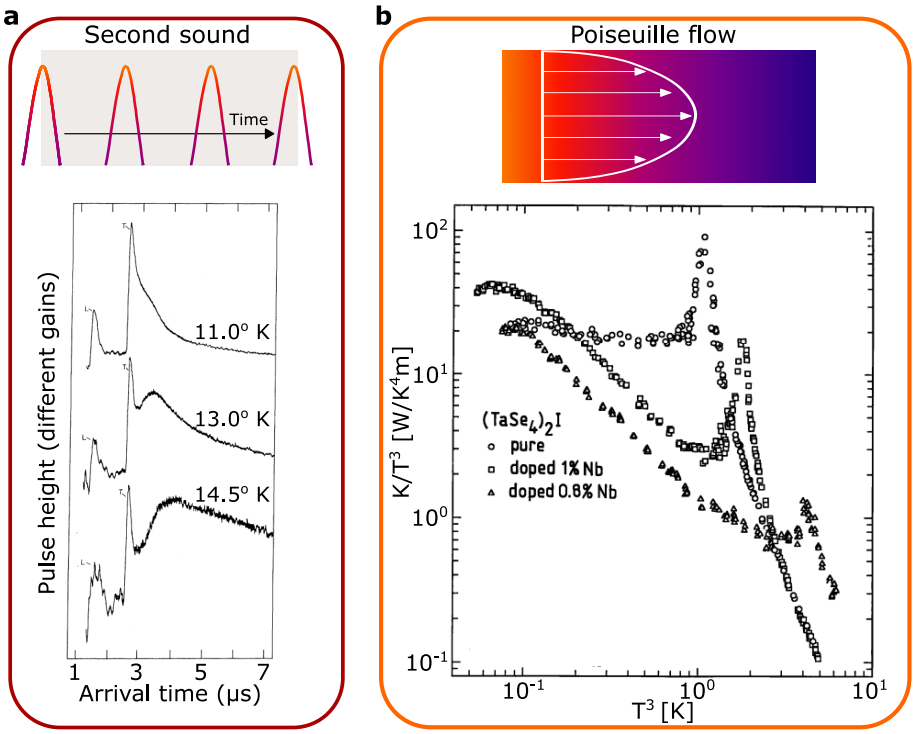


Figure 2.7: Second sound and phonon Poiseuille flow. (a) Schematic illustration (top) of second sound propagation, where a heat pulse travels through a material with minimal damping (Adapted from Ref. [68]). Experimental results (bottom) showing the observation of second sound in heat pulse measurements in sodium fluoride (Reprinted with permission from Ref. [90]). **(b)** Schematic illustration (top) of phonon Poiseuille flow (Adapted from Ref. [68]). Plot of κ/T^3 *vs.* temperature (bottom) in single crystals, showing a thermal conductivity dependence exceeding T^3 (Reprinted with permission from Ref. [91]).

In the diffusive limit ($N \to 0$), the phonon modes relax independently toward equilibrium through different scattering rates, as assumed in the RTA. In the collective situation ($N \gg R$), numerous Normal collisions occur between each resistive collision, redistributing the lost crystal momentum. Consequently, the distribution relaxes collectively and is characterized by a single collective relaxation time τ_c for the momentum of all the phonon modes. The thermal properties in the Ziman regime are usually calculated by solving

BTE with the full collision operator [92–95].

There have been several experimental observations that confirm the occurrence of hydrodynamic phonon transport where Normal collisions dominate (see Figures 2.7, 2.8). This includes the wave-like propagation of heat, known as second sound (see Figure 2.7a), which has been observed in materials such as helium [96], bismuth [97], sodium fluoride [98], strontium titanate [99], and graphite [93].

Hydrodynamic transport can also lead to phonon Poiseuille flow (see Figure 2.7b) similar to that of viscous fluids under the pressure gradient in a pipe. This transport mechanism leads to a distinctive dependence of the thermal conductivity on temperature, notably exceeding T^3. This phenomenon has been experimentally observed in quasi-one-dimensional single crystals [91], strontium titanate [100], black phosphorous [101], and graphite [102].

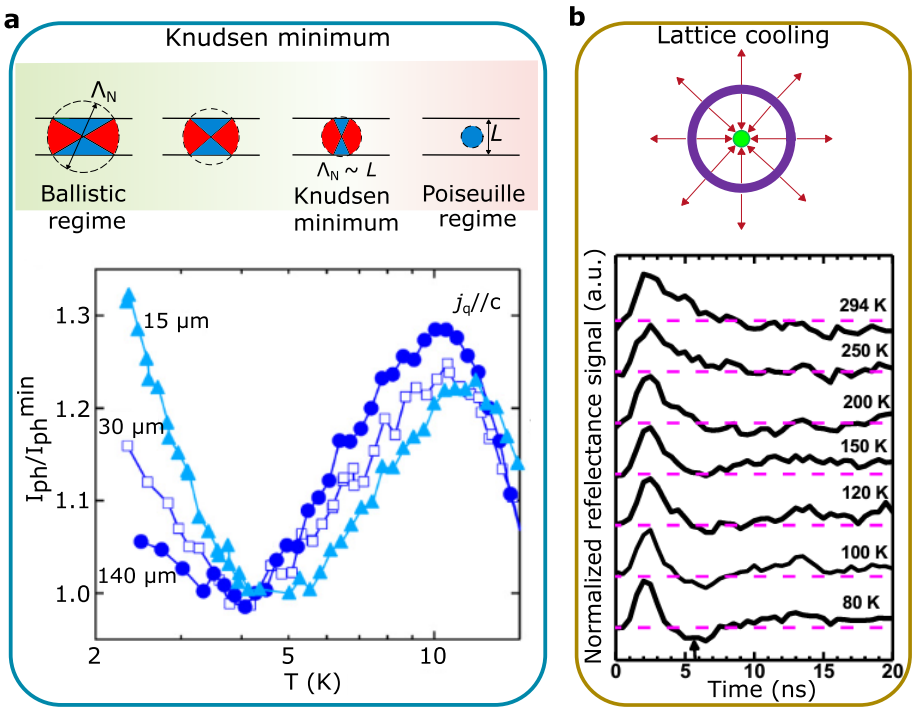


Figure 2.8: Knudsen minimum and lattice cooling. (a) Schematic (top) showing the Knudsen minimum. The diffuse boundary scattering rate is effectively increased by Normal scattering when the MFP of Normal scattering Λ_N, represented by the dashed circle, is comparable with the sample size L, producing a local minimum in the effective phonon MFP. The thickness dependence (bottom) of the Knudsen minimum in black phosphorus is expressed via the temperature variation of the effective phonon MFP along the c-axis, normalized by its value at the Knudsen minimum. As thickness increases, the minimum shifts to lower temperatures (Reprinted/Adapted from Ref. [101]). **(b)** Schematic (top) of the ring-shaped pump and probe at the center on the sample surface. Arrows indicate heat-propagating directions. Normalized reflectance dynamics (bottom) in graphite at different temperatures, showing the appearance of negative amplitude (Reprinted with permission from Ref. [103]).

Another observation is the Knudsen minimum (see Figure 2.8a), which describes how

the increased scattering of phonons at the boundaries of a material when the MFP of Normal scattering is smaller than the sample dimension, results in a local minimum in the effective phonon MFP. This phenomenon is visualized by a local minimum in the thermal conductivity *vs.* temperature plot, as predicted in graphite [95] and as observed in black phosphorous [101].

Recently, hydrodynamic lattice cooling (see Figure 2.8b), manifested by a sign change in the reflection dynamics, was also observed using pump-probe thermal reflection measurements in graphite [103]. Using a ring-shaped pump beam, they observed that the heat pulse initially propagates inward and then outward, causing a negative temperature rise at the center. This phenomenon was attributed to hydrodynamic thermal fluctuations. Importantly, all these observations of hydrodynamic heat flow are predominantly seen at low temperatures.

Theoretical predictions have indicated the presence of phonon hydrodynamic behaviour in 2D materials like graphene and TMDs [104, 105]. Although there are several experimental evidences of hydrodynamic heat transport well above cryogenic temperatures (up to 200 K [106]) for graphitic materials, there are no observations of phonon hydrodynamic transport in TMDs at any temperature yet.

2.5.3 Phonon hydrodynamics in nanoscale

As discussed, the framework developed by Guyer and Krumhansl considered a dominance of Normal phonon collisions, particularly in the low-temperature limit where such collisions prevail. However, early theoretical works by Hardy and colleagues [107] proposed that hydrodynamic behaviour is not necessarily restricted to situations where Normal collisions dominate. They identified the slow relaxation of heat flux relative to experimental timescales as pivotal for the emergence of wave-like (hydrodynamic) heat propagation. This is manifested by "drifting" (where $N \gg R$) and "driftless" (not associated with the displaced distribution or a drift velocity) second sound [107]. Recent theoretical advancements [67, 108] have generalized this hydrodynamic framework, extending its applicability to a broader range of materials and temperatures.

One such significant advancement was made by Lluc Sendra and colleagues [67], who proposed a generalization of the hydrodynamic equations by solving the BTE. This approach established a specific connection between the microscopic theory (BTE) and the mesoscopic constitutive relation between the heat flux and the temperature. They derived the following expression for the heat flux:

$$\tau \frac{\partial \mathbf{q}}{\partial t} + \mathbf{q} + \kappa \nabla T = \ell^2 \left(\nabla^2 \mathbf{q} + \alpha \nabla (\nabla \cdot \mathbf{q}) \right) \tag{2.23}$$

where ℓ is the non-local length, and α is a coefficient related to the hydrodynamic effects (see Ref. [67] for detailed derivation). This equation is quite similar to the hydrodynamic equation derived by Guyer and Krumhansl in the Ziman limit [89]. Equation 2.23 introduces a non-local term (proportional to ℓ^2) and a memory term (proportional to τ) into Fourier's law. By assuming a simplified collision operator (RTA approximation), they were also able to obtain the expression for thermal conductivity as:

$$\kappa = \frac{1}{3}\sum_{\mathbf{k}} C_{\mathbf{k}} \mathbf{v}_{\mathbf{k}}^2 \tau_{\mathbf{k}} \tag{2.24}$$

This expression recovers the thermal conductivity within the RTA framework (see Equation 2.16). Microscopically, the non-local length is interpreted as the weighted average of the phonon MFPs and is expressed as:

$$\ell^2 = \frac{1}{5}\frac{\left\langle \frac{v_{\mathbf{k}}^3 \tau_{\mathbf{k}}^2}{v_{\mathrm{p},\mathbf{k}}} \right\rangle}{\left\langle \frac{v_{\mathbf{k}}}{v_{\mathrm{p},\mathbf{k}}} \right\rangle} \tag{2.25}$$

where v_{p} is the phonon phase velocity defined as $v_{\mathrm{p}} = \frac{\omega_{\mathbf{k}}}{|\mathbf{k}|}$. The non-local length is an intrinsic material property, meaning it does not depend on the size or shape of the heating source but is instead determined by the material's inherent characteristics. The heat flux relaxation time from this framework is given by:

$$\tau = \frac{\langle v_{\mathbf{k}}^2 \tau_{\mathbf{k}}^2 \rangle}{\langle v_{\mathbf{k}}^2 \tau_{\mathbf{k}} \rangle} \tag{2.26}$$

At the mesoscopic level of description, both ℓ and τ are intrinsic properties that determine the length and time scales where thermal perturbations remain correlated. This modern formulation provides a comprehensive framework for understanding and predicting the heat transport behaviours at the nanoscale. Several studies have demonstrated its effectiveness across a range of temperatures and materials. For instance, it has been applied to silicon [77, 78, 109–112], bismuth telluride [113], indium gallium arsenide [114], and germanium [115].

3

Fabrication of suspended TMDs

"Success is the sum of small efforts, repeated day in and day out." - Robert Collier

In this chapter, we detail the general fabrication process and the characterization of suspended transition metal dichalcogenides flakes, down to the monolayer limit. We use this fabrication process throughout this thesis to investigate heat transport. Typically, we fabricate our suspended samples by mechanical exfoliation from bulk crystal, followed by a transfer onto a substrate with a 15 μm diameter hole using a home-built dry transfer stage, as described in detail in this chapter. We will also show thorough characterization measurements to analyze the properties of such samples. This chapter serves as a foundational guide for the fabrication and characterization methods of samples used in subsequent heat transport studies in this thesis.

This chapter is based on the following publication:

S. Varghese*, D. Saleta Reig*, J. D. Mehew, A. Block, A. El Sachat, E. Chávez-Ángel, M. Sledzinska, B. Ballesteros, C. M. Sotomayor Torres, and K. J. Tielrooij, Fabrication and characterization of large-area suspended $MoSe_2$ crystals down to the monolayer, Journal of Physics: Materials, 4, 046001 (2021) [116].

*Equal contributions

3.1 Introduction

Suspended flakes of layered materials are essential for accurately studying their intrinsic properties without unwanted effects from their environment. Interactions such as Coulomb scattering [117], dielectric effects [118], phonon scattering [119], and near-field energy transfer [120] can significantly alter the electrical, optical, thermal, and mechanical properties of flakes supported on substrates [121–123]. To mitigate these environmental effects and probe the material's intrinsic characteristics, it is crucial to use freely suspended crystals, such as those placed over holes or trenches. Ideally, the suspended flakes should be monocrystalline, residue-free, strain-free, relatively easy to fabricate, and durable.
In this chapter, we describe an easy and cost-effective technique to fabricate such suspended TMD samples using the polydimethylsiloxane (PDMS)-assisted dry transfer [124] method, onto a substrate with a 15 μm diameter hole, with a full transmission window. This fabrication method is applied to prepare all the TMD samples studied in this thesis. We demonstrate the ability to fabricate these material systems with flakes down to the monolayer. We then outline the characterization techniques used to analyze these samples. While these characterization methods are applied to all TMDs studied in this thesis, we specifically focus on suspended $MoSe_2$ flakes as a representative example to provide detailed insights and demonstrate the effectiveness of our approach.

3.2 Fabrication of samples

3.2.1 Preparation of PDMS and exfoliation

We use the exfoliation and dry transfer methodology detailed in Ref. [125] for fabricating the suspended flakes studied in this thesis. To prepare the PDMS stamp, we mix the silicone elastomer base (SYLGARD 184) and silicone elastomer curing agent in a ratio of 1 part curing agent to 10 parts elastomer base by weight. After thorough stirring, we place the mixture in a vacuum desiccator to eliminate air bubbles until it becomes transparent. Subsequently, we pour the mixture into a Petri dish to form a uniform, bubble-free PDMS layer about 1 mm in thickness, ensuring an even surface. We allow the PDMS to dry in ambient conditions for approximately 48 hours, before sealing the Petri dish to prevent dust accumulation and to maintain adhesive properties. Finally, we cut the PDMS into necessary sizes when needed, choosing sections from the central region of the Petri dish where the PDMS is flat.
During exfoliation, we enclose a flat TMD material piece between two strips of Scotch tape. Through repetitive contact at close proximity, we thin and spread the crystals over an area

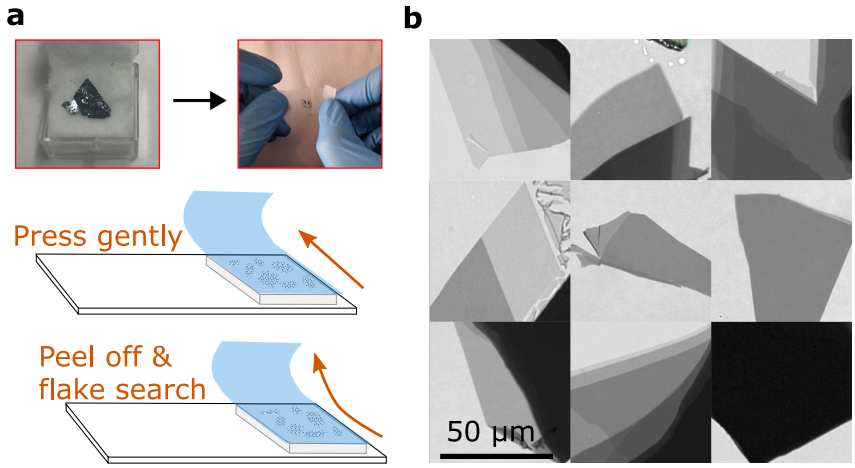


Figure 3.1: TMD exfoliation. (**a**) Pictures showing the bulk TMD crystal and flake exfoliation (top panels), along with the schematics illustrating the exfoliation of TMD onto PDMS (grey part) on a glass slide. (**b**) Optical microscope images of exfoliated flakes of different thicknesses ($MoSe_2$) on PDMS.

of around $1 \times 2\,\mathrm{cm}^2$. These strips act as the parent tapes. Exfoliation tapes are derived by peeling off thin crystals using fresh Scotch tape. Subsequently, we immediately bring the exfoliation tape into contact with a PDMS bed positioned along the edge of a pristine glass slide. Gentle rubbing with a cotton swab ensures proper adhesion between the crystals and PDMS, which typically yields larger flakes. We employ a swift peeling technique for the exfoliation tapes to enhance the yield and size of thin flakes (see Figure 3.1a). Using an optical microscope, we check for wrinkle-free, large (> 15 µm), and uniformly thick flakes with well-defined edges, indicative of superior quality and single-crystalline nature, under both transmission (see Figure 3.1b) and reflection configurations.

3.2.2 Deterministic dry transfer

Drawing inspiration from the design in Ref. [124], we employ a home-built dry transfer stage setup (see Figure 3.2) for the deterministic, precise transfer of TMD flakes to the substrates. All the suspended TMD samples used in this thesis are fabricated using this custom-built transfer stage. The following are the most significant enhancements that we have implemented compared to the system described in Ref. [124]. First of all, we equip the stage with motorized zoom and focus capabilities. Secondly, we integrate a vacuum chuck with temperature control, enabling smooth mounting and dismounting of substrates and samples. Thirdly, we equip the transfer stage with six degrees of freedom to align the flake with regard to the target substrate (x, y, z, rotation θ, pitch δ, and roll ϕ), as depicted in Figure 3.2. The tilt degrees of freedom enable fine control of the flake-substrate contact angle and flake release direction, crucial when fabricating suspended flakes. Furthermore,

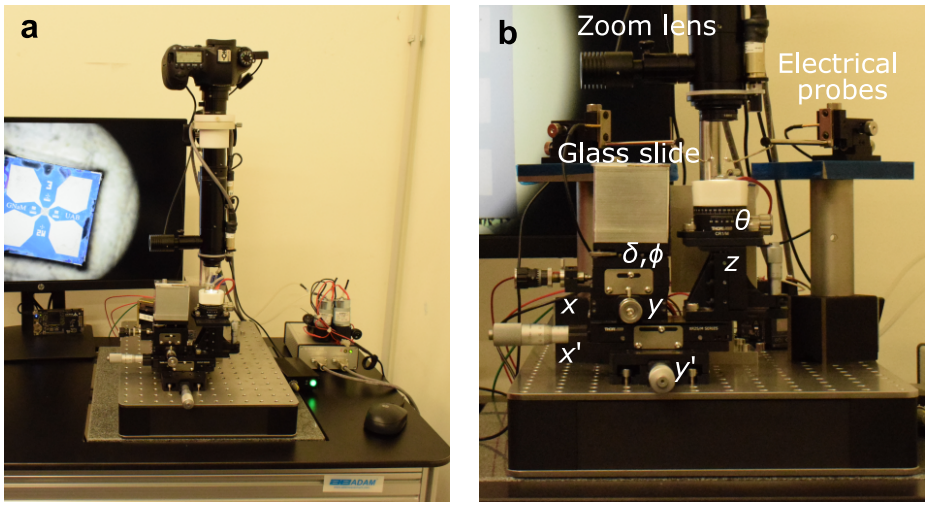


Figure 3.2: Dry transfer stage setup. (**a, b**) Pictures of the home-built transfer stage setup and its (a) zoom-in view. The components used to build the setup and other details are listed at the end of this chapter, see Table 3.1.

we utilize the x' and y' stages at the bottom of the system to enable sample examination without losing alignment between the flake and substrate. The details of the components used to build the transfer stage setup are provided in Table 3.1.

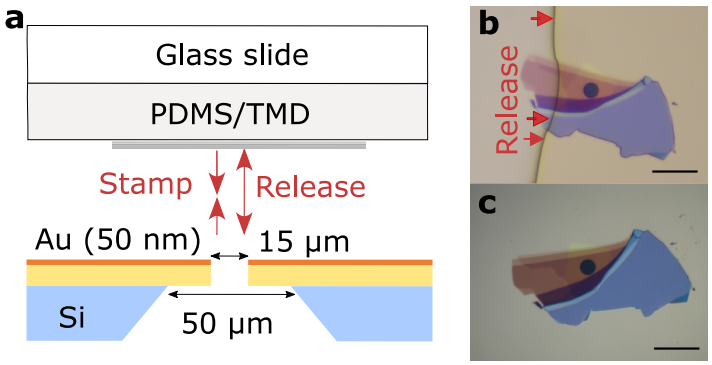


Figure 3.3: Dry transfer of the exfoliated flakes. (**a**) Schematics of the flake transfer to Norcada substrate. (**b**) Optical image taken at the time of transferring, (**c**) resulting suspended sample (5 layer $MoSe_2$). Scale bar: 50 μm.

For the samples used throughout this thesis, we typically use commercial Si_3N_4 membranes as substrates. These substrates have a single hole of 15 μm in diameter (NTPR005D-C15, Norcada) in the center. We gold-coat the substrates before the flake transfer (Ti/Au: 5/50 nm) to take advantage of the strong adhesion between gold and chalcogen atoms [126], significantly enhancing the transfer yield. For the transfer of a TMD flake onto a gold-coated perforated substrate, we employ the z-stage to advance the substrate towards the viscoelastic PDMS stamp, which holds the targeted flake. This general method for fabricating TMD samples is illustrated schematically in Figure 3.3a. To determine the

contact and release directions, we adjust the δ and ϕ stages prior to the stamping. We note that the best transfer yield is obtained when releasing the flake onto the substrate beginning from its sharper (thinner) edge and progressing towards thicker regions, as depicted in Figure 3.3.

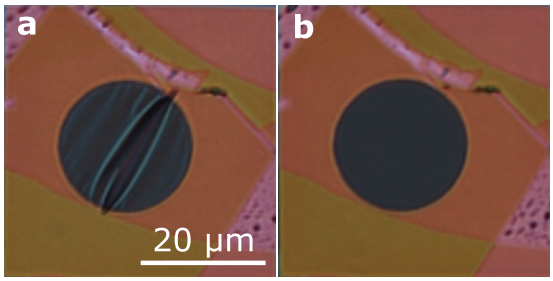


Figure 3.4: Flake ironing. (**a**) Wrinkled suspended region after dry transfer of an exemplary $MoSe_2$ sample that is flattened by (**b**) annealing on a hotplate at 150 °C for 30 minutes.

During the fabrication of suspended TMD flakes, sometimes we observe wrinkle formation in the suspended region. This is typically caused by substantial straining of TMD material during the dry transfer process (see Figure 3.4a). We solve this problem by subjecting the sample to a 30-minute heat treatment at 150 °C on a hot plate.

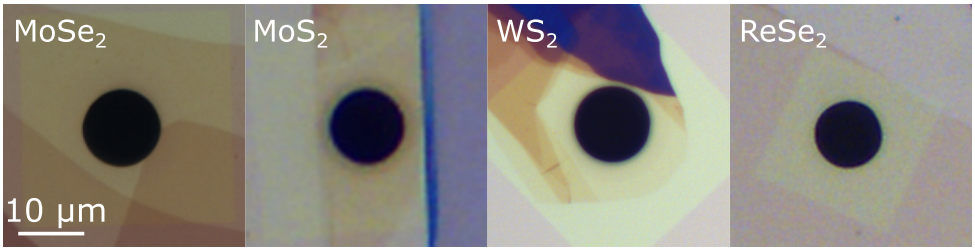


Figure 3.5: Dry transferred monolayer flakes. Optical microscope images of suspended monolayer TMDs. The scale bar is valid for all four images.

The application of controlled heat proves instrumental in eliminating wrinkles and restoring the desired flatness (see Figure 3.4b) to the suspended region, enabling the fabrication of large-area flakes across different TMDs (for monolayers, see Figure 3.5) and thicknesses (see Figure 5.1, Figure 7.3, and Figure 6.1c).

3.3 Characterization of the samples

In this section, we describe the typical characterization of suspended samples, including the determination of thickness, analysis of surface roughness, assessment of crystallinity, and relative strain evaluation. We typically perform these measurements on most of the TMD samples studied throughout this thesis, with a particular emphasis on thickness determination and Raman spectroscopy, which are conducted for almost all samples.

Although the specific measurements detailed here are for suspended $MoSe_2$ samples, the methodologies are applied across most of the suspended samples investigated in this thesis.

3.3.1 Thickness determination

To quantify the thickness of suspended samples, we employ optical contrast [127], photoluminescence (PL), atomic force microscopy (AFM), and Raman spectroscopy techniques.

Optical contrast and photoluminescense

We usually combine optical contrast and PL measurements to determine the thickness of very thin TMD flakes ($1-5$ layers). Optical contrast is a straightforward approach for identifying the thickness of exfoliated flakes. Using ImageJ software [128], we split the transmission optical microscopy images of the flakes on PDMS into RGB color channels. We find that the green channel (see Figure 3.6a) offers the best signal-to-noise ratio and good contrast for thin flakes, making it ideal for plotting intensity profiles across regions of interest (from PDMS to the flake). This enables quantifying the intensity drops with respect to the substrate based on the flake's thickness. Finally, we normalize the intensity profiles to the average intensity of the transparent substrate for comparison with the flake of known thickness (see Figure 3.6b[†]).

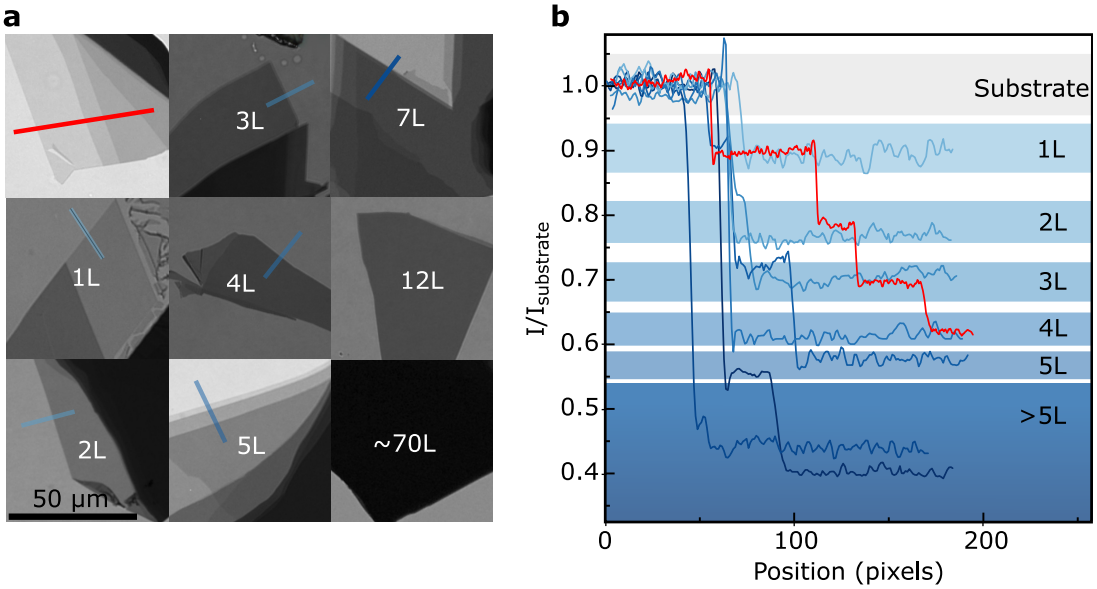


Figure 3.6: Optical contrast analysis of exfoliated flakes. (**a**) Green channel transmission images of $MoSe_2$ flakes on PDMS, prior to the dry transfer. Calibration sample: top left image in (a). (**b**) Normalized (to the substrate intensity) intensity profiles of the solid lines in panel (a).

[†]Most of the experimental figures in this thesis are plotted according to the color codes suggested in Ref. [129].

To confirm the thickness of the thinnest flakes, we perform PL measurements on the suspended region of the flake. For this, we excite the flake with 532 nm continuous wave (CW) light and record the emission intensity with a nitrogen-cooled Charge Coupled Device detector (see Figure 3.7). The emission peak for 1L (2L) is centered around 790 nm (805 nm), consistent with the A exciton peak reported in the literature [47]. The PL spectrum of a trilayer flake exhibits a further red-shifted, broadened emission peak with significantly reduced intensity, in agreement with prior observations [130] (direct to indirect band gap crossover). By combining the optical contrast and the PL data, we accurately

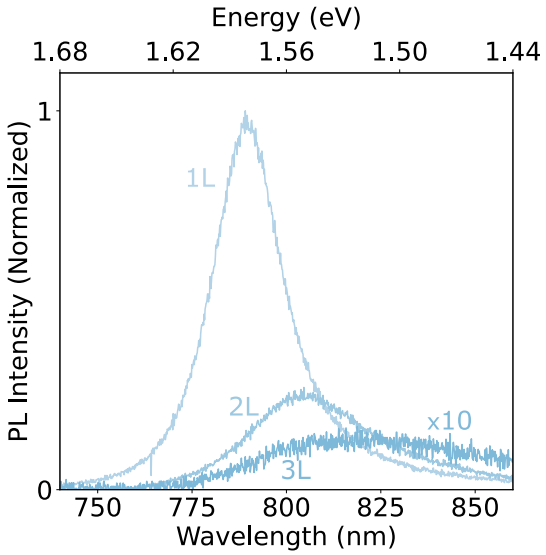


Figure 3.7: Photoluminescense spectra. PL spectra corresponding to the mono-, bi-, and trilayer suspended $MoSe_2$ flakes, normalized to the monolayer intensity. The trilayer spectrum is multiplied by 10 for better comparison.

determined the thickness of 1L, 2L, and 3L flakes, providing unambiguous and consistent results.

Atomic force microscopy

We employ atomic force microscopy to measure the thickness of samples with a thickness greater than 5 layers. Figure 3.8 shows the AFM images of exemplary $MoSe_2$ flakes transferred onto gold-coated substrates. We determine the thickness of the flake by capturing line profiles across the regions of interest using Gwyddion software [131].
We accurately determined the thickness of the prepared samples by combining the data from three methods—optical contrast and photoluminescence for ultrathin films (< 5L), and AFM for thicker (> 5L) samples. Indeed, while the presented data exclusively focuses on $MoSe_2$, it is essential to point out that these techniques have been employed throughout this thesis to accurately determine the thickness of various TMDs studied.

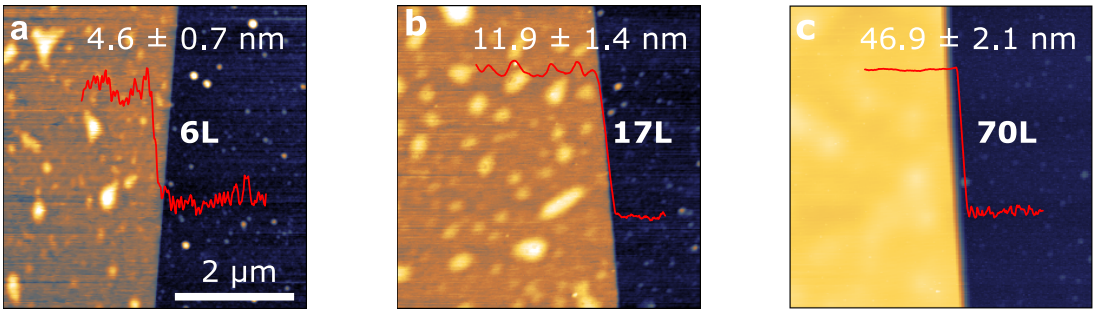


Figure 3.8: Thickness determination using AFM. (**a-c**) AFM images of exemplary $MoSe_2$ flakes transferred onto the gold coated substrates. The line profiles in each panel are the height profiles across the edge of the $MoSe_2$ flakes. The panel (a) scale bar is valid for all three AFM maps.

3.3.2 Roughness and crystallinity

In addition to measuring the thickness, AFM scanning offers the capability to quantify the roughness of the samples. Figure 3.9a shows the 3D topography AFM image of a suspended bilayer $MoSe_2$ at the hole edge as an example for such measurements. We made an interesting observation, revealing an abrupt sagging of the membrane at the edge of the suspended region. This phenomenon has previously been observed [132] and arises from the remarkable ability of atomically thin materials to conform to the nano/microstructures of the substrate underneath [133].

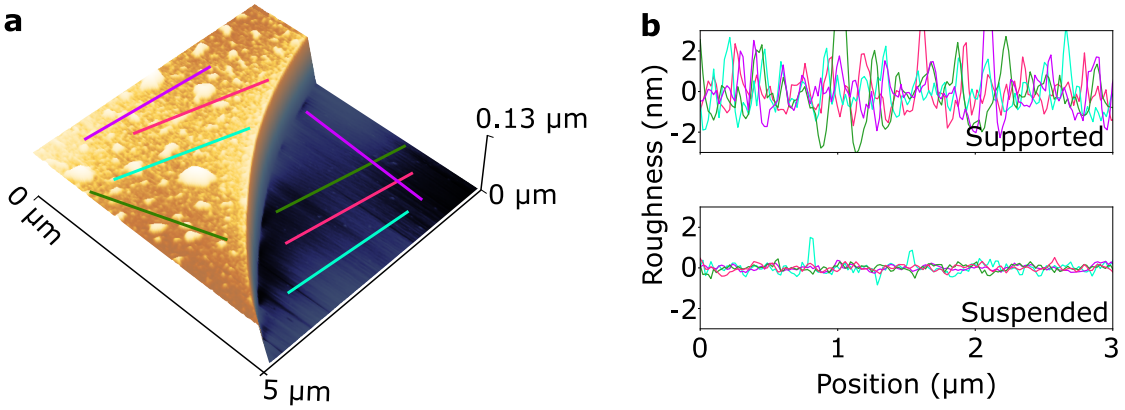


Figure 3.9: Roughness of the transferred flakes. (**a**) AFM 3D topography image at the hole edge showing supported and suspended regions of a bilayer $MoSe_2$ sample and (**b**) their corresponding roughness profiles.

The flake exhibits blisters and a larger roughness in the supported region because it is influenced by the roughness of the substrate. The root mean square roughness (R_q) of the flake in the supported region is 2.8 ± 1.0 nm. In comparison, the surface quality in the suspended region (see Figure 3.9b) is noticeably greater, with an R_q of 0.75 ± 0.25 nm over a 2×2 µm^2 area. This number is in the order of a monolayer thickness (0.7 nm),

implying that the flake is atomically flat. The sub-nanometer roughness spanning several micrometres further demonstrates the absence of any wrinkles on the suspended region.

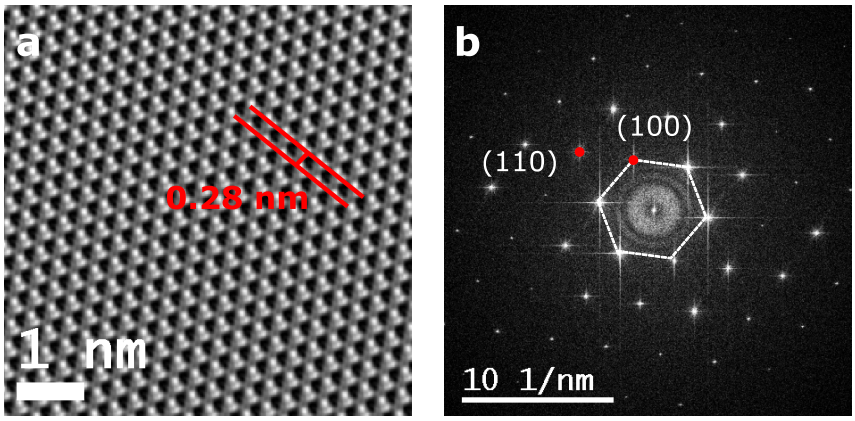


Figure 3.10: High-resolution transmission electron microscopy images. (**a**) HR-TEM images of an exemplary suspended $MoSe_2$ sample. (**b**) FFT of the TEM image showing hexagonal symmetrical patterns of the sample.

We conduct further characterization of the suspended TMD samples using high-resolution transmission electron microscopy (HR-TEM). These HR-TEM images were taken using an ARM-200f (JEOL) at 80 kV, as part of a previous study [134], providing crucial information about the structure and quality of the suspended flakes. The high-magnification TEM image in Figure 3.10a reveals a honeycomb arrangement of atoms, indicating a single-crystalline structure with an interplanar distance of approximately 0.28 nm, consistent with the literature [135]. Figure 3.10b shows the Fast Fourier Transform (FFT) pattern, exhibiting hexagonal symmetrical patterns that confirm the hexagonal lattice structure of the TMD single crystals, verifying the highly crystalline nature of the samples.

3.3.3 Raman: Strain characterization

To extract information about strain in the TMD samples studied in this thesis, we use Raman spectroscopy (spectral resolution of 0.25 cm^{-1}). Raman spectroscopy also allows us to determine the thickness of TMDs by analyzing the relative shifts in the peak positions of Raman active modes [119]. As an example of strain and thickness characterization, we present the results obtained from $MoSe_2$ flakes. To obtain Raman spectra, we use a 532 nm CW laser excitation (same setup as PL measurements). Figure 3.11a shows the A_{1g} mode for $MoSe_2$ flakes with thicknesses ranging from $1-4$L, along with the bulk sample. The A_{1g} peak position for bulk $MoSe_2$ is located at 242.2 cm^{-1}, consistent with previously reported values [136]. As the flake thickness reduces, the A_{1g} mode shifts to a lower frequency, reaching 239.3 cm^{-1} for monolayer $MoSe_2$, in agreement with literature results [137]. This way, we can confirm the flake thickness, obtained from the PL measurements.

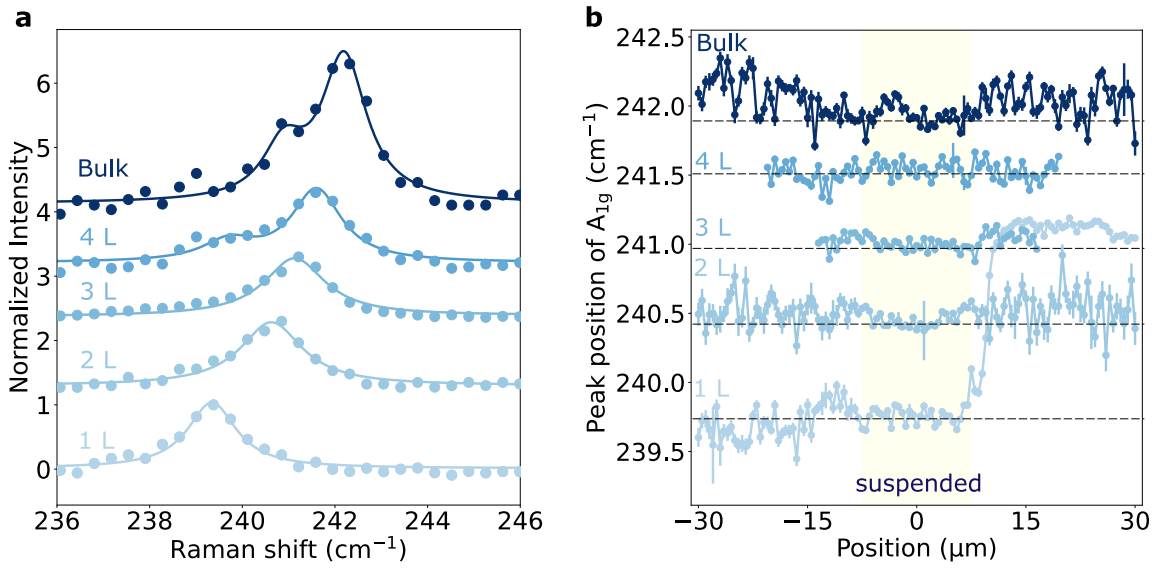


Figure 3.11: Raman spectra of suspended $MoSe_2$ samples. (**a**) Raman spectra of suspended $MoSe_2$ flakes of $1-4$ layers and bulk measured at 532 nm excitation wavelength. The solid lines are double Lorentzian (3L, 4L and bulk) and single Lorentzian (1L and 2L) fits to the Raman spectra. The spectra are shifted up for clarity. (**b**) Peak position of A_{1g} mode across suspended $MoSe_2$ flakes of $1-4$ layers and bulk taken at 3 μW incident power at the sample plane. The shaded area represents the suspended regions. The sudden jump in peak position for the monolayer sample corresponds to a transition from 1 to 3 layers along the scan direction.

To gain insights into strain, we acquire Raman spectra at various sample positions across the suspended region and extract the peak position of the Raman active mode. For $MoSe_2$, we monitor the A_{1g} mode as a function of sample position (see Figure 3.11a). To avoid temperature-induced Raman shifts, we typically use a very low incident power of 3 μW at the sample plane. The frequency of the A_{1g} mode shows minimal variation within the suspended region of the sample, while it exhibits fluctuations in the supported part, close to or within the resolution limit of the spectrometer for the incident power we use (see Figure 3.11b). Hence, we conclude that there are minimal signs of strain-induced shifts within the suspended region.

3.4 Optical measurements

Continuing with our analysis of clean, large-area, unstrained suspended samples, we will now demonstrate accurate optical absorption measurements using these flakes. Specifically, we focus on single wavelength (532 nm) and spectrally resolved absorption measurements (UV-Vis spectroscopy) in $MoSe_2$.

3.4.1 Absorption measurements at 532 nm

We begin with a systematic study of absorption at 532 nm (CW light source) in ambient conditions as a function of sample thickness. Taking advantage of holey substrates as open windows for transmission measurements, we quantify the absorption of the sample by measuring the reflected P_{refl} and transmitted P_{trans} laser power with respect to the incident power P_{inc}, using a calibrated power head (Thorlabs, S130C). We use a pristine substrate as the reference for this measurement. The optical absorbance A of the suspended flake is obtained from the relation $A = 1 - T_{\text{r}} - R = 1 - \frac{P_{\text{trans}}}{P_{\text{inc}}} - \frac{P_{\text{refl}}}{P_{\text{inc}}}$. Figure 3.12a illustrates the resulting absorption A, transmission T_{r}, and reflection R values of the $MoSe_2$ flakes as a function of the number of layers.

The absorption increases with thickness and saturates quickly after 5L. The material becomes quite reflective as the number of layers increases towards the bulk. We measure multiple samples in the $1-4$L regime, and obtain very reproducible R values of $2 \pm 0.2\%$ and $6 \pm 0.2\%$ for 1 and 2L, respectively, with minimal sample-to-sample variations. The reflectivity of TMDs has also been shown to effectively reveal the thickness of each flake [138], increasing from 2% to 20% from 1 to 5 layers. We obtain an absorption of

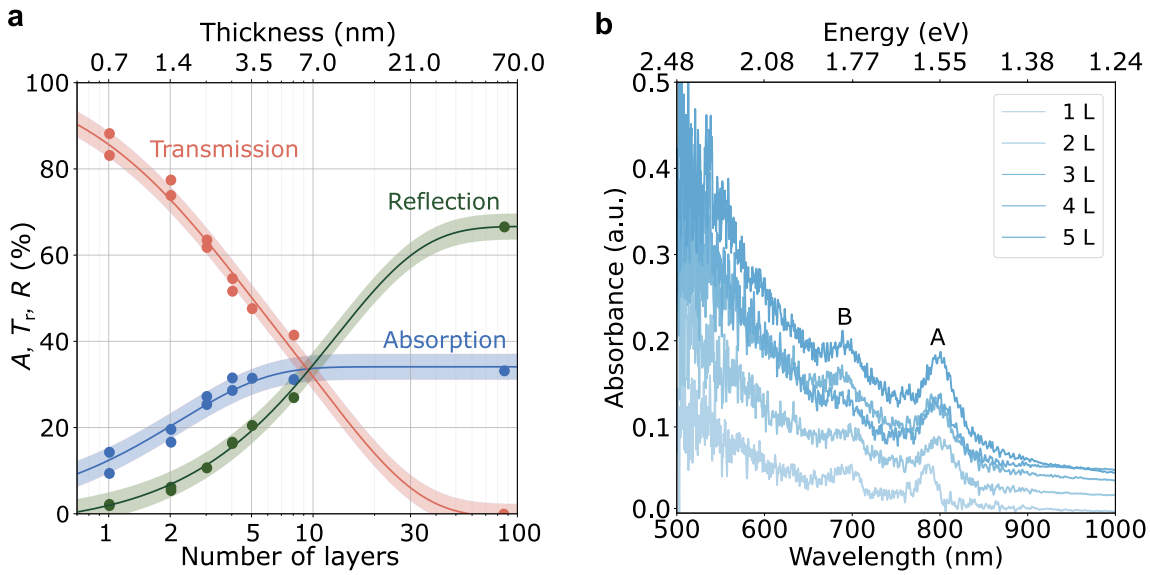


Figure 3.12: Absorption measurements. (**a**) Calculated absorption values from $A = 1 - T_r - R$ at 532 nm, together with measured reflection R and transmission T_r, as a function of $MoSe_2$ flake thickness. (**b**) UV-vis spectra for 1-5 layers suspended $MoSe_2$ flakes.

$10 \pm 3\%$ for the monolayer $MoSe_2$ and $33 \pm 3\%$ for bulk $MoSe_2$. It is important to note that for thicker flakes, internal reflections inside the material can occur [139], resulting in the non-monotonous behaviour of the optical properties as a function of thickness.

Absorption values for mono- and few-layer TMDs in the literature are limited and scattered.

For monolayer $MoSe_2$ supported on SiO_2/Si, an absorption of $23 \pm 8\%$ was estimated at a wavelength of 514 nm [47]. Others have reported values of 5.6% and 9.7% for suspended monolayer and bilayer $MoSe_2$ at 633 nm, respectively [140]. It is worth noting that most literature values are obtained either on supported flakes or flakes suspended over shallow, well-like holes, or on small holes with sizes comparable to the laser spot. In these cases, the absorption is determined using an analysis that depends on knowledge of the complex permittivities of the environment, which may introduce potential errors in the measured absorption values. In contrast, large-area suspended flakes allow for more direct optical absorption measurements that do not necessitate knowledge of any dielectric properties of the environment (substrate).

3.4.2 UV-Vis spectroscopy

We conduct the second optical absorption experiment in the range from visible to near-infrared (500 to 1000 nm), utilizing a commercial UV–Vis spectrometer (Hyperion 2000, Bruker). Figure 3.12b presents the absorption spectra in the measured range for $1 - 5$ layers of suspended $MoSe_2$ samples. Excitation and absorption features in bulk TMD crystals are well-documented, having been extensively studied over several decades [141]. We observe exciton peaks around 700 nm (B-exciton) and 800 nm (A-exciton), consistent with previous studies on $MoSe_2$ [142]. Furthermore, we note a sudden blue shift in the peak position of the A-exciton (for monolayer), as observed in earlier studies [143]. The strength of the spin-orbit interaction (energy difference between the A and B peaks) is approximately 220 meV for $MoSe_2$, in agreement with the literature [144].

PL measurements: Suspended vs supported

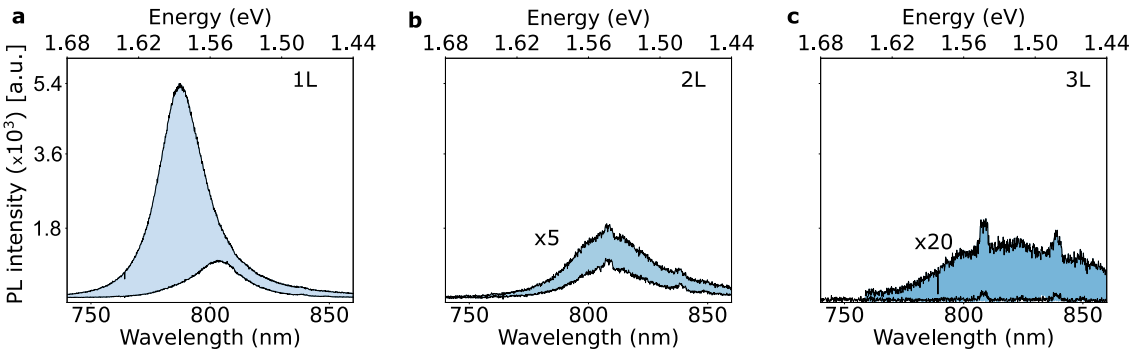


Figure 3.13: Comparison of photoluminescence from suspended and supported regions. PL emission from supported and suspended regions of (**a**) 1L, (**b**) 2L, and (**c**) 3L $MoSe_2$ flakes. The shaded areas represent the PL enhancement on the suspended regions. Datasets presented in panels (b) and (c) are scaled by a factor of 5 and 20, respectively.

Finally, to showcase the benefits of suspended crystals, we perform a comparison of photoluminescence measurements between supported and suspended regions of mono-, bi-, and trilayer $MoSe_2$ flakes. The results clearly indicate that suspended TMDs exhibit brighter emission and the PL signal of the trilayer $MoSe_2$ flake is only detectable in the suspended regions for the laser power we use (see Figure 3.13).

3.5 Summary

In summary, we have developed a fabrication procedure to produce large-area, suspended TMD flakes using standard PDMS-assisted dry-transfer combined with gold-coated commercial substrates having 15 μm-diameter holes. The chapter has included comprehensive measurements to analyze the properties of the suspended samples. Additionally, experimental results on the optical absorption of suspended $MoSe_2$ flakes have been presented, with a focus on how their thickness influences the absorption behaviour. These suspended TMD structures offer significant potential for a variety of applications, including electrical, mechanical, and thermal studies (thesis focus). Their free-standing nature also makes them suitable for applications and studies requiring photon emission with minimal losses.

Contributions

Sebin Varghese and David Saleta Reig built the transfer stage setup, fabricated the samples, and performed the measurements under the supervision of Prof. Klaas-Jan Tielrooij. The HR-TEM images of suspended flakes were shared by Dr Emerson Coy (CNBM-AMU). Sebin Varghese and David Saleta Reig were trained by Dr Marianna Sledzinska and Dr Emidgio Chávez-Ángel to perform Raman spectroscopy measurements. The results were discussed and interpreted together with David Saleta Reig, Dr Jake Dudley Mehew, Dr Alexander Block, and Prof. Klaas-Jan Tielrooij.

Components for building dry-transfer stage

Component	Description	Part Number	Distributor	Price (€)
Optomechanical components	Optical breadboard	B3045A	Thorlabs	598.79
	Stainless steel post	39353	Edmund optics	57.00
	Rack and pinion	03609	Edmund optics	260.00
Zoom lens	2X F-mount Adapter tube	1-62922	Delta optics	487.00
	2X Lens Attachment	1-50015	Delta optics	253.00
	12X zoom motorized	1-51200	Delta optics	3953.00
	10 mm ø fiber input for 12X	2-50751	Delta optics	260.00
	Phase Desktop Enclosure	40234	Delta optics	1260.00
Stages	Linear translational stage (x2)	XR25C/M	Thorlabs	769.72
	Vertical translational stage	MVS005/M	Thorlabs	609.28
	Continuous rotational stage	CR1/M	Thorlabs	306.55
	Translational stage with differential adjuster (x2)	MT1A/M	Thorlabs	748.72
	Dual thread adapter M4 to M6 screw (x4)	AE4M6M	Thorlabs	16.00
	Tilt stage	AIS-60B	OptoSigma	160.30
Illumination	LED point light	ML02221212	Boli optics	152.49
	Adapter plug	EC02411201	Boli optics	9.86
Camera	Canon EOS 6D		FotoK	825.62
	Continuous power supply		FotoK	171.90
	F-mount to Canon EF/E		Gobe	26.00
Temperature control	Thermocouple, K type	405-000	TC direct	15.00
	Temperature Controller	309-103	TC direct	81.00
	Mini transformer	714-1388	RS	15.32
	Solid state relay	102-5544	RS	15.28
	Mini vacuum pumps (x2)	ROB-10398	Electan electronica	33.56
Table	Anti-vibration table	AZ-104008036	Biogen cientifica	925.00
Probe station	Magnetic base (x3)	MB175/M	Thorlabs	140.40
	Solid post (x3)	P100/M	Thorlabs	115.08
	Micro positioner (x2)	XYZ 300 TR	Quarter research	984.815
	Micro positioner	XYZ 300 TL	Quarter research	492.41
	Cable BNC to straight pin (x3)		Quarter research	118.18
	Test needle – Beryllium copper	H-20242-C	Quarter research	45.28
	Source measure unit	P2005A2-EU	Ossilia	1100.00
Total				**15006.56**

Table 3.1: Components for the assembly of our dry-transfer stage, which comes at a cost of 12000 €, inclusive of the anti-vibration table. Additionally, the probe station functionality can be included for an extra 3000 € (Price in 2019).

4

Spatiotemporal pump-probe microscopy: Experimental setup

"Rome wasn't built in a day." - French medieval proverb (English translation)

In this chapter, we introduce the spatiotemporal pump-probe microscopy setup utilized in this thesis for visualizing diffusion processes. We describe the setup, and detail the critical considerations for precise measurements, such as overlapping the pump and probe beams in both space and time. Concluding the chapter, we present a proof-of-concept measurement demonstrating the tracking of hot carrier diffusion in a typical metal, gold.

4.1 Experimental setup: Description and characterization

In this section, we provide a detailed description and characterization of the experimental setup employed in this thesis to study the heat diffusion process. We describe the key components and parameters essential for accurate diffusion measurements and analysis. The basic concept of such time, and space-resolved measurements is illustrated in Figure 4.1a.

4.1.1 General concept

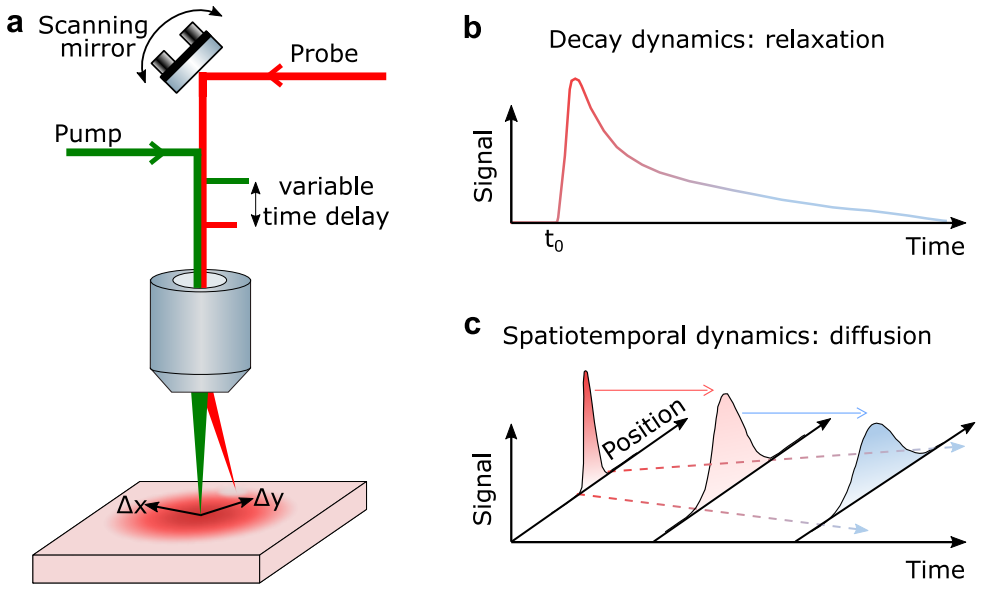


Figure 4.1: General concept of a spatiotemporal pump-probe microscopy experiment. (**a**) Schematics of a time and space resolved experimental setup. An optical pump pulse is focused onto the sample, inducing a localized excitation. (**b**) Schematic illustrating the decay dynamics of the localized excitation at different pump-probe time delays. (**c**) The spreading of the excitation is tracked by scanning the probe beam across the sample, enabling quantification of diffusion. This comprehensive approach provides insights into the dynamics and diffusion processes within the sample. Panels (b, c) are adapted from Ref. [145].

Time-resolved optical measurements are useful for investigating dynamic processes in samples by capturing their responses at precisely controlled time intervals after the photoexcitation. The basic principle involves irradiating a sample with a short optical pulse (pump) and then measuring the resulting changes in its response at specific time delays using a second laser pulse (probe). It allows for the observation of fast dynamic phenomena with temporal resolutions extending down to the attosecond range [146]. During such measurements, the sample's response is recorded as a time-dependent signal. A typical measurement yields a time-dependent signal, where photoexcitation occurs at time-zero (t_0). The result typically is a rapid signal change at t_0, followed by signal

decay, as illustrated in Figure 4.1b. This approach enables the detailed study of transient processes and associated relaxation phenomena within the sample.
Spatiotemporal microscopy adds a spatial degree of freedom to the conventional time-resolved optical measurements, allowing for the observation of both temporal and spatial dynamics of a photoexcited sample (see Figure 4.1a). This technique enables the analysis of how a local photoexcited signal evolves over time and space. In practice, the spatially confined photoexcitation results in a signal that is recorded as a function of both space and time, producing a 2D map. As time progresses, the spatial profile of the signal typically undergoes broadening due to transport processes, such as diffusion (see Figure 4.1c). This broadening, which is observed by examining the changes in the spatial profile over time, provides crucial information about the diffusivity of the material. To determine the diffusion of the local excitation, one can analyze the temporal derivative of squared width evolution (using Equation 2.10) or solve the Fourier heat equation, which will be discussed in the next chapter.
Depending on the transparency of the sample, it is generally possible to measure both transient reflection and transient transmission. Throughout this thesis, we monitor transient reflection $\Delta R/R$, given by,

$$\frac{\Delta R}{R}(x, y, t) = \frac{R_{\text{on}}(x, y, t) - R_{\text{off}}}{R_{\text{off}}} \tag{4.1}$$

where R_{on} and R_{off} are the reflected probe signal when the pump is on and off, respectively, to quantify diffusion in different materials under study.

4.1.2 Experimental setup

The schematic of the experimental setup employed for these measurements is illustrated in Figure 4.2. Our primary laser source, the FLINT from Light Conversion, emits pulses with a duration of approximately 120 fs at a wavelength of 1030 nm, delivering an output power of approximately 14 W with a repetition rate (f_{rep}) of 76 MHz. We direct the majority of this laser output (80%) towards an optical parametric oscillator (OPO), which produces a tunable idler output ranging from 2150 to 4800 nm and a signal output ranging from 1320 to 2000 nm. This signal output enters a HarmoniXX (APE) system to generate the second and third harmonics of the signal wavelength. Meanwhile, the remaining 20% of the FLINT output (at 1030 nm) is directed through a lithium triborate (LBO) crystal to generate the second harmonic (515 nm) of the fundamental laser source.
In our experimental setup, we can have two different configurations. In one configuration, we use the second harmonic of FLINT output (515 nm) as the pump beam. The probe beam is either the second or third harmonics output of the HarmoniXX. This configuration

adds an important feature to the experimental setup. By fixing 515 nm as the pump beam, we can now tune the probe from approximately 500 nm to nearly 1000 nm (outputs of HarmoniXX), by varying the signal output of the OPO. This flexibility allows us to study various materials, such as transition metal dichalcogenides (TMDs), whose exciton resonances are within this range. We use such an experimental configuration for the measurements performed in this thesis unless otherwise mentioned. In the other configuration, we use the outputs of HarmoniXX as the pump and the probe beam. Specifically, the second harmonic acts as the probe beam, while the third harmonic functions as the pump beam. For instance, with a 1600 nm OPO signal output, the probe beam is 800 nm and the pump beam is 533 nm.

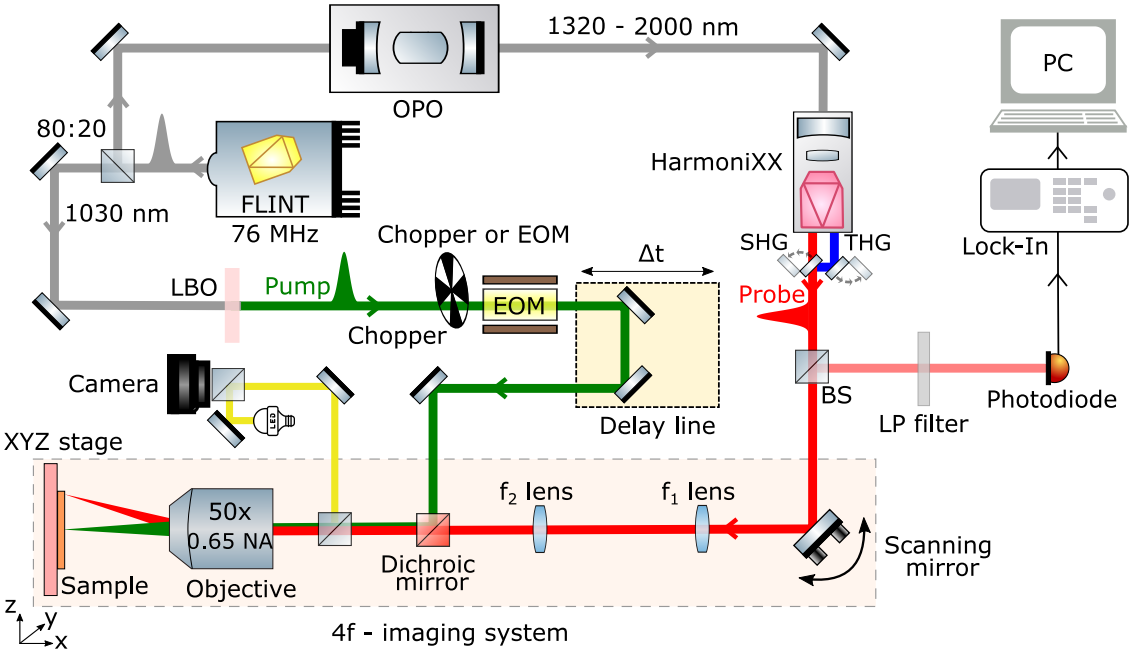


Figure 4.2: Detailed schematic of spatiotemporal pump-probe microscopy setup. The fundamental laser source (FLINT) generates an output at 1030 nm which we use to obtain the pump and the probe beam. The pump beam is sent through a mechanical delay line and combined with the probe beam using a dichroic mirror. The probe beam is directed using a scanning mirror system and later combined with the pump and focused on the sample plane. The reflected probe is filtered and detected using a longpass filter and silicon photodiode, respectively. A detailed description is provided in the main text. LP filter: longpass filter, BS: beam splitter, SHG (THG): second (third) harmonic generation.

An optical chopper (MC1F10HP, Thorlabs) modulates the pump beam, regulating the pump modulation frequency (up to 10 kHz), before being directed onto a variable delay line (DL225, Newport). For modulation frequencies exceeding 10 kHz, we replace the optical chopper with a free-space electro-optic modulator (EO-AM-NR-C4, Thorlabs). We guide the probe beam using a scanning mirror system (OIM 101, Optics in Motion) and f_1-f_2 lenses, and then combine it with the pump beam using a dichroic mirror (DMLP550

or DMLP650, Thorlabs).
After combining the pump and probe beams at the dichroic mirror, we focus them onto the sample stage (XYZ stage, Standa) using a 50x microscope objective lens (the PAL-50-NIR-HR-LC00 from OptoSigma, or the LCPLN50XIR from Olympus[†]). To filter the pump light reflected from the sample, we use longpass filters (using FELH0550 or FELH0650, Thorlabs), and direct the reflected probe light to a silicon photodiode (DET10A2, Thorlabs). This photodiode is connected to a synchronized lock-in amplifier (MFLI 500 kHz, Zurich Instruments), which demodulates the detected probe signal at the pump modulation frequency to obtain the transient reflectivity signal. We use a white LED and camera setup to observe the sample. A bird's eye view of the setup is shown in Figure 4.3. We

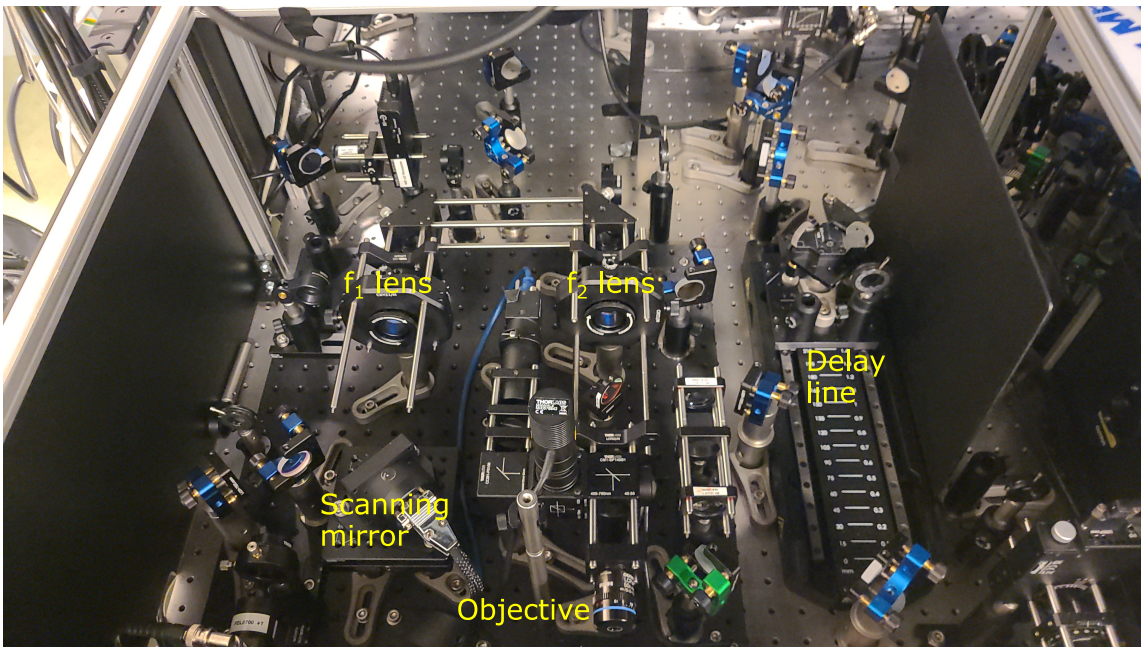


Figure 4.3: A bird's eye view of the spatiotemporal pump-probe microscopy setup in our laboratory.

also built a second spatiotemporal setup using the SuperK laser system (FIU-6, NKT Photonics), which has a temporal resolution of tens of picoseconds and a tunable repetition rate ($0.15 - 78$ MHz).

4.1.3 Beam overlapping and spatial scanning

To perform spatiotemporal measurements with high temporal and spatial resolution, it is important to thoroughly characterize the setup beforehand, including overlapping the beams and calibrating the scanning mirror.

[†]This is a correction collar objective, which allows for compensation of cover glass thickness variations (e.g. while measuring in vacuum).

Spatial overlap

To obtain the best signal level in the measurement, it is important to spatially overlap the pump and probe in all three dimensions. Here, we will explain how this is achieved. A

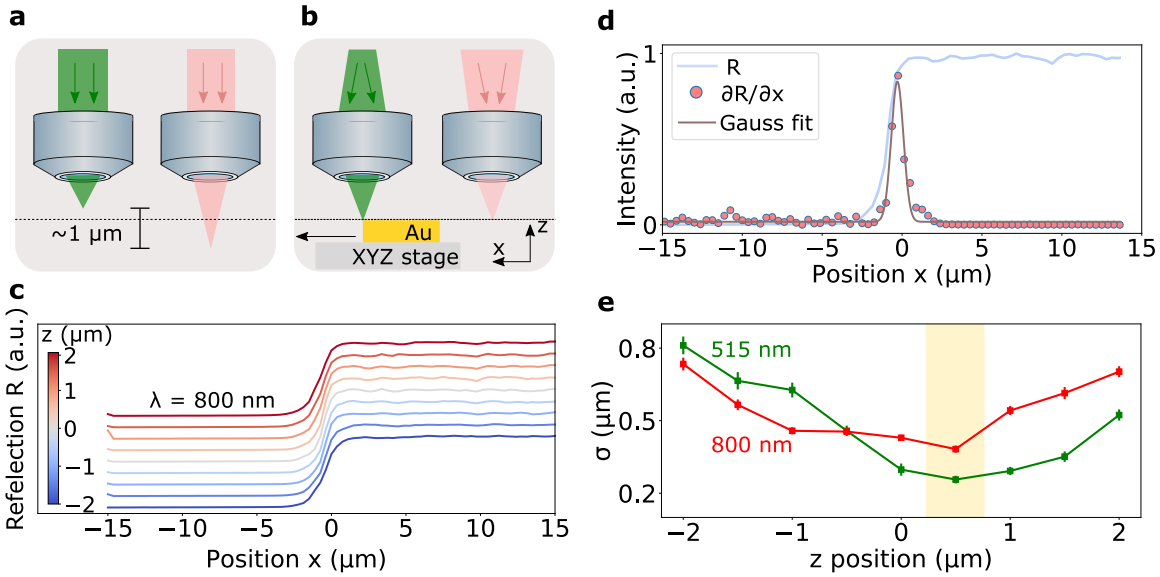


Figure 4.4: Beam profiling and overlapping by knife-edge method. (**a**) Chromatic aberration causes micrometer-scale variations in the focal z-position for different wavelengths. (**b**) Through beam profiling and iterative adjustment of collimation, the beam focuses can be aligned to achieve improved overlap. Adapted from [147]. (**c**) An exemplary knife-edge measurement for 800 nm performed at a sharp metal (Au) edge while tracking the reflection signal as a function of z-position. (**d**) From the Gaussian fit (light brown line) to its derivative (scatters) we extract the width of the beam. (**e**) Width of both beams at different z-positions. The shaded region indicates the overlap of the beams in the z-dimension.

coarse overlap in the lateral dimensions (x, y) is first achieved by carefully aligning the incoming beams to overlap in both position and angle upon entering the back aperture of the objective. This is usually done by imaging the reflected light from a sample and adjusting the final two mirrors to make the reflected beam shape symmetric (and overlapped).

However, in the z-direction, challenges arise due to the chromatic aberration exhibited by various optical elements along the beam path, including the microscope objective. In particular, the collimated pump and probe beams often display a different focal length, typically differing by a few micrometres, as shown in Figure 4.4a. To address this discrepancy, it becomes important to slightly de-collimate one or both beams to ensure they converge at the same z-position, see Figure 4.4b. This is done by slightly moving the collimation lenses in the beam paths, for example, f_2 lens (see Figure 4.2) in the probe beam path.

To accurately estimate and correct the z-offset, we employ a knife-edge method [148],

which involves measuring the beam profile as a function of z-position. Here, we track the reflection profile of each beam across a very sharp metal edge, see Figure 4.4b,c. Such a measurement is repeated for the y-direction as well (not shown). To determine the spot size, we take the spatial derivative of the reflection profile and fit a Gaussian function (see Figure 4.4d) to it. By analyzing all the z-slices similarly, we determine the z-position where the Gaussian fit to the derivative has the minimum width, which represents the best focus (see Figure 4.4e). Here, we show the results after several iterations of beam profiling and slight adjustments of the collimation lenses in the beam path, yielding the sigma (σ) parameter (standard deviation) of the Gaussian fit as 0.26 µm and 0.36 µm for pump (515 nm) and probe (800 nm), respectively.
Afterwards, we achieve fine spatial alignment by maximizing the transient signal through subtle adjustments to the probe beam's position using the scanning mirror. Now, both beams are overlapped in all the spatial dimensions which is a requirement to obtain high signal-to-noise in spatiotemporal transient microscopy measurements. We perform spatial overlap frequently, which includes instances such as changing the wavelength, making slight adjustments to the optical components, or when changing the sample.

Temporal overlap

We benefit from our 225 mm delay line and employ a straightforward methodology to establish the temporal overlap (time-zero) between the pump and probe beams. This involves measuring the distance travelled by both beams to the sample stage, ensuring that both beams travel approximately the same distance. By conducting a pump-probe delay scan across the entire range of the delay line, we successfully identify the time-zero position. We recognize this time-zero point by observing a distinct peak in the temporal dynamics of the sample, see Figure 4.5. For this purpose, we utilize a 50 nm gold-coated quartz substrate[‡].
In Figure 4.5b, we convert the delay line position to time delay, where 1 mm corresponds to approximately 6.67 ps (which equals $2 \times \frac{1\text{ mm}}{c}$), where c is the speed of light. This conversion allows us to depict three distinct regimes in time delay. Firstly, when $\Delta t = 0$, the pump and probe pulses arrive simultaneously at the sample plane. This is marked by a sharp rise in the signal level. Secondly, for $\Delta t > 0$, the probe arrives after the pump pulses in a pump-probe pulse pair. The maximum time delay in this scenario is constrained by the length of the delay line (for instance, a 225 mm delay implies 1.5 ns). This enables us to study the decay dynamics of the excited carriers. Lastly, for $\Delta t < 0$, the probe arrives before the pump pulse in the pump-probe pulse pair, effectively evaluating the effect of

[‡]As decay dynamics for thick TMDs are much slower than gold, it will be even easier to use a TMD flake to find the time-zero position on a delay line.

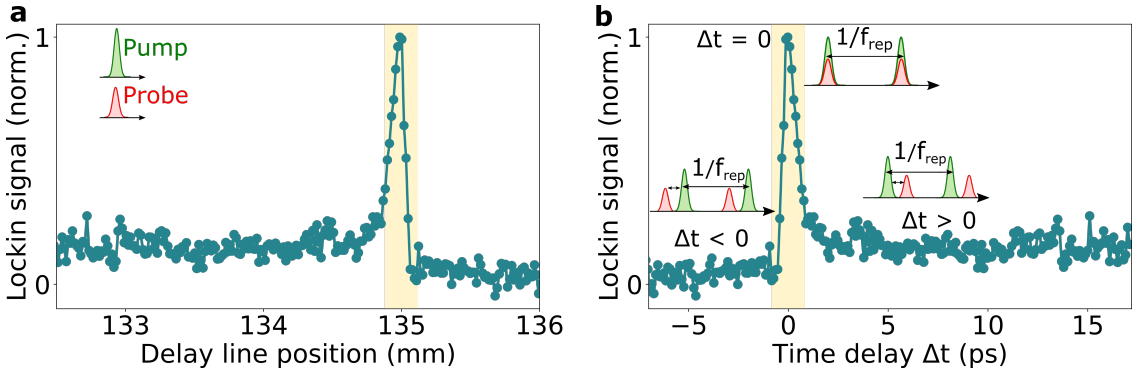


Figure 4.5: Temporal dynamics. (**a**) Decay dynamics measured on gold to identify the time zero (shaded region) position on the delay line. Pump wavelength $\lambda_{pu} = 515$ nm, probe wavelength $\lambda_{pr} = 800$ nm. (**b**) A schematic illustrating different time delay scenarios is depicted, with the delay line position in panel (a) converted to the temporal axis.

the previous pump pulse on the sample. Here, the maximum time delay is set by the repetition rate of the laser (for instance, a f_{rep} of 76 MHz corresponds to Δt of 13 ns). In the case of layered semiconductors, at nanosecond timescales, electronic excitations have relaxed into phonon heat [149], so the signal at that timescale corresponds to the phonon-induced change in reflection/transmission. Further discussion of this case will be provided in the forthcoming chapters of this thesis. Apart from the simpler approach described here, other methods to find temporal overlap include monitoring the beams with a fast photodiode or employing time-correlated single photon counting [150].

Scanning mirror system

To independently control the movement of the probe beam relative to the pump beam, we utilize a scanning mirror, configured in a 4-f imaging system. In this setup, two lenses with focal lengths f_1 and f_2 are placed between the scanning mirror and the objective lens (f_{obj}). This arrangement ensures that even small translations of the scanning mirror result in proportional translations at the back aperture of the objective, maintaining the same focal plane (see Figure 4.6).

Utilizing ray transfer matrix analysis or ABCD matrix analysis, we can comprehensively understand the propagation of beams through the imaging system towards the sample. By applying these analytical tools, we can predict the final position x_o (and angle ϕ_o) of the probe beam from the input position x_i (and angle ϕ_i) at the sample plane as follows [151, 152],

$$\begin{pmatrix} x_o \\ \phi_o \end{pmatrix} = \begin{pmatrix} A & B \\ C & D \end{pmatrix} \cdot \begin{pmatrix} x_i \\ \phi_i \end{pmatrix} \tag{4.2}$$

where A and D are the scaling factors along the transverse axes. B and C represent

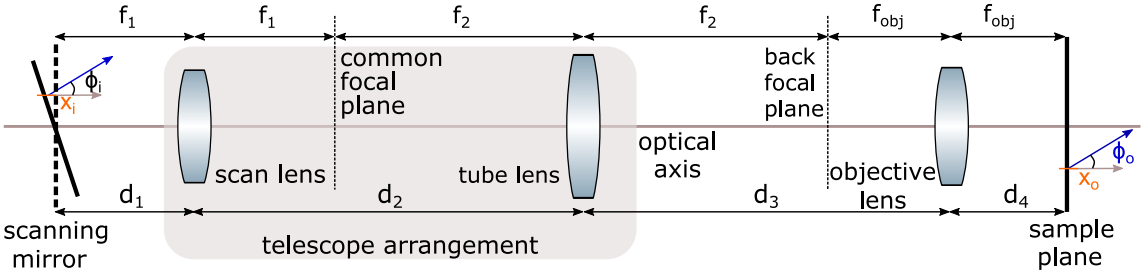


Figure 4.6: Schematics illustrating 4-f imaging system. With this type of arrangement, the scanning mirror controls the input beam angle ϕ_i, translating it into the sample plane displacement x_o while maintaining the beam aligned with the optical axis at the back focal plane of the objective.

any optical aberrations, tilts, or translations introduced by the optical system. The determinant of the matrix $(AD - BC)$ represents the overall magnification or compression of the optical system. Such transfer matrix for a free space propagation with a distance of d (denoted $\mathrm{M_d}$) as and for a thin lens with focal length f (denoted as $\mathrm{M_f}$) are given by the following forms:

$$\mathrm{M_d} = \begin{pmatrix} 1 & d \\ 0 & 1 \end{pmatrix} \quad \text{and} \quad \mathrm{M_f} = \begin{pmatrix} 1 & 0 \\ -1/f & 1 \end{pmatrix} \tag{4.3}$$

Incorporating both free space propagation and optical elements, such as lenses, the final ABCD matrix (M) of the system is determined by the product of individual ABCD matrices,

$$\mathrm{M} = \mathrm{M_{d_4}} \cdot \mathrm{M_{f_{obj}}} \cdot \mathrm{M_{d_3}} \cdot \mathrm{M_{f_2}} \cdot \mathrm{M_{d_2}} \cdot \mathrm{M_{f_1}} \cdot \mathrm{M_{d_1}} \tag{4.4}$$

By substituting the matrix elements, the above Equation 4.2 simplifies to the following form,

$$\begin{pmatrix} x_o \\ \phi_o \end{pmatrix} = \begin{pmatrix} 0 & -\frac{f_{obj} f_1}{f_2} \\ \frac{f_2}{f_{obj} f_1} & 0 \end{pmatrix} \cdot \begin{pmatrix} x_i \\ \phi_i \end{pmatrix} \tag{4.5}$$

The vanishing diagonal elements of the final ABCD matrix M is a consequence of placing the lenses in a conjugated condition, $d_1 = f_1$, $d_2 = f_1 + f_2$, $d_3 = f_2 + f_{\mathrm{obj}}$, and $d_4 = f_{\mathrm{obj}}$ (see, Figure 4.6). Now, the position of the beam at the sample plane is expressed as,

$$x_o = -\frac{f_{obj} f_1}{f_2} \phi_i \tag{4.6}$$

and is dependent on the scanning mirror angle. The focal length of the objective is

expressed as $f_{\mathrm{obj}} = L_{\mathrm{i}}/(m+1)$, where L_{i} is the image distance (often specified by objective manufacturers) and m is the magnification. The angles of the scanning mirror are mapped to angles at the back focal plane of the objective. If $f_2 > f_1$, they are magnified by the ratio f_1/f_2, which is smaller than one. From Equation 4.5, we can also obtain the full scan angle $2\phi_{\mathrm{i}_{\mathrm{max}}}$ of the scanning mirrors as,

$$2\phi_{\mathrm{i}_{\mathrm{max}}} = \frac{f_2 2x_{\mathrm{o}_{\mathrm{max}}}}{f_1 f_{\mathrm{obj}}} = \frac{R_{\mathrm{a}} f_2}{f_1 f_{\mathrm{obj}}} \tag{4.7}$$

where R_{a} is the full range of possible sample positions. In all the experiments performed in this thesis, we use an f_1 lens with a focal length of 150 mm and an f_2 lens with a focal length of 250 mm. For the OptoSigma objective ($f_{\mathrm{obj}} = 4$ mm) with 50x magnification, and a full scan angle of 3 degrees (≈52 mrad) of our scanning mirror, the probe beam scans around 120 μm at the sample plane. Equation 4.7 also provides the scanning resolution of the 4-f imaging system. By utilizing the angular resolution of our scanning mirror (< 2 μrad), we estimate the scanning resolution to be around 5 nm for our experimental configuration.

Scanning mirror calibration

In spatiotemporal pump-probe microscopy, achieving precise measurements relies on an accurate calibration of the scanning mirror. This calibration process ensures that applied voltages to the scanning mirror directly translate to precise displacements in the sample plane.

As a first step, we prepare a calibration sample, typically consisting of nanopillars spaced at known distances. Figure 4.7a shows the reflection map recorded at 800 nm probe wavelength of a few such nanopillars. We then fit the reflection profile using multiple Gaussian peaks, see Figure 4.7b. With the known spacing (center-to-center) between nanopillars designed at 3 microns, we establish a correlation between the applied driving voltage and the resulting displacement in the sample plane.

We also employ the same approach, using another calibration sample: a commercial holey substrate (NTPR005D-C15, Norcada) with a known hole size of 15 microns. In this method, akin to the calibration with fabricated nanopillars, we analyze the reflection profile (see Figure 4.7c) to determine the voltage-to-micron conversion factor. This is done by taking the line profile across different directions and comparing it to the known distance of 15 microns. This approach provides an alternative yet reliable means of calibrating scanning mirrors for precise spatial mapping in spatiotemporal pump-probe experiments. Both approaches yielded similar results within a few percent, likely attributed to differences in fabrication processes. We opted for commercial substrate calibration, as the samples utilized in this thesis were fabricated on such substrates.

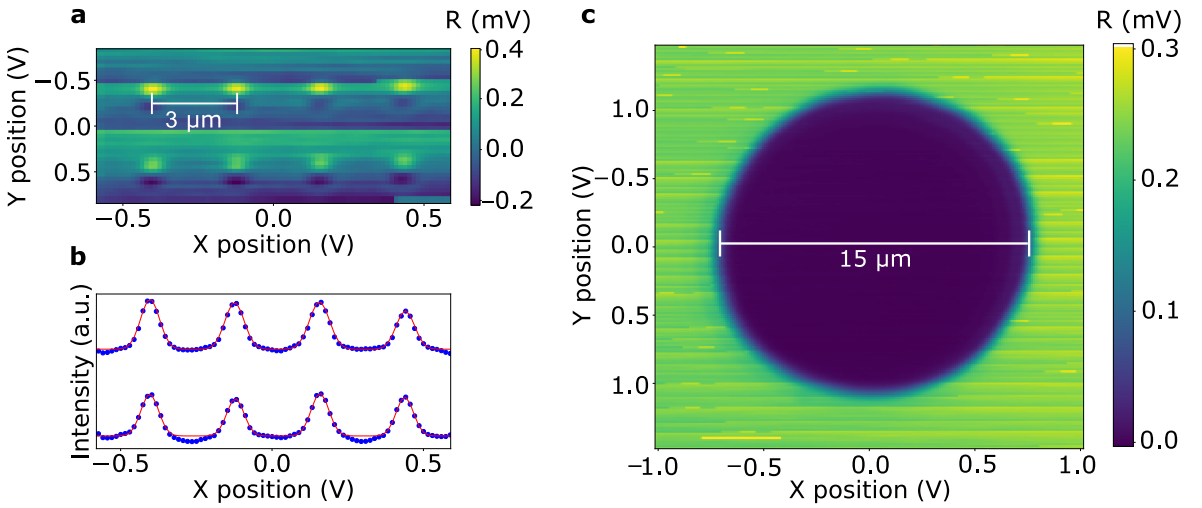


Figure 4.7: Scanning mirror calibration. (**a**) Reflection map (axes in units of volts V) at probe wavelength 800 nm of a gold nanopillar sample. (**b**) Line-cuts (blue scatters) of the reflection map in (a) fitted with multiple Gaussian peaks (solid red line) to determine the voltage-to-micron conversion value. (**c**) Reflection map of a commercially fabricated holey substrate from Norcada.

4.2 Tracking diffusion on gold

To demonstrate the setup's functionality, we present our initial proof-of-concept and a concrete example of spatiotemporal pump-probe experiments. Inspired by the findings reported in Ref. [153], where the spatiotemporal pump-probe technique was employed to investigate the hot electron diffusion in 50 nm gold, we sought to replicate these results. Utilizing the same sample, we conduct measurements to examine hot electron diffusion dynamics. We use a 515 nm pump (fluence $f_{\text{pu}} \approx 0.9$ mJ/cm^2)[§], modulated at 4.37 kHz, and a probe of 800 nm for these measurements.

Figure 4.8a shows transient reflectivity $\Delta R/R$ profiles at a few different time delays. These profiles depict the temporal decay and diffusion of the signal. By fitting the spatial profiles with Gaussian functions, we extract the sigma parameter and plot the resulting temporal evolution of squared width (σ^2) (see Figure 4.8b). Utilizing Equation 2.10, we determine the diffusion coefficient of the sample.

Consistent with the observations reported in Ref. [153], our analysis outlines two distinct regimes: an initial phase characterized by rapid diffusion within the first few picoseconds, followed by a slower diffusion process. Specifically, we find that the fast diffusion D_{fast} value is 59.8 ± 6.7 cm^2/s, while the slow diffusion D_{slow} rate is 1.4 ± 0.6 cm^2/s (see Figure 4.8b). This phenomenon is attributed to the initial stage of hot-electron diffusion, succeeded

[§]In this thesis, we quantify fluence from laser repetition rate $f_{\text{rep}} = 76$ MHz, $1/e$ radius of the Gaussian beam at the focus $r_{1/e}$, and averaged power P_{avg} measured at the sample plane, and is given by, $f = P_{\text{avg}}/(f_{\text{rep}} \cdot \pi \cdot r_{1/e}^2)$.

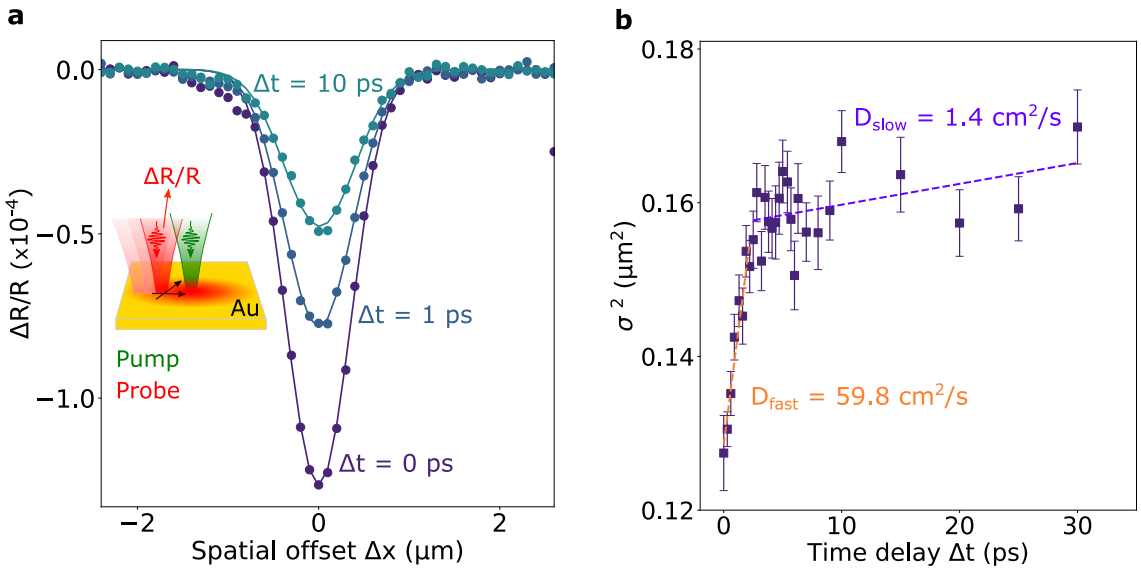


Figure 4.8: Diffusion dynamics in gold. (**a**) Transient reflectivity $\Delta R/R$ recorded by scanning the probe beam over the pump spot at a few different time delays. The solid lines are the single Gaussian fit to the data. The inset shows the schematics of the experiment. (**b**) Evolution of the squared width (extracted from the Gaussian fit), for each pump-probe delay (scatters). The initial fast and subsequent slow diffusion coefficients are extracted by fitting the slopes in the two regions (using Equation 2.10). We obtained $D_{\text{fast}} = 59.8$ cm^2/s (orange dashed line) and $D_{\text{slow}} = 1.4$ cm^2/s (violet dashed line). The error bars show 68% confidence interval of the Gaussian fits.

by the slow phonon diffusion process [153]. These results serve as compelling evidence that our setup can resolve nanoscale ultrafast diffusion dynamics with high precision and accuracy.

We further evaluate the spatial accuracy of our setup using the fitted spatiotemporal profiles shown in Figure 4.8. This assessment involves extracting the error bars associated with the width parameter (σ) of the Gaussian fits. We use the average error in the fitting (at all time delays measured) as an indicator of our spatial accuracy, which we determine to be approximately 12 nm for our experimental configuration. This value is very close to the spatial scanning resolution of the scanning mirror (5 nm), indicating that our setup is limited by signal-to-noise ratio, rather than the scanning mirrors. The accuracy (12 nm) we obtain closely resembles the findings in Ref. [153]: 20 nm and Ref. [154]: 10 nm.

4.3 Summary: Outlook to study heat transport

In this chapter, we have discussed in detail the experimental setup employed in this thesis and addressed crucial considerations for observing diffusion processes through spatiotemporal pump-probe microscopy. We have also explained key experimental procedures, in particular, those that ensure spatial and temporal overlap. These are essential to perform

spatiotemporal pump-probe measurements. As a proof-of-concept experiment, we have measured spatiotemporal dynamics to study hot-carrier diffusion in gold. We will use this technique to investigate nanoscale heat transport properties in TMDs, as detailed in the forthcoming chapters. By taking advantage of the pre-time-zero signal ($\Delta t < 0$), we will examine very long time delays ($\Delta t = 13$ ns), where electronic excitations have relaxed into phonon heat, to study the heat transport.

Contributions

Sebin Varghese and Dr Jake Dudley Mehew built the spatiotemporal pump-probe microscopy setup with inputs from Dr Alexander Block. Sebin Varghese and Afroditi Koutsogianni built the second spatiotemporal pump-probe microscopy setup with inputs from Dr Jake Dudley Mehew. Dr Jake Dudley Mehew fabricated the nanopillar sample. Sebin Varghese performed the measurements and analyzed the data reported in this chapter under the supervision of Prof. Klaas-Jan Tielrooij.

5

Spatiotemporal thermometry: Quantifying heat diffusion in bulk TMDs

"The longer you can look back, the farther you can look forward." - Winston Churchill

In this chapter, we present the previously detailed spatiotemporal pump-probe microscopy technique to quantify the thermal diffusion in transition metal dichalcogenides (TMDs) in a direct fashion. Our technique is sensitive to the temperature profile via the transient reflectivity when probe pulses arrive before pump pulses within the pulse train. This effectively establishes a pump-probe time delay of 13 ns, determined by the repetition rate of our laser system (76 MHz). A distinctive benefit of this technique is its ability to quantify thermal transport without the need for specific material input parameters or significant heating. We validate the efficacy of our technique by the direct determination of the thermal diffusivity (D) of four prototypical TMDs — $MoSe_2$ (0.18 cm^2/s), WSe_2 (0.20 cm^2/s), MoS_2 (0.35 cm^2/s), and WS_2 (0.59 cm^2/s).

This chapter is based on the following publication (Editors Pick):

S. Varghese, J. D. Mehew, A. Block, D. Saleta Reig, P. Woźniak, R. Farris, Z. Zanolli, P. Ordejón, M. J. Verstraete, N. F. van Hulst, and K. J. Tielrooij. A pre-time-zero spatiotemporal microscopy technique for the ultrasensitive determination of the thermal diffusivity of thin films, Review of Scientific Instruments, 94, 034903 (2023) [155].

5.1 Introduction

Numerous experimental techniques, both electrical and optical, have been devised to measure the thermal transport properties of nanoscale materials. Electrical methods, such as the 3ω [156] and suspended micro-bridge [157] methods, offer precise measurements but often require complex setups and/or sample preparation.

Optical techniques, on the other hand, have gained attention for their non-contact nature. For example, optothermal methods based on steady-state Raman spectroscopy [13], and transient optical techniques, including time-domain thermoreflectance (TDTR) [40], frequency-domain thermoreflectance (FDTR) [41], and time-resolved transient grating (TTG) [43] have been used for the measurement of thermal transport properties of various material systems. However, these techniques have limitations. They typically require accurate knowledge of the material parameters, such as thickness, optical absorption and heat capacity, and in some cases, such as Raman thermometry, need relatively strong heating ($\Delta T \approx 100$ K) [36].

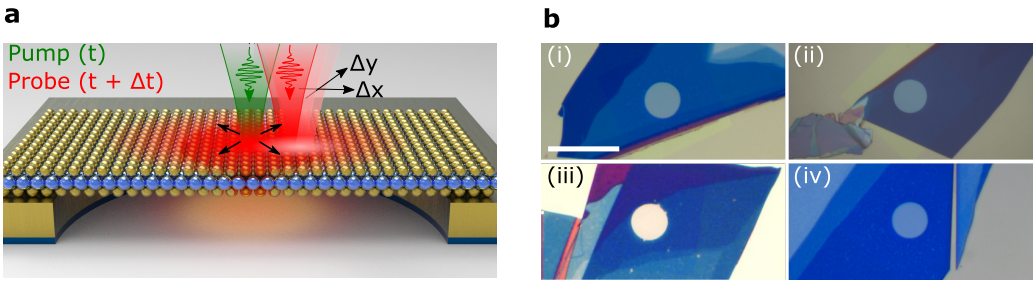


Figure 5.1: Schematics of the thermal diffusivity measurements and investigated samples. (a) Schematics showing pump-probe measurements performed on a suspended sample[†]. An optical pump pulse heats the suspended region, and the evolution of this heat is tracked spatiotemporally. **(b)** The microscope image of suspended samples studied – (i) $MoSe_2$, (ii) WS_2, (iii) WSe_2, and (iv) MoS_2, all having thickness around 15 nm. The scale bar (30 µm) in (i) is valid for all the images.

Here we overcome these limitations by introducing a novel approach, named spatiotemporal pump-probe thermometry, based on the experimental setup detailed in the previous chapter. This technique enables us to determine the in-plane thermal diffusivity by examining the spatial profile at a small negative pump-probe delay time Δt. Here, the probe pulses arrive before the pump pulses, allowing sensitivity to residual heat generated by prior pump pulses in the pulse train (effectively, $\Delta t = 13$ ns). The key thing is that in this way we are not sensitive to electronic transport. The measurements involve locally heating the center of the suspended region of the sample with a pump beam and monitoring the evolution of

[†]This is an artistic illustration (also Figure 6.1b) and does not accurately represent the crystal structure.

this heat using a probe beam both spatially and temporally (see Figure 5.1a).
In the rest of this chapter, we will dive deep into how this method works, showing its capability to accurately quantify heat transport in thin films. In particular, we demonstrate the working principle of our method by quantifying the thermal diffusivity D of four TMD materials (see Figure 5.1b), each with a thickness of around 15 nm.

5.2 Temporal dynamics

The first step towards measuring spatiotemporal transport is to observe the temporal decay dynamics of the sample. Figure 5.2a-d shows the transient reflectivity $\Delta R/R$ signal on the suspended and supported regions, for $MoSe_2$, WSe_2, MoS_2 and WS_2. We use a pump wavelength of 515 nm and set the probe wavelength to the exciton resonance of each TMD (see also Figure 5.3). In these measurements, we spatially overlap the pump and probe beam: $\Delta x = \Delta y = 0$. We perform all the measurements reported in this chapter under ambient conditions and at a pump fluence between $0.03 - 0.04$ mJ/cm^2, unless mentioned otherwise.

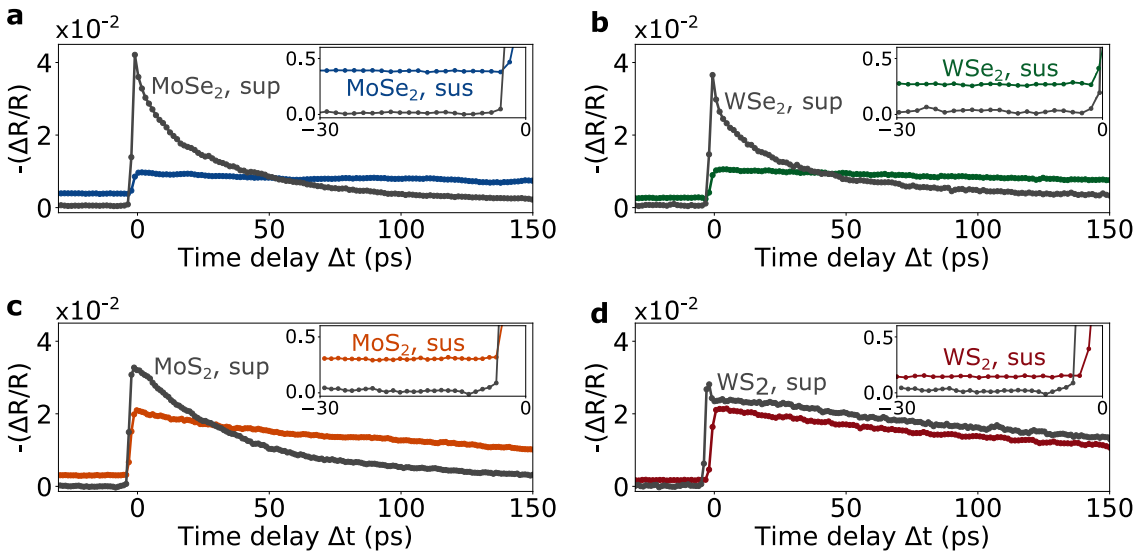


Figure 5.2: Decay dynamics of TMDs. (a-d) Comparison of transient reflectivity dynamics in suspended (sus) and supported (sup) regions of (a) $MoSe_2$, (b) WSe_2, (c) MoS_2, and (d) WS_2. Insets show a zoomed-in view of the signal before time-zero, i.e., $\Delta t = 13$ ns.

In both regions, we observe signal peaks occurring at $\Delta t = 0$ ps. We attribute this to the photoexcitation of charge carriers and the rapid formation of excitons [158]. Focusing on the substrate-supported region, we observe a gradual decay of the pump-probe signal over picosecond timescales. This indicates a reduction in the exciton population, which can be attributed to several processes. These include radiative recombination, where an electron-hole pair recombines and emits a photon, exciton-exciton annihilation, where two

excitons annihilate each other, non-radiative recombination, and energy transfer to lattice vibrations or phonons [159, 160]. Importantly, the signal approaches near-zero levels within the temporal window provided by our delay line (150 ps) and reaches zero, as evidenced by the signal at $\Delta t < 0$. This indicates that the system returns to an equilibrium state before the arrival of subsequent pump pulses. As described in Subsection 4.1.3, the situation at $\Delta t < 0$ corresponds to a time delay of 13 ns, as set by the repetition rate (76 MHz) of our laser.

In contrast, the suspended region has a noticeable residual signal at $\Delta t < 0$ (see Figure 5.2a,b). We attribute this phenomenon to the accumulation of phonon-induced heat within the sample. This phenomenon is absent in the supported regions, owing to the efficient out-of-plane heat dissipation facilitated by the gold-coated substrate.

5.3 Emergence of long-lived signal

5.3.1 Dependence on probe wavelength

To validate that the $\Delta t < 0$ signal correlates with a phonon-induced change in probe reflection, we assess the signal variation across probe wavelengths (see Figure 5.3). From now on, will call the pre-time-zero signal ($\Delta t < 0$) as a time delay Δt of 13 ns. Notably,

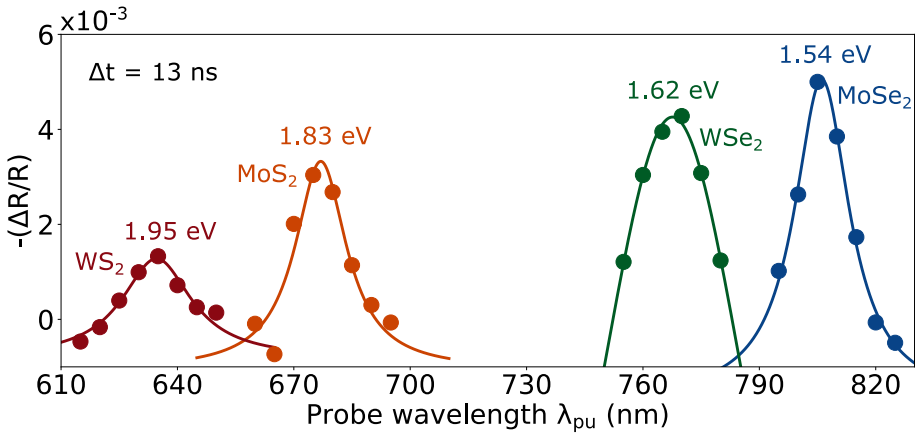


Figure 5.3: Probe wavelength dependence of $\Delta R/R$. $\Delta R/R$ signal at $\Delta t = 13$ ns measured at different probe wavelengths with a fixed incident pump fluence $f_{pu} \approx 0.03$ mJ/cm^2. The peak response corresponds to the A exciton resonance of the materials. The solid line is a Lorentzian fit to the data.

distinct peaks emerge at wavelengths of 635 nm (1.95 eV), 675 nm (1.83 eV), 770 nm (1.62 eV), and 805 nm (1.54 eV), matching the A-exciton resonances of WS_2, MoS_2, WSe_2, and $MoSe_2$, respectively [138]. We fit the experimental data using a Lorentzian function, from which we derive linewidths of 21 nm (WS_2), 16 nm (MoS_2), 44 nm (WSe_2), and 17 nm ($MoSe_2$), which are similar to the literature reports of exciton linewidths [161].

5.3.2 Lorentz oscillator model

The exciton linewidth broadening in TMDs is widely studied and is known to be temperature dependent[52]. This temperature dependence provides a direct physical connection between the measured optical response and the presence of phonon heat in the sample. To gain a better understanding, we perform a Lorentz oscillator model simulation. This simulation helps us comprehend how heating the phonon system results in the changes in reflectivity observed around the exciton resonance.

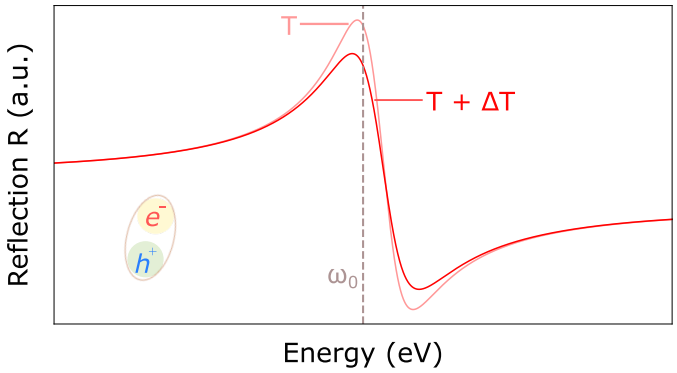


Figure 5.4: Lorentz oscillator model. Calculated reflection spectra around an exciton resonance ω_0 (dashed line) at two different temperatures. An increase in lattice temperature results in the broadening of the exciton linewidth, consequently causing a reduction in reflection around the exciton resonance energy.

Using the Lorentz oscillator model we describe the complex dielectric function $\hat{\epsilon}$ as:

$$\hat{\epsilon}(\omega) = (n_{\mathrm{b}} + ik_{\mathrm{b}})^2 + \frac{A_{\mathrm{m}}}{(\omega_0 - \omega^2 - i\gamma\omega)} \tag{5.1}$$

where ω is the energy, $n_{\mathrm{b}} + ik_{\mathrm{b}}$ represents the background complex refractive index in the absence of excitons and we assume it to be equal to that of bulk material [162]. The exciton resonance energy is denoted by ω_0 with amplitude A_{m}, and a temperature-dependent exciton linewidth broadening parameter γ. From the complex refractive index $\hat{n} = \sqrt{\hat{\epsilon}(\omega)}$, we calculate the complex reflection coefficients $\hat{r}_{\mathrm{c}}$ as:

$$\hat{r}_{\mathrm{c}} = \frac{r_{12} + r_{23}e^{2i\beta}}{1 + r_{12}r_{23}e^{2i\beta}} \tag{5.2}$$

where $r_{12} = (n_1 - n_2)/(n_1 + n_2)$, $r_{23} = (n_2 - n_3)/(n_2 + n_3)$ and $\beta = \frac{2\pi}{\lambda} n_2 d_{\mathrm{th}}$. Here, 1 and 3 represent air, 2 represents the TMD, and d_{th} is the thickness of the TMD. Finally, the reflection R is given by,

$$R = |\hat{r}_{\mathrm{c}}|^2 \tag{5.3}$$

Such reflection profiles for two different linewidths (and therefore temperatures) are shown

in Figure 5.4. As the lattice temperature rises, the exciton linewidth broadens, resulting in a reduction in reflection (at ω_0), consistent with our experimental observations. We will now quantify the typical increase in lattice temperature in TMDs using this model.

5.3.3 Estimation of temperature rise

To determine the lattice temperature rise, we plot the reflection profiles from the Lorentz oscillator model for different exciton linewidths (and therefore temperatures). For this calculation, we took the linewidth γ at room temperature (38.5 meV for $MoSe_2$ and 22.5 meV for WS_2) from the literature [52]. The transient reflectivity is determined using $\frac{\Delta R}{R} = \frac{R_{(\mathrm{T})} - R_{(\mathrm{T=300\ K})}}{R_{(\mathrm{T=300\ K})}}$, where $R_{(\mathrm{T=300\ K})}$ is the reflection at room temperature. Upon comparing our calculations with the experimental observations, we find that the temperature increase of the lattice remains below 10 K even for the highest fluence that we use. Additionally, our measurements are sensitive enough to detect heating at the single Kelvin level (see Figure 5.5a).

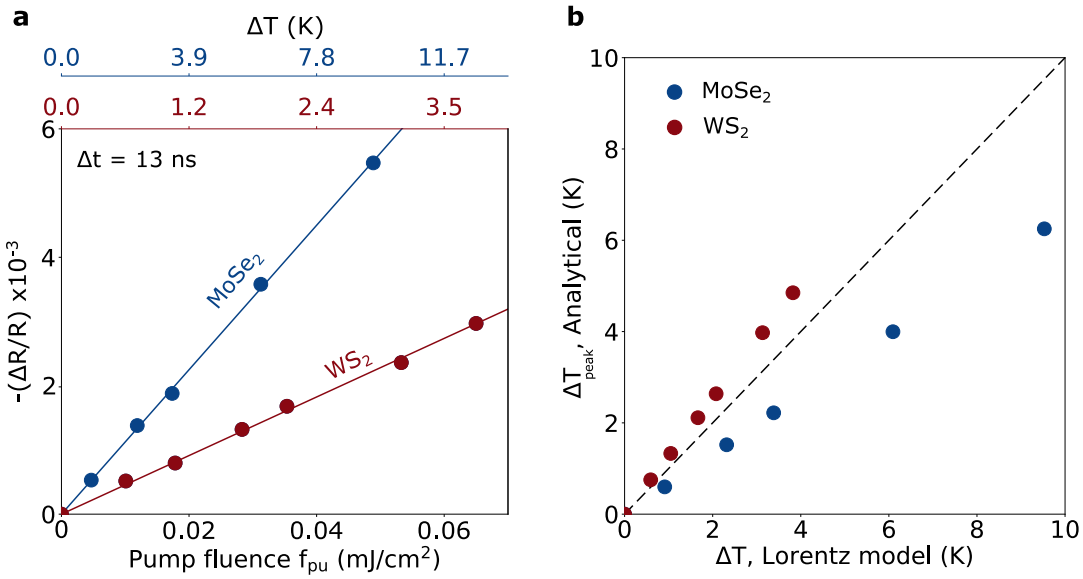


Figure 5.5: Determination of the lattice temperature increase. (a) Correlating the transient reflectivity signal with pump fluence (bottom-axis) at Δt of 13 ns to the calculated lattice temperature increase (top-axes) determined from our Lorentz oscillator model for $MoSe_2$ and WS_2. Solid lines are linear fits to the datasets. The error bars are smaller than the marker size (68% confidence interval). **(b)** Comparison of ΔT from the Lorentz oscillator model to the analytical ΔT obtained using: $(A \cdot f_{\mathrm{pu}})/(d_{\mathrm{th}} \cdot C_{\mathrm{v}})$. The dashed line represents the perfect agreement between them.

We correlate this derived ΔT from the Lorentz oscillator model with the peak temperature increase, employing the relation $\Delta T_{\mathrm{peak}} = (A \cdot f_{\mathrm{pu}})/(d_{\mathrm{th}} \cdot C_{\mathrm{v}})$. Here, A represents absorption, f_{pu} is pump fluence, d_{th} signifies thickness and C_{v} denotes heat capacity. Specifically for $MoSe_2$ (WS_2), we use a thickness of 13.8 nm (17.2 nm), C_{v} from literature sources

($MoSe_2$ from Ref. [163] and WS_2 from Ref. [164]), and an absorption of 33% (24%). Figure 5.5b depicts the resulting plot of this comparison. Although our analysis doesn't match perfectly, several factors contribute to this discrepancy. Firstly, the exciton linewidth γ at room temperature used in the Lorentz model comes from literature [52] values that were calculated for monolayers, while our samples have different thicknesses. Also, the inhomogeneous linewidth broadening was assumed not to depend on temperature in their calculation. Additionally, there could be multiple uncertainties in the material parameters, such as absorption and fluence, which we use to calculate the analytical ΔT_{peak}. Importantly, these results underscore the technique's sensitivity to reflection changes induced by heating, even by less than a Kelvin. This sensitivity is evident from the agreement between two completely separate calculations: one based on the Lorentz oscillator model and the other derived from an analytical equation.

Dependence on pump fluence

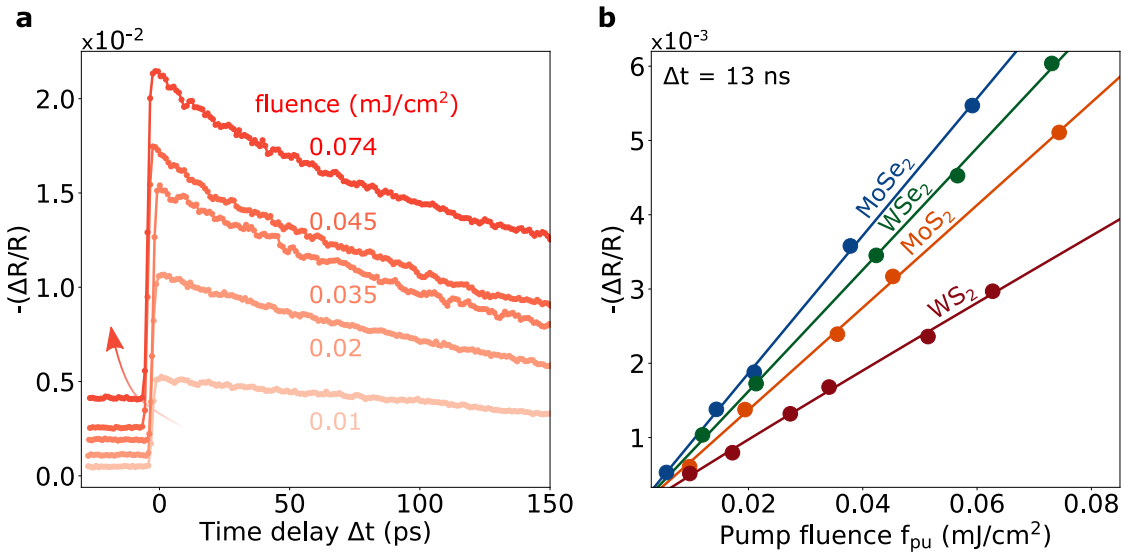


Figure 5.6: Pump fluence dependence of decay dynamics. (a) Exemplary fluence-dependent decay dynamics in suspended MoS_2. **(b)** Analysis of the transient reflectivity signal at Δt of 13 ns for all the samples studied. The error bars are smaller than the marker size (68% confidence interval). Solid lines are power-law fits, yielding the exponent of the fit to be 0.98 ($MoSe_2$), 1.00 (WSe_2), 1.00 (MoS_2), and 0.97 (WS_2), suggesting that the relationship is very close to linear.

To test our understanding of the Lorentzian model, we further investigate linewidth broadening and decreased reflection with temperature by analyzing the transient reflectivity signal as a function of pump fluence f_{pu}. We did such measurements on all the samples, and the results obtained on the suspended MoS_2 sample are shown in Figure 5.6a. Firstly, we observe that the $\Delta R/R$ signal increases with pump fluence as expected. We also

notice that the signal scales linearly with fluence, see Figure 5.6b. Crucially, this validates the utilization of the transient reflectivity profile as an accurate representation of the temperature profile, from which we will quantify the thermal diffusivity of the sample.

5.4 Spatiotemporal mapping at Δt = 0 and Δt = 13 ns

Now that we have confirmed the sensitivity of our probe to phonon heat through the analysis of the exciton linewidths, we proceed to conduct spatiotemporal imaging to visualize the diffusion process. In Figure 5.7, we present exemplary transient reflectivity

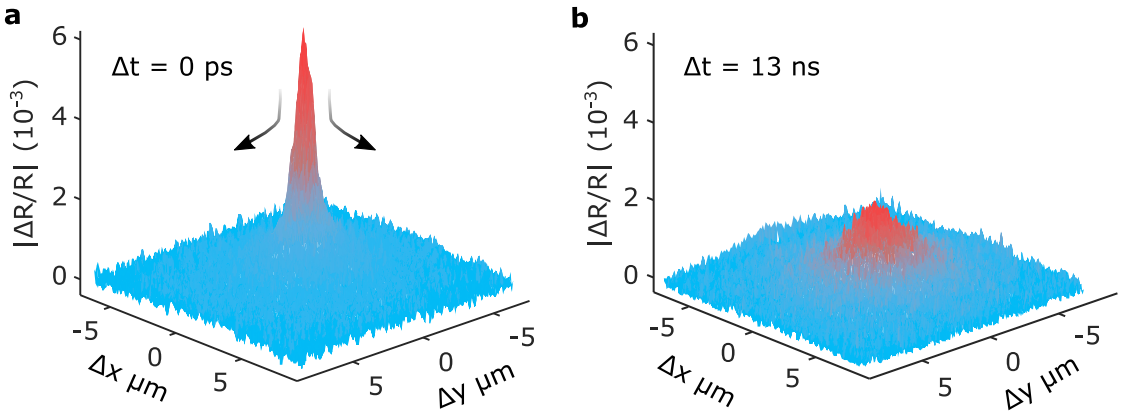


Figure 5.7: Transient reflectivity maps. (a) The $\Delta R/R$ profile at a time delay $\Delta t = 0$ ps shows a narrow profile corresponding to the electronic response created by the photoexcitation from the pump pulse. **(b)** The profile measured at $\Delta t = 13$ ns shows a broadened response due to the diffusion of phonon heat.

maps captured at two distinct pump-probe time delays on the $MoSe_2$ sample. At time-zero ($\Delta t = 0$ ps), a narrow profile centered at the pump spot is evident, attributed to the electronic excitation induced by the absorption of the pump pulse.

Upon tuning to a slightly negative time delay (effectively, Δt of 13 ns), we observe a broader profile with reduced amplitude. As discussed earlier, this signal is the result of the diffusion of phonon heat within the sample. Importantly, the broader the 13 ns profile, the greater the expected diffusivity of the phonon heat, ultimately enabling us to quantitatively determine the diffusivity.

Figure 5.8 depicts the line-cuts of the transient reflectivity maps at $\Delta t = 0$ ps and $\Delta t = 13$ ns. The profiles are clearly non-Gaussian, which indicates that the observations cannot be solely attributed to the diffusion of a single Gaussian hot spot (as discussed in Section 2.2). This deviation from Gaussian behaviour implies the involvement of additional underlying processes. To accurately interpret these results and determine the diffusivity, it is essential to have a thorough understanding of the measurement technique employed.

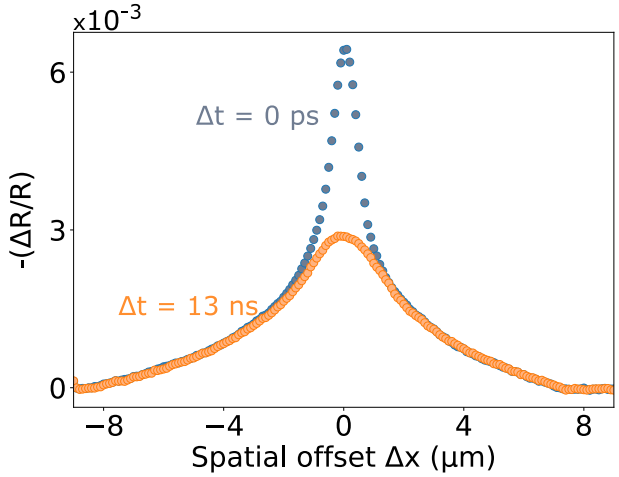


Figure 5.8: Line-cuts of a transient reflectivity map. The transient reflectivity $\Delta R/R$ profiles at a time delay $\Delta t = 0$ ps and $\Delta t = 13$ ns from a 2D map, demonstrating that the profiles are not Gaussian.

5.5 Heat accumulation: Schematics

Figure 5.9a illustrates the temporal evolution of the temperature increase ΔT in the suspended region of the sample across one on-off cycle of the pump. During the pump-on window, a train of pulses (at every 13 ns) photoexcites the sample, where each pump pulse leads to localized heating. Due to insufficient time for the system to return to equilibrium between successive pump pulses, heat steadily accumulates within the system. This accumulation persists over $N_\mathrm{p} = f_\mathrm{rep}/2f_\mathrm{mod}$ pump pulses (with a 50% duty cycle modulation), resulting in a progressive rise in system temperature, peaking towards the end of the pump-on window. Subsequently, as the pump pulses are blocked (pump-off window), the accumulated heat dissipates, and the system achieves thermal equilibrium prior to the next cycle involving N_p pump pulses.

The progression of the temperature profiles is depicted in Figure 5.9b. Following the initial pump pulse, photoexcitation at pump-probe delay time $\Delta t = 0$ exhibits a narrow Gaussian profile (i). After pump excitation and electron-phonon coupling, heat begins to diffuse within the phonon system. Consequently, at a slightly negative Δt (or $\Delta t \approx$13 ns), just before the second pump pulse, the Gaussian profile has decayed and broadened (profile (ii)). The arrival of the second pump pulse (at 13 ns) introduces another narrow Gaussian profile on top of the diffused Gaussian profile (iii). This composite profile subsequently diffuses, resulting in a sum of two broadened Gaussians (profile (iv)). This sequence continues for N_p pump pulses (at every 13 ns), culminating in profile (v) immediately after the final pump pulse. The cumulative photoexcitation following N_p pulses eventually yields a spatial profile similar to (vi). This profile comprises a narrow component representing

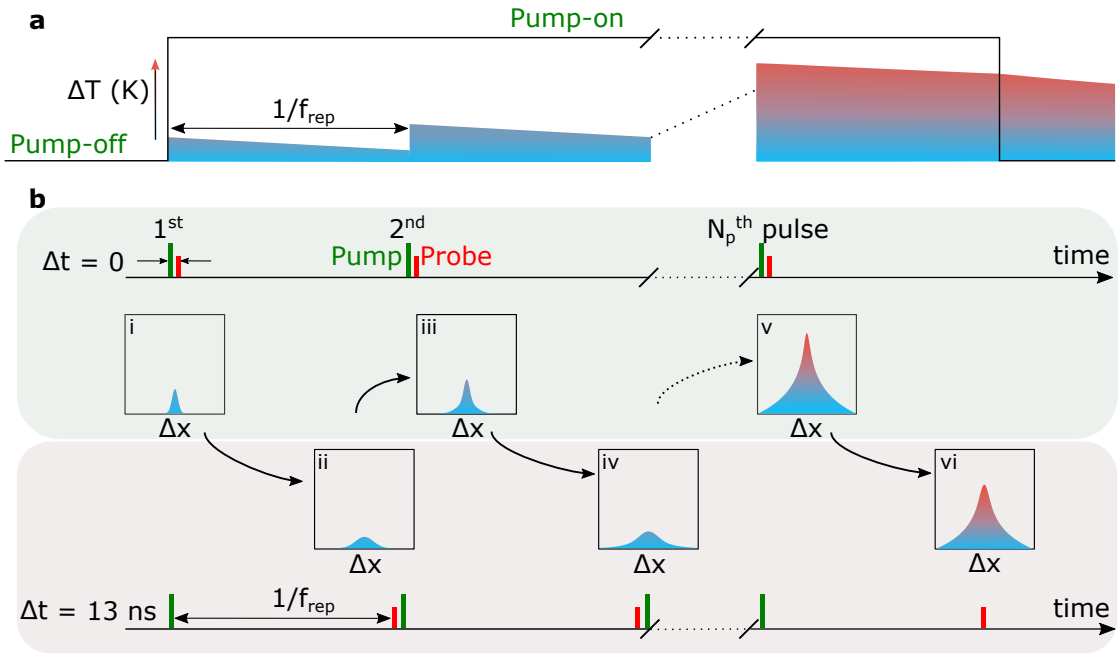


Figure 5.9: Illustration of heat accumulation. (a) Schematic representing the temperature rise in the suspended region of the sample during one pump-on window. **(b)** Evolution of the initial Gaussian profile (i) over a single pump-on window containing N_p pulses. The top shaded region represents the situation at $\Delta t = 0$, and the bottom illustrates the diffused heat profiles at $\Delta t = 13$ ns. By using a negative pump-probe delay time (equivalent to $\Delta t = 13$ ns), the N_p^{th} probe pulse senses the effect of the $(N_p - 1)^{th}$ pump pulse and possibly the cumulative effect of all until $N_p - 1$ pulses.

diffused heat from the preceding pump pulse and a broader component corresponding to accumulated heat from all prior pump pulses.

5.6 Simulations: Solving Fourier's heat law

To understand the spatial profile's shape and to obtain the accurate thermal diffusivity, we conduct a straightforward simulation based on Fourier's law of heat conduction in 2-dimension:

$$\frac{\partial T}{\partial t} = D\left(\frac{\partial^2 T}{\partial x^2} + \frac{\partial^2 T}{\partial y^2}\right) + \sum_i S_i \tag{5.4}$$

We model two-dimensional diffusion with radial symmetry, computing the temperature increase, $\Delta T(x, y)$. We apply a perfect heat sink as the boundary condition at the periphery of the circular sample with a radius r_d. This means at position $r = \sqrt{x^2 + y^2}$, $\Delta T_{r=r_d} = 0$ K.

In the simulation, we introduce a Gaussian source to evolve in both space and time, with a constant diffusion coefficient. At $t = 1/f_{rep}$, we introduce an additional pump pulse

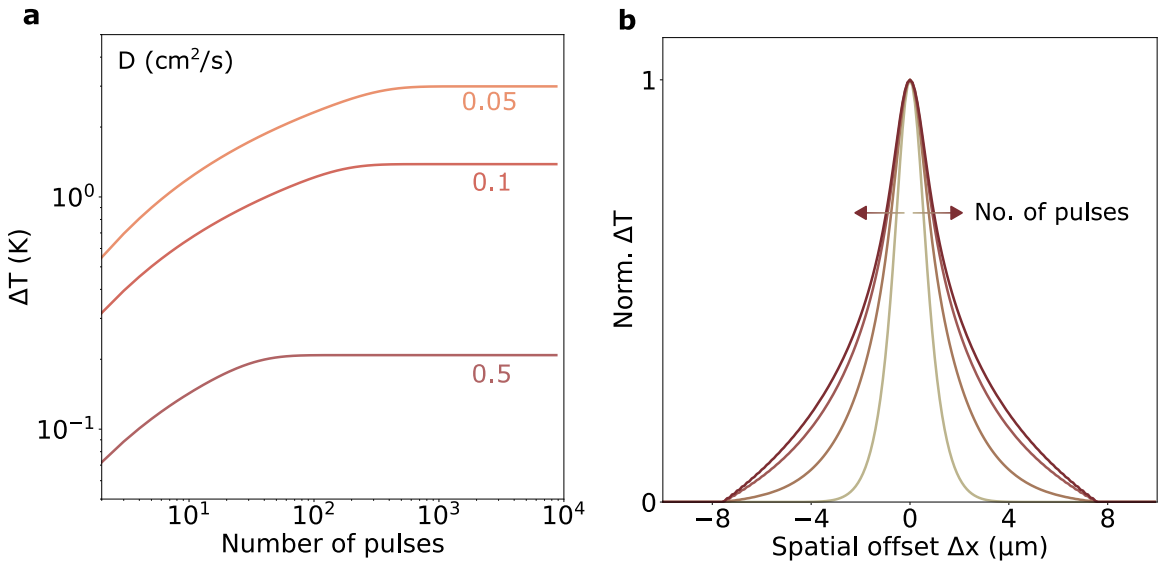


Figure 5.10: Simulation: Effect of number of pulses. (a) Calculated temperature rise with increasing number of pulses N_p for different input thermal diffusivities D. **(b)** Broadening of the spatial profiles for a fixed thermal diffusivity with N_p.

to the residual heat profile. We repeat this process for all N_p pulses and obtain the final temperature profile. With increasing N_p, we observe the peak temperature's saturation at $(\Delta x,\ \Delta y) = 0$, indicating the establishment of a steady-state profile, as plotted in Figure 5.10a. The simulations reveal that a higher thermal diffusivity reduces the number of pulses required to reach a steady-state condition, consequently leading to a lower peak temperature. This is because, in such scenarios, heat diffuses more rapidly towards the heat sink.

When we visualize these simulated spatial profiles for a constant thermal diffusivity, we notice a gradual broadening of the profile with each increment in the number of pulses (see Figure 5.10b), an observation in line with our previous discussions. Experimentally, adjusting the number of pulses entails changing the pump modulation frequency (f_{mod}). As we proceed, we will demonstrate the excellent agreement between experimental findings and simulations across a wide range of modulation frequencies.

We additionally demonstrate the variations in the spatial profile for different diffusivities. This aspect is significant as it underscores the sensitivity of our technique in determining a sample's diffusivity. To explore this, we conduct simulations using different diffusion coefficients. Figure 5.11 shows the resulting average spatial profile after N_p pulses. Our simulations confirm that broader spatial profiles correspond to larger D values, consistent with our initial intuitive reasoning. Moreover, we observe that our technique can effectively capture diffusivities spanning several orders of magnitude. For accessing the Python script that we use to solve the heat diffusion equation, see Appendix Section A1.

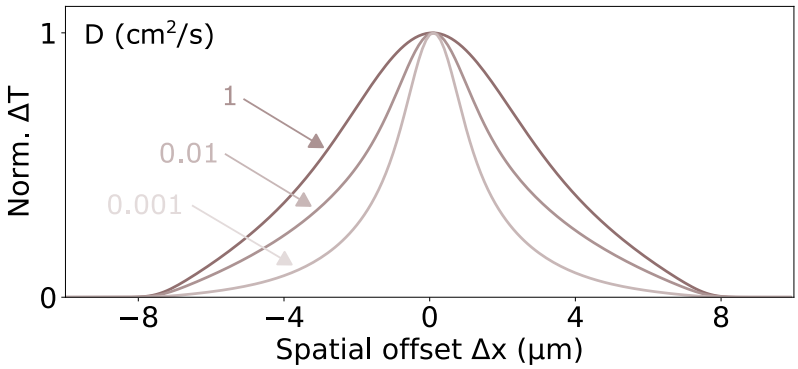


Figure 5.11: Simulation: Effect of thermal diffusivity. Average spatial heat profiles after N_p pulses (normalized) are depicted for various D values. The profiles are broader for higher diffusivities.

5.7 Experimental results and comparison: Bulk TMDs

Now we proceed to conduct spatiotemporal measurements on four suspended TMDs to quantify their thermal diffusivities. We pump at the center of the suspended region and record the $\Delta R/R$ profiles across the suspended region at $\Delta t = 0$ and $\Delta t = 13$ ns. To extract the width of the $\Delta t = 0$ spatial profile, we subtract the background signal, i.e. $\Delta t = 13$ ns profile, and fit a Gaussian to it. Figure 5.12a-d display these normalized spatial profiles at $\Delta t = 0$ and $\Delta t = 13$ ns for (a) $MoSe_2$, (b) WSe_2, (c) MoS_2, and (d) WS_2, measured with a pump fluence of approximately 0.03 mJ/cm^2 at $f_{\text{mod}} = 4.37$ kHz. We determine the diffusivity by minimizing the squared residuals between the experimental $\Delta t = 13$ ns profile and the simulated profile. This process requires knowledge of just the diameter of the suspended flake (15 μm) and the experimental beam width of the pump and the probe. We determine the experimental beam size from the Gaussian fit to the $\Delta t = 0$ profile and knife edge measurements (see Figure 4.4e), by assuming the ratio between experimental beam widths and knife-edge measurements is identical (see Appendix Section A2). To match with experimental conditions, we convolve the simulated profiles with the probe beam's spatial profile. Through this method, we obtain thermal diffusivities D of 0.18 ± 0.02 cm^2/s for $MoSe_2$, 0.20 ± 0.03 cm^2/s for WSe_2, 0.35 ± 0.04 cm^2/s for MoS_2, and 0.59 ± 0.07 cm^2/s for WS_2.

To verify the obtained diffusivity values for these TMD films, we initiate a comparison with experimental data available in the literature. Many studies present thermal conductivity κ, which correlates with diffusivity through the heat capacity: $\kappa = D \cdot C_v$. Thus, we convert our diffusivity values utilizing the bulk heat capacities from literature references for $MoSe_2$: 1.87×10^6 J/m^3/K [163], WSe_2: 1.98×10^6 J/m^3/K [163], MoS_2: 2.01×10^6 J/m^3/K [171], and WS_2: 1.93×10^6 J/m^3/K [164].

Figure 5.12e illustrates the comparison between our experimental results (solid lines)

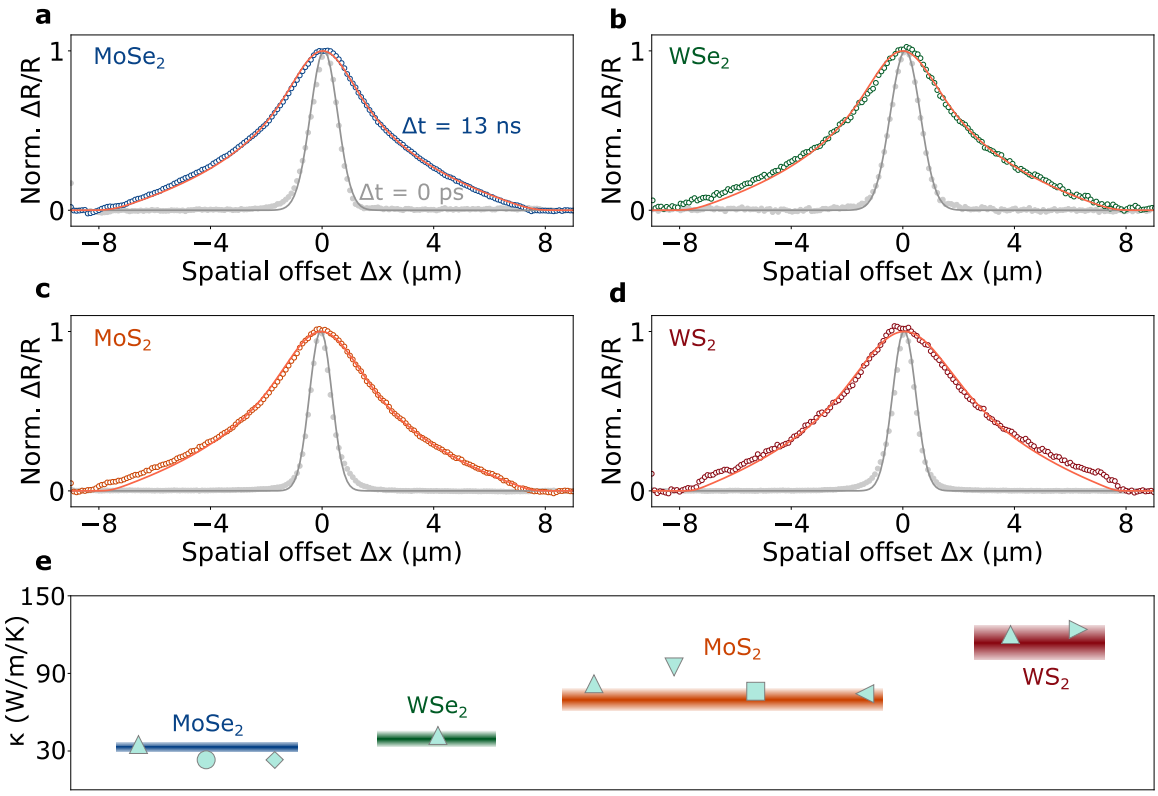


Figure 5.12: Thermal diffusivities and benchmarking. (a-d) Measured transient reflectivity profiles, all normalized to the peak of the fit, for $MoSe_2$, WSe_2, MoS_2, and WS_2. The narrow profiles are described using a single Gaussian function (grey line) to obtain their width. We describe the $\Delta t = 13$ ns profile using our Fourier model (light red line) based on heat diffusion to quantify the thermal diffusivity of 0.18 ± 0.02 cm^2/s for $MoSe_2$, 0.20 ± 0.03 cm^2/s for WSe_2, 0.35 ± 0.04 cm^2/s for MoS_2, and 0.59 ± 0.07 cm^2/s for WS_2. **(e)** Comparison of the calculated thermal conductivity from the measured thermal diffusivity with literature; △ (Ref. [165]), ○ (Ref. [74]), ◇ (Ref. [166]), ▽ (Ref. [167]), □ (Ref. [168]), ◁ (Ref. [169]), and ▷ (Ref. [170]). The solid line represents the extracted κ values for the TMDs, each approximately 15 nm thick, while the gradient limit indicates the error margin with a 95% confidence interval.

and other experimental findings (symbols). For consistency, we focus our comparison on literature values pertaining to relatively thick crystals, about 10 nm and above. The comparison reveals a notable agreement between our findings and the literature, thereby confirming the prevailing trend wherein selenides ($MoSe_2$, WSe_2) exhibit lower thermal conductivity compared to sulfides (MoS_2, WS_2) [172].

In the case of bulk $MoSe_2$ and WSe_2, prior experimental investigations have quantified thermal conductivities ranging from 22 to 42 W/m/K [74, 165, 166] which is in good agreement with our derived κ values of 33.5 W/m/K for $MoSe_2$ and 39.6 W/m/K for WSe_2. For WS_2, our findings yield a relatively high κ value of 113.9 W/m/K, which correlates well with existing experimental data [165, 170]. Similarly, our determined κ value for MoS_2, at 70 W/m/K, is consistent with reports in Refs. [165, 168, 169]. However, we note a considerable dis-

crepancy compared to the thermal conductivity measured in Ref. [167]. This divergence is likely attributed to the smaller thickness of our sample relative to what was examined in that work.

As another proof-of-concept experiment, we measure the $MoSe_2$ sample using different laser repetition rates, with our second spatiotemporal setup, which uses a SuperK laser (FIU-6, NKT Photonics). We conduct measurements at three different laser repetition rates — 78 MHz, 39 MHz, and 26 MHz — corresponding to maximum time delays of 13 ns, 26 ns, and 38 ns, respectively. Intuitively, the larger the time delay, the more time for heat to spread, which will result in lower signal amplitude and a broader profile compared to shorter time delays. Indeed, we observe this behaviour in our results: the transient reflectivity signal decreases with decreasing repetition rate (see Figure 5.13a), and the spatial profiles become broader at lower repetition rates (see Figure 5.13b). By describing the spatial profiles using the Fourier model based on heat diffusion, we obtain a thermal diffusivity of 0.18 ± 0.01 cm^2/s for the 78 MHz ($\Delta t = 13$ ns) measurements, consistent with the above results. For repetition rates of 39 MHz ($\Delta t = 26$ ns) and 26 MHz ($\Delta t = 38$ ns), we find lower diffusivity values of 0.13 ± 0.01 cm^2/s.

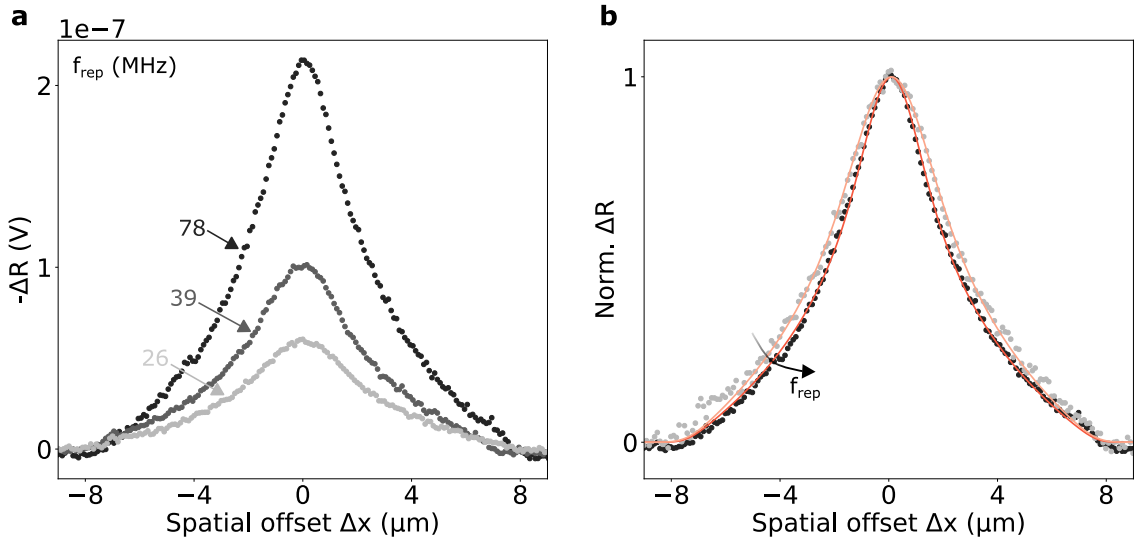


Figure 5.13: Laser repetition rate dependence of spatial profiles in $MoSe_2$. **(a)** Spatial profiles obtained on $MoSe_2$ at different repetition rates of the laser. **(b)** The experimental profile (normalized to the peak of the fit) at 78 MHz and 26 MHz described using our Fourier model based on heat diffusion (light red line), yielding a D of 0.18 ± 0.01 cm^2/s and 0.13 ± 0.01 cm^2/s, respectively.

Although our preliminary measurements show qualitative and some quantitative consistency, we have yet to fully explain the observed reduction in thermal diffusivity. To address this, we plan to repeat these measurements systematically and also in other 2D materials as part of our research focus in the coming years.

5.8 Modulation dependent spatial profiles

As a final experiment, to understand the working principle of our technique, we perform heat diffusion measurements on a suspended $MoSe_2$ sample, while varying the modulation frequency f_{mod}, thus controlling the number of pulses in the pump-on window. As indicated by our simulations (see Figure 5.10), an increased number of pulses leads to a broader spatial heat profile, a trend also observed in our experimental results. Figure 5.14 shows spatial profiles at different modulation frequencies ranging from 240 kHz to 4 kHz. We note a distinct broadening of the $\Delta t = 13$ ns spatial profiles as f_{mod} decreases, with a tendency to reach saturation at the lowest modulation frequencies (see Figure 5.14).

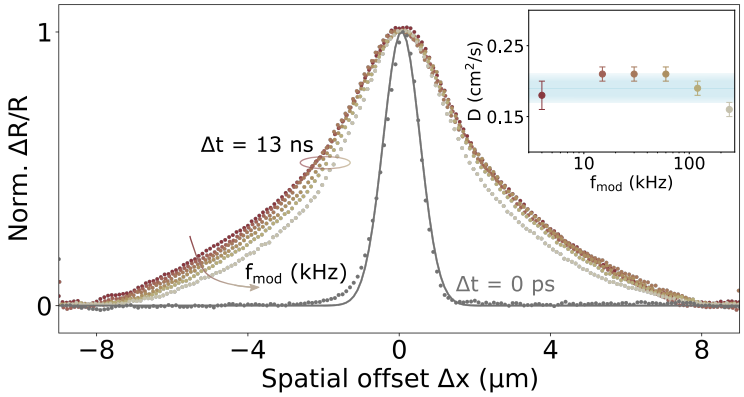


Figure 5.14: Modulation frequency dependence of spatial profiles in $MoSe_2$. For low modulation frequencies ($4 - 30$ kHz), the spatial profiles are similar, indicating temperature saturation due to steady state formation. The narrow profile represents the $\Delta t = 0$ profile (grey scatters) for f_{mod} at 240 kHz and is described by a Gaussian function. The inset shows the thermal diffusivities obtained at different f_{mod}. The shaded region represents the average D with the gradient limit being the standard deviation.

This saturation phenomenon is attributed to the establishment of a steady-state profile, where the rate of heat addition from absorbed light equals the rate of heat diffusion to the edge of the suspended material and subsequent dissipation into the gold-coated substrate. Lower modulation frequencies, corresponding to extended excitation periods with pump pulses, result in increased accumulated heat, thus broadening the profile further. We analyse the $\Delta t = 13$ ns profiles and describe them with our Fourier model based on heat diffusion. We observe that the thermal diffusivities remain similar across the modulation frequency range, 0.18 ± 0.01 cm^2/s (4 kHz), 0.21 ± 0.01 cm^2/s (15 kHz), 0.21 ± 0.01 cm^2/s (30 kHz), 0.21 ± 0.01 cm^2/s (60 kHz), 0.19 ± 0.01 cm^2/s (120 kHz), and 0.16 ± 0.02 cm^2/s (240 kHz). We calculate the average diffusivity to be 0.19 ± 0.02 cm^2/s (see the inset of Figure 5.14).

5.9 Describing in-phase and quadrature lock-in signals

The experimental spatial profiles we have shown until now correspond to the total amplitude signals obtained from the lock-in amplifier. However, in order to obtain an even more accurate extraction of the diffusivity, we consider both the in-phase (denoted as X) and out-of-phase (denoted as Y) signals.

A lock-in amplifier multiplies the signal response from the sample with a reference signal and a 90-degree phase-shifted signal having a frequency f_{mod}, and filters out the signal at that same frequency. This filtering process can be understood as the averaging of the signal over the entire experiment duration. Filtering (or averaging) these two resulting signals (low-pass filtering), results in the in-phase and the out-of-phase components. Filtering allows the removal of the noise at other frequencies. The total amplitude of the signal (or the R channel) is then given by $R_{\mathrm{ta}} = \sqrt{X^2 + Y^2}$.

To understand the in-phase and out-of-phase signals for different modulation frequencies, we adapt our Fourier model by including the lock-in operation. Here, we show the results at two different modulation frequencies: 10 kHz and 240 kHz. Figure 5.15a shows the temperature dynamics for $f_{\mathrm{mod}} = 10$ kHz at the hotspot ($\Delta x = \Delta y = 0$) obtained from the Fourier model (see Section 5.6) over a few modulation cycles. As clearly seen, the temperature rises and reaches saturation during the pump-on window, and decays to zero in approximately 2 µs during the pump-off window. The extended pump-off period (tens of microseconds) allows the temperature to return fully to equilibrium.

To perform the lock-in operation, we multiply these temperature dynamics with sine (for the in-phase signal, see Figure 5.15b) and cosine (for the out-of-phase signal, see Figure 5.15c) functions with a frequency equivalent to the modulation frequency ($f_{\mathrm{mod}} = 10$ kHz). Upon averaging these signals over time, the temperature dynamics multiplied by the cosine function average out to nearly zero, whereas the dynamics multiplied by the sine function do not. Consequently, there will be a predominant in-phase component while the out-of-phase signal will be negligible.

We repeat this lock-in operation to the temperature dynamics at various positions (from hotspot to heat sink) to reconstruct the in-phase and out-of-phase spatial profiles. Figure 5.15d presents the resulting in-phase and out-of-phase spatial profiles. The resulting total amplitude (R channel) of the lock-in is almost entirely due to the contribution of the in-phase signal.

Figure 5.15e-h shows similar simulation results for a modulation frequency of 240 kHz. Unlike the 10 kHz case, the temperature dynamics exhibit a finite signal during the pump-off window, as seen in Figure 5.15e. This key difference leads to a finite amount of out-of-phase signal when averaging the cosine multiplied temperature dynamics. However,

the in-phase signal's amplitude remains larger because the temperature dynamics have

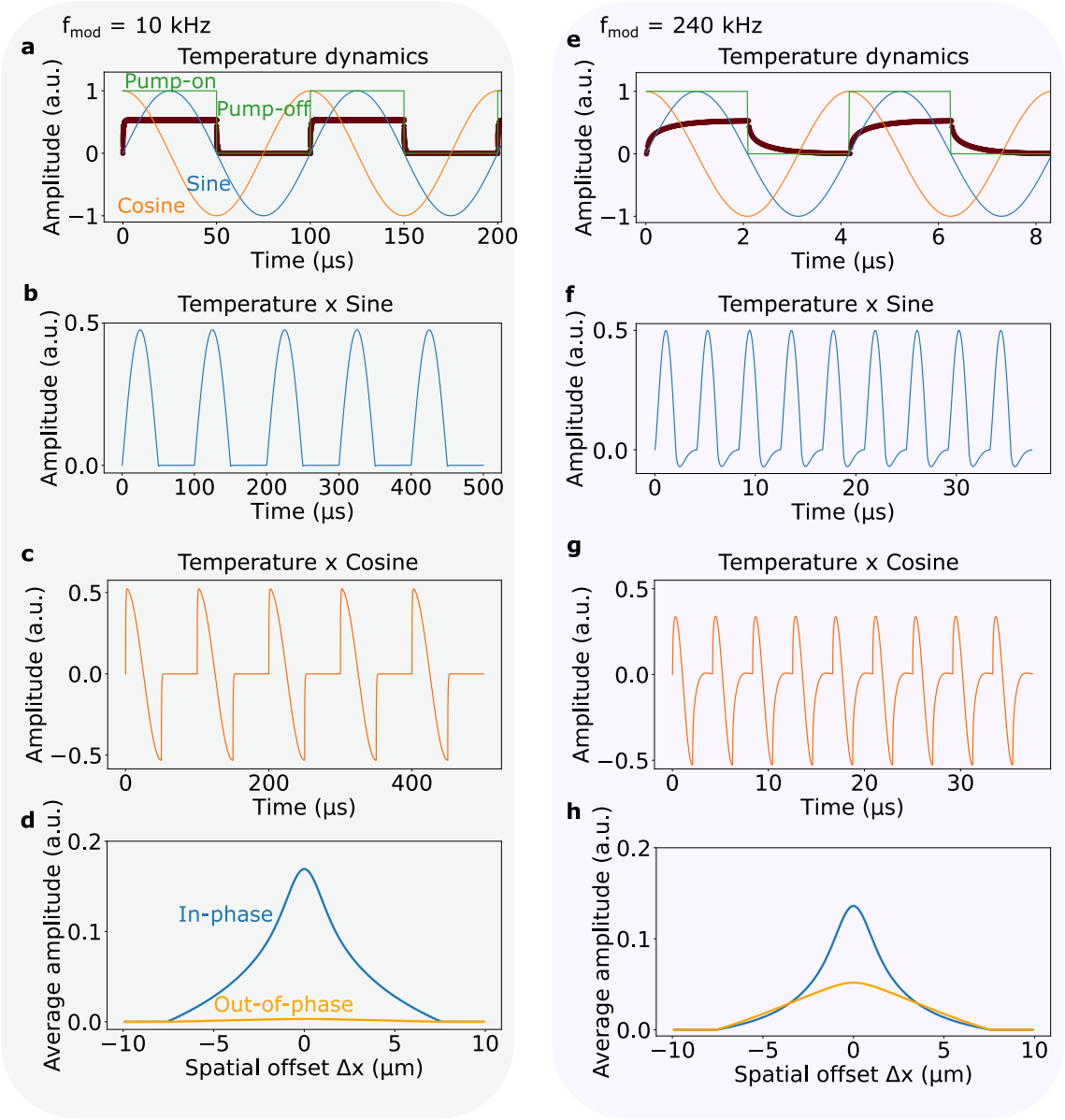


Figure 5.15: Simulations of lock-in operation. **(a)** Simulated temperature dynamics (at the hotspot, $\Delta x = \Delta y = 0\mu$m) at every $\Delta t = 13$ ns (brown scatters) during multiple square wave modulation ($f_{\text{mod}} = 10$ kHz) cycles, along with the reference signals at the same f_{mod}. **(b, c)** The temperature dynamics multiplied with (b) sine and (c) cosine functions. **(d)** The in-phase and out-of-phase profiles after averaging the sine and cosine multiplied temperature dynamics at different positions. For large pump-off time (small f_{mod}), the out-of-phase component averages out to be zero. **(e-h)** The same simulation performed at a modulation frequency of 240 kHz. The out-of-phase signal is multiplied by -1 for a proper comparison. The diffusivity in both cases is set at 0.20 cm^2/s.

a higher amplitude during the pump-on window. Figure 5.15h shows the full spatial profile of the in-phase and out-of-phase signals, illustrating the results of multiplying the temperature dynamics from various positions (from hotspot to heat sink). In conclusion,

if there is a significant amount of time in the pump-off state where the response from the sample is zero, the dominant signal will be the in-phase signal, while the out-of-phase signal will approach zero.

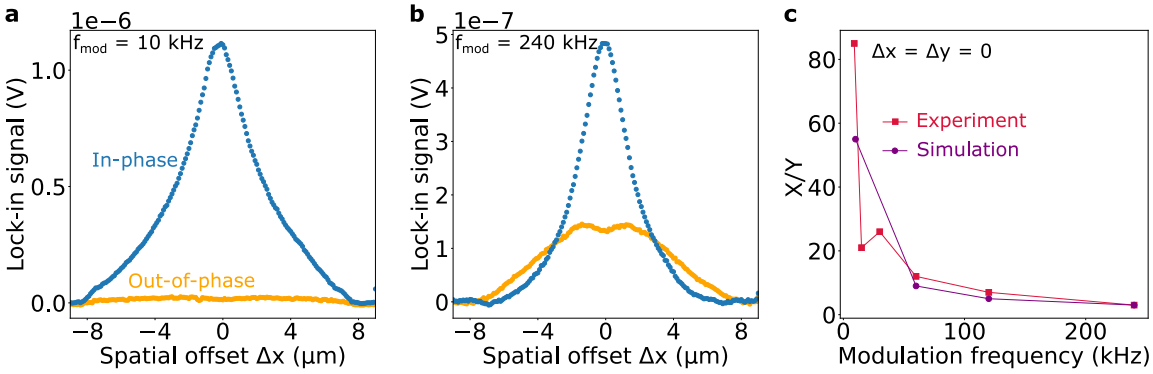


Figure 5.16: Experimental profiles and the ratio of in-phase to out-of-phase. (a, b) In-phase and out-of-phase experimental profiles for a 20-layer $MoSe_2$ at (a) f_{mod} = 10 kHz and (b) f_{mod} = 240 kHz. **(c)** Ratio of in-phase to out-of-phase (X/Y) at the hotspot from the experiment and simulation (D = 0.20 cm^2/s).

To assess the validity of our simulations, we compare them with experimental results shown in Figure 5.16, which show the in-phase and out-of-phase spatial profiles for a 20-layer $MoSe_2$ flake (decomposed profiles from Figure 5.14). At a modulation frequency of 10 kHz (see Figure 5.16a), the in-phase signal is prominent while the out-of-phase signal is negligible, consistent with our simulation results. Conversely, at 240 kHz (see Figure 5.16b), we observe a significant amount of out-of-phase signal alongside a predominant in-phase signal. We further compare the in-phase to out-of-phase ratio at the hotspot ($\Delta x = \Delta y = 0$) between simulation and experiment across different modulation frequencies. Both sets of data are in qualitative agreement, showing an increasing in-phase to out-of-phase ratio with decreasing modulation frequency (see Figure 5.16c).

5.10 Evaluation of spatiotemporal thermometry

Our investigation into the spatiotemporal technique that we developed has unveiled its capability to determine the thermal diffusivities of thin films. We conclude this chapter by discussing the principal advantages of this methodology. Unlike electrical methods [156], it presents a distinct advantage by being a contact-free and non-invasive technique. Moreover, in contrast to various all-optical approaches such as TDTR [40], FDTR [41], Raman thermometry-based techniques [173], and TTG [43], it offers several notable benefits. A key strength lies in its capability to quantify the in-plane thermal diffusivity of a thin film through comparison with a simple description grounded on Fourier's heat law. Unlike these techniques, spatiotemporal pump-probe thermometry does not need material parameters

like temperature coefficient, optical absorption, thickness, interfacial thermal conductance, heat capacity, and properties associated with transducer layers to quantify the thermal properties. For simulations, we only need specific experimental conditions, namely the diameter of the suspended material region, the beam sizes, and the laser's repetition rate. As these parameters are known with a high degree of precision, typically within an error margin of a few percent or less, we obtain accurate diffusivity determinations. Consequently, our proposed method eradicates error sources arising from the necessity of measuring intermediate parameters utilized in the model for extracting unknown thermal properties. In this regard, we would like to note that, recently, Xu et al. [174] developed a beam-offset FDTR method to measure the in-plane thermal diffusivity by analyzing the slope of the phase lag versus offset plot for various excitation frequencies, without requiring any material input parameters.

Another significant benefit lies in the sensitivity of the method. The capability to detect changes in a spatial temperature profile is only constrained by the signal-to-noise ratio, ultimately dictating the accuracy in quantifying the diffusivity. Being a pump-probe technique, where the pump-induced changes are detected differentially using the combination of an optical chopper and a synchronized lock-in amplifier, means that we can resolve very subtle heat-induced changes in the refractive index (permittivity) of materials. Consequently, it is possible to quantify thermal transport properties even if the change in temperature due to heating is very small, on the single Kelvin level (see Figure 5.5). This represents a significant advantage over alternative techniques that typically require stronger heating.

In addition to these benefits, our technique holds promise in investigating previously unexplored physical phenomena and properties. Taking thermal transport as a primary example, we propose integrating our technique that quantifies thermal diffusivity with a complementary study offering thermal conductivity, thus facilitating the optical determination of heat capacity. Moreover, our technique is poised to facilitate exploration into transport regimes beyond diffusive transport, encompassing ballistic or hydrodynamic phonon transport. This has predominantly been explored theoretically in two-dimensional materials [68, 105], yet lacks substantial experimental validation [93, 175]. Given its high sensitivity to diffusive processes occurring at nanometer-length scales, we anticipate that our method will advance the comprehension of non-diffusive transport in low-dimensional materials (see Chapter 7). Furthermore, we highlight that our technique facilitates the examination of complex structures, such as van der Waals heterostructures comprising various layered materials, with material specificity achieved through the identification of material-specific exciton resonances.

Lastly, we address the drawbacks of our spatiotemporal microscopy technique. In our

exploration of thermal diffusion in thin TMDs, we capitalize on increased sensitivity attributed to the temperature-dependent exciton response. It is important to note that not all materials have exciton resonances, meaning they may not all benefit from the same sensitivity enhancement. Nevertheless, the technique is anticipated to be effective for any diffusing species possessing an associated optical response and a sufficiently long lifetime for detection at several nanoseconds. In fact, we have successfully measured materials such as graphene nanoribbons [176] and MXenes using this method. Considering the prevalence of temperature-dependent refractive indices, we expect to quantify the thermal diffusivity of materials without an exciton response.
It is worth mentioning that in certain materials, such as those with prolonged photoexcited charge-carrier lifetimes, direct determination of thermal diffusivity may not be feasible. This limitation arises because the 13 ns signal may predominantly reflect electronic diffusion rather than thermal diffusion. However, this suggests that the technique allows for observing charge diffusion in semiconducting thin films with carrier lifetimes ranging from nanoseconds to microseconds. This aspect is particularly intriguing for materials characterized by low electronic diffusivities. Finally, we highlight that our 2D diffusion model assumes uniform heating along the out-of-plane direction (c-axis), justified by our flake's thicknesses below the optical penetration depth (20 nm at 515 nm for $MoSe_2$). However, if the thickness exceeds the optical penetration depth, coupled with high thermal anisotropy, the 2D model will need to be adapted into a three-dimensional problem.

5.11 Summary

In summary, we have introduced a novel approach for measuring the thermal diffusivity using spatiotemporal pump-probe microscopy. This involves analyzing the spatial temperature profile at a slight negative time delay (or $\Delta t = 13$ ns). Specifically, we have demonstrated the applicability of this technique in determining the in-plane thermal diffusivity of suspended films of four different TMDs: $MoSe_2$, WSe_2, MoS_2, and WS_2. Our method offers a straightforward, sensitive, and precise means of assessing thermal diffusivity, which will contribute to a deeper comprehension of the thermal characteristics of nanoscale materials.
Additionally, we propose that our approach holds the potential for exploring previously inaccessible insights into non-diffusive heat transport phenomena in low-dimensional materials, paving the way for new avenues of research and technological progress.

Contributions

Sebin Varghese fabricated the samples, performed the spatiotemporal measurements, and

developed the Fourier model with inputs from Dr Jake Dudley Mehew, Dr Alexander Block, and David Saleta Reig. Sebin Varghese and Afroditi Koutsogianni performed the spatiotemporal measurements with the SuperK laser system under the supervision of Prof. Klaas-Jan Tielrooij. The results were discussed and interpreted together with Dr Jake D. Mehew, Dr Alexander Block, David Saleta Reig, and Prof. Klaas-Jan Tielrooij.

6

Raman thermometry: Steady-state heat transport down to monolayer

"In nature, the smallest thing is as complex as the largest." - Unknown

In this chapter, we present a systematic investigation of the in-plane thermal conductivity (κ) of $MoSe_2$ (suspended over 15 µm) as a function of flake thickness, extending to the monolayer limit, using Raman thermometry. Our experimental findings reveal that the thermal conductivity of $MoSe_2$ exhibits minimal variation, changing by less than a factor of two, across the range from 50 nm to monolayer flakes. *Ab initio* simulations point to strongly changing phonon contributions to κ when the thickness decreases from bulk to monolayer. This is marked by the emergence of heat-carrying phonon modes around ≈0.1 THz. Such low-frequency modes, compensate for the expected reduction of κ towards the monolayer, thus resulting in an overall weak effect when changing the material thickness.

This chapter is based on the following publication:
D. Saleta Reig, **S. Varghese**, R. Farris, A. Block, J. D. Mehew, O. Hellman, P. Woźniak, M. Sledzinska, A. El Sachat, E. Chávez-Ángel, S. O. Valenzuela, N. F. van Hulst, P. Ordejón, Z. Zanolli, C. M. S. Torres, M. J. Verstraete, and K. J. Tielrooij, Unraveling heat transport and dissipation in suspended $MoSe_2$ from bulk to monolayer, Advanced Materials 34, 2108352 (2022) [74].

6.1 Introduction

Before exploring the thickness-dependent thermal properties using spatiotemporal thermometry, we initially utilize a well-established steady-state optothermal technique: Raman thermometry. We have two main reasons for conducting these measurements.
One reason is the absence of a systematic study examining how the thickness of $MoSe_2$ affects its thermal conductivity in the in-plane direction down to the monolayer limit. Notably, the experimental values for the in-plane lattice thermal conductivity of TMDs exhibit considerable variability, particularly in $MoSe_2$, where reported values range from 6 to 59 W/m/K [140, 166]. The exact relationship between thermal conductivity and the thickness of TMD flakes is not well understood, and a comprehensive experimental study covering a broad range of thicknesses has been lacking [177–180]. Additionally, the calculated thermal conductivity from atomistic simulations ranges between 17 to 54 W/m/K [180, 181] for $MoSe_2$ monolayer systems.
Another reason is that Raman thermometry provides insights into the thermal conductivity of $MoSe_2$, offering a comparison for subsequent analyses using spatiotemporal thermometry which yields the thermal diffusivity. By comparing these results, we can gain a complete understanding of the heat transport properties of $MoSe_2$. The advantage of employing Raman thermometry also stems from its compatibility with the suspended samples used in spatiotemporal thermometry experiments.
Addressing the influence of sample thickness on the thermal conductivity of $MoSe_2$ and explaining the underlying physical mechanisms are key objectives of this chapter. By systematically exploring $MoSe_2$ across various thicknesses, we aim to clarify how thermal conductivity depends on the sample thickness. In the following sections, we describe our use of Raman thermometry to investigate these thickness-dependent variations in thermal conductivity. Our experimental observations and theoretical insights offer a deeper understanding of heat transport properties in $MoSe_2$, extending down to the monolayer limit.

6.2 Raman thermometry

One of the most common techniques used to study the heat transport properties of thin films is Raman thermometry [36, 37]. This method utilizes the principles of Raman scattering, in which photons from a laser source are inelastically scattered by a material, resulting in a shift in the energy of the scattered light. This shift, known as the Raman shift, occurs because the incident photons either gain or lose energy by interacting with the vibrational modes of a material. The Raman shift is typically linked to a material's

temperature (see Figure 6.1a). Understanding the Raman shift provides us with the means to access the thermal conductivity of a material. In our study, we utilize single-laser Raman thermometry, wherein a laser beam functions as both a heat source and a thermometer. The thermometer operates via Raman scattering of the laser light, where the temperature-dependent frequency shift of a Raman mode provides a method to determine the local temperature of a material.

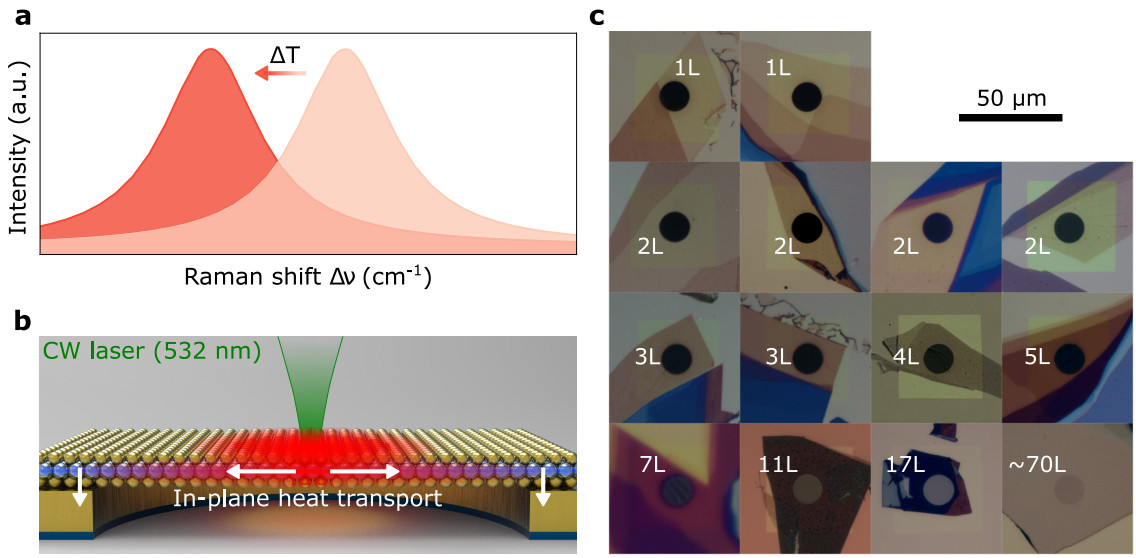


Figure 6.1: Principle of Raman thermometry and suspended samples. (a) Shift of the Raman active mode due to a temperature change. The correlation between temperature change and Raman shift enables the determination of a material's thermal conductivity. **(b)** A diagram illustrating a monolayer $MoSe_2$ suspended structure. Here, absorption of 532 nm laser light at the center of the suspended area induces localized heating, with heat simultaneously propagating towards the heat sink located at the boundary of the suspended region. **(c)** Supended $MoSe_2$ samples ranging from 1L to about 70L.

In our experimental setup, we use CW light of wavelength 532 nm to locally heat a spot of $r_0 = 1$ μm in the center of the suspended sample (see Figure 6.1b). The subsequent cooling process is facilitated by a radial diffusive heat transport mechanism that directs heat towards the edges of the suspended region, where the gold-coated substrate functions as a heat sink. We examine the temperature at the laser spot's position, representing the condition of equilibrium where the heat generated by the laser is compensated by cooling mechanisms and heat sinking. Consequently, a higher (lower) temperature at equilibrium suggests less (more) effective cooling, indicating a lower (higher) thermal conductivity for fixed thermal capacity and thickness.

6.3 Experimental results

We conduct Raman thermometry measurements on suspended $MoSe_2$ samples ranging from $1 - 70$ layers (see Figure 6.1c), corresponding to a thickness range from ≈0.7 nm to ≈50 nm. Here we exploit the temperature-sensitive A_{1g} Raman mode to understand the heat transport mechanism. The details of the fabrication and characterization of the samples are described in Chapter 3.

6.3.1 Calibration measurements

To quantify the thermal transport, it is crucial to understand how heating up the sample affects the frequency shift in the A_{1g} Raman active mode. Here we provide the results obtained for a monolayer $MoSe_2$ flake. Figure 6.2a depicts the laser power-dependent shift in peak frequency for this mode for monolayer $MoSe_2$. Notably, an increase in laser power leads to a more substantial temperature rise ΔT, resulting in a correspondingly greater red-shift in the A_{1g} peak. To establish a correlation between the red-shift $\Delta\nu$, and the temperature increase ΔT, we conduct Raman spectroscopy measurements at low incident power (3 μW) and concurrently varying the temperature of the sample stage (see Figure 6.2b).

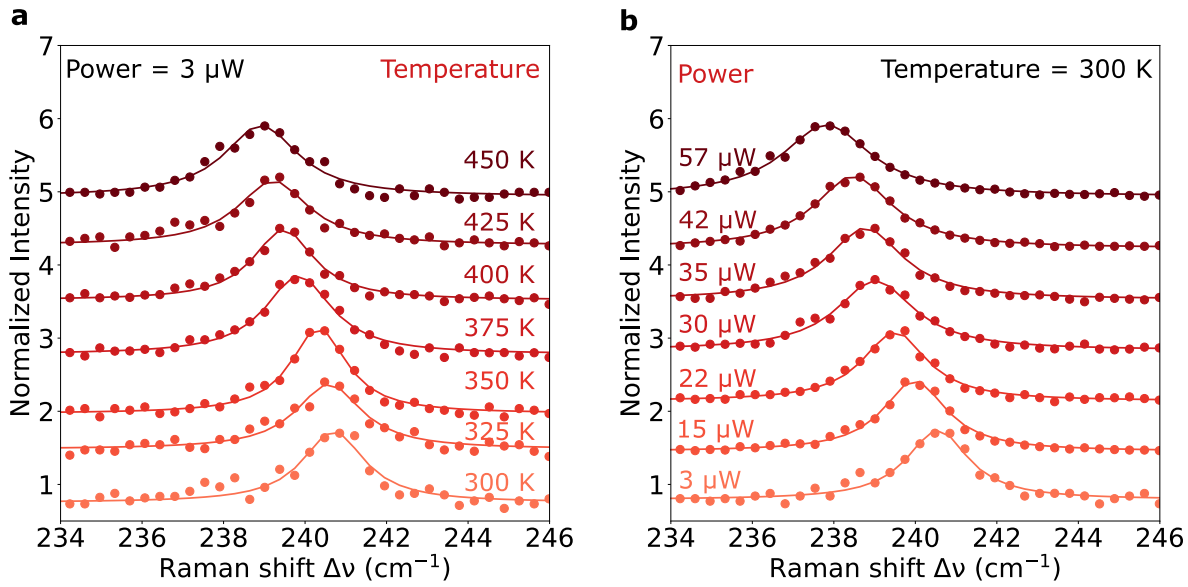


Figure 6.2: Raman thermometry measurement of a suspended monolayer $MoSe_2$. **(a)** Calibration measurements of Raman spectra at 532 nm while varying the sample temperature on the sample stage, showcasing the redshift with increasing temperature. Here, the laser power was maintained at a minimal level to prevent laser-induced heating. **(b)** Raman spectra while increasing laser power, demonstrating the redshift of the A_{1g} mode due to laser-induced heating. The spectra are (normalized and) shifted up for clarity.

We note that it is crucial to employ low laser power to prevent any unintended redshift caused by the laser's influence. For monolayer $MoSe_2$, we determine the temperature coefficients $\chi_T = \partial\nu/\partial T$ of -0.015 $cm^{-1}K^{-1}$. We also perform similar experiments on the other $MoSe_2$ samples, and the results are presented in Table 6.1. These temperature coefficients then enable us to translate the laser-induced red-shift $\Delta\nu$, of the peak of the Raman signal into a localized temperature increase $\Delta T(P)$, as a function of the laser power P.

Number of layers	χ_P **(cm^{-1} μW^{-1})**	χ_T **(cm^{-1} K^{-1})**
1L	-0.05212	-0.0155
2L	-0.02542	-0.0105
3L	-0.02306	-0.0975
4L	-0.01498	–
5L	-0.01083	-0.0067
7L	-0.00939	–
11L	-0.00564	-0.0069
17L	-0.00318	–
≈70L	-0.00860	-0.0072

Table 6.1: Summary of measured power coefficient χ_P and temperature coefficient χ_T for $MoSe_2$ flakes.

To facilitate the extraction of in-plane thermal conductivity κ, we undertake a linear regression analysis on the extracted ΔT with respect to absorbed laser power, denoted as P_{abs}. This process yields the slope, $\partial T/\partial P_{abs}$, which subsequently serves as a critical component in the equation [182]:

$$\kappa = \frac{1}{2\pi d_{th}} \cdot \left(\frac{\partial T}{\partial P_{abs}}\right)^{-1} \cdot \ln\left(\frac{r_d}{r_0}\right) \cdot \alpha \tag{6.1}$$

where r_d is the hole radius (7.5 µm) and d_{th} is the thickness of the flake, and α is a prefactor that is a function of the ratio r_d/r_0 [182]. For our experimental conditions, $\alpha \approx 1$. It is important to point out that Equation 6.1 is valid under the condition that the cooling pathway involves only in-plane diffusive heat transfer towards the edge of the suspended region. At the edge, the substrate acts as a perfect heat sink. As seen from the Equation 6.1, it is necessary to accurately determine the laser spot size, the laser power absorbed by each flake (see Section 3.4), and the flake thickness (see Subsection 3.3.1) to

quantify the in-plane thermal conductivity.

6.3.2 Raman thermometry for varying flake thickness

We will now present the results of our Raman thermometry measurements on $MoSe_2$ crystals, focusing on how these measurements vary with crystal thickness. It's crucial to note that we conduct all these experiments under vacuum conditions to prevent heat loss to the surrounding atmosphere. It has been demonstrated that heat loss to the surrounding gas can introduce significant errors when determining the thermal conductivity [183].
In Figure 6.3a, we show the temperature change ΔT as a function of absorbed power P_{abs}. A clear trend emerges with varying crystal thickness: thinner crystals exhibit more pronounced temperature increases for the same absorbed power. This observation is quite intuitive, as thinner crystals have less volume to share the same amount of heat, resulting in higher temperatures.

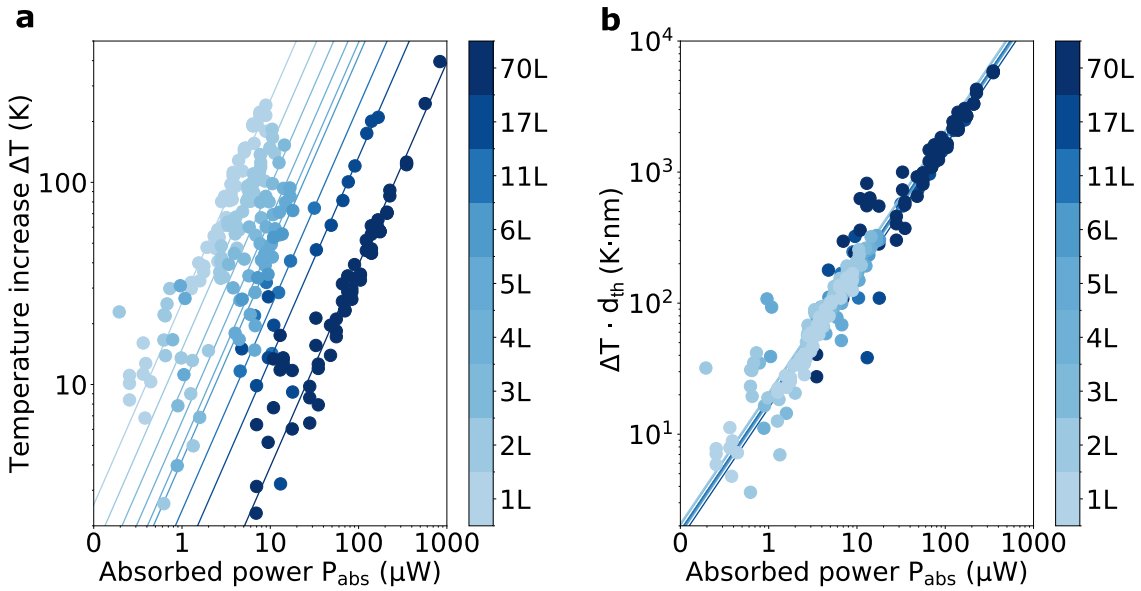


Figure 6.3: Raman thermometry of $MoSe_2$ with varying crystal thickness. (a) Temperature increase ΔT, as a function of the absorbed power P_{abs}, for $MoSe_2$ crystals of different thicknesses. **(b)** The dataset in (a), multiplied by the thickness of each crystal, allowing the slope to represent the thermal conductivity κ. Solid lines depict linear fits to the data.

When we plot $\Delta T \cdot d_{\text{th}}$ as a function of P_{abs} (see Figure 6.3b), the slope directly reflects the material's thermal conductivity κ, as per Equation 6.1. Interestingly, all data points closely converge along nearly the same slope, suggesting that the crystal thickness does not significantly alter the intrinsic thermal conductivity of $MoSe_2$.

6.4 Thermal conductivity and microscopic insights

Now we quantitatively determine κ for different thicknesses using Equation 6.1. Our systematic variation in thickness demonstrates that the effect of crystal thickness is relatively weak, with a slight decreasing trend in thermal conductivity from 70L down to monolayer thickness (see Figure 6.4a). Specifically, the thinnest samples display lower thermal conductivity compared to the thickest sample (70L). This contrasts with some values reported in the experimental literature [140, 166, 169]. We attribute this difference to variations in experimental conditions and substrate characteristics in prior studies. Many of these studies used non-coated substrates, resulting in inefficient heat sinking at the hole edge. Consequently, the boundary conditions assumed in Equation 6.1 are not satisfied, necessitating the use of a modified version of Equation 6.1 in such cases. Some studies used relatively small hole sizes, which could lead to an overestimation of absorption and consequently leading to an overestimation of the thermal conductivity, especially for monolayer samples. Furthermore, any presence of contamination on a monolayer sample can act as a thermal dissipation channel, which could affect the measured thermal conductivity. In our study, as extensively outlined in Chapter 3, we utilized substrates designed to minimize artefacts and conducted experiments with well-characterized, clean samples.

To comprehend our experimental results, we compare them with calculated[†] conductivities for bulk $MoSe_2$, and for 2D crystals with thicknesses from 6L down to the monolayer and between 300 and 500 K. We use the SIESTA program and the temperature-dependent effective potential method in density functional theory. The details of this approach can be found elsewhere [184]. In this comparison, we use a temperature of 400 K, which is more consistent with the experimental conditions. This choice is motivated by the fact that the experimental results encompass a temperature range spanning from approximately 300 K to 500 K (due to laser-induced heating, see Figure 6.3b). For the thinnest crystals, first-principles-based results at 400 K reveal a κ of 15 W/m/K, gradually increasing to 21 W/m/K for 6L, and further to 32 W/m/K for the bulk crystal. Experimental values exhibit a similar trend, starting below 20 W/m/K for the bilayer sample and rising above 20 W/m/K for 17L and 70L samples (see Figure 6.4a). Taking into account experimental uncertainties and the temperature range considered in the theoretical results, the findings are in good quantitative agreement. Importantly, both sets of results indicate that crystal thickness has a very small effect on the thermal conductivity. Additionally, any such effect observed here contrasts with the behaviour in graphite, where decreasing crystal thickness leads to an increase in thermal conductivity, with monolayer graphene exhibiting

[†]The microscopic calculations were performed by Dr Roberta Farris (see also Contributions 6.5).

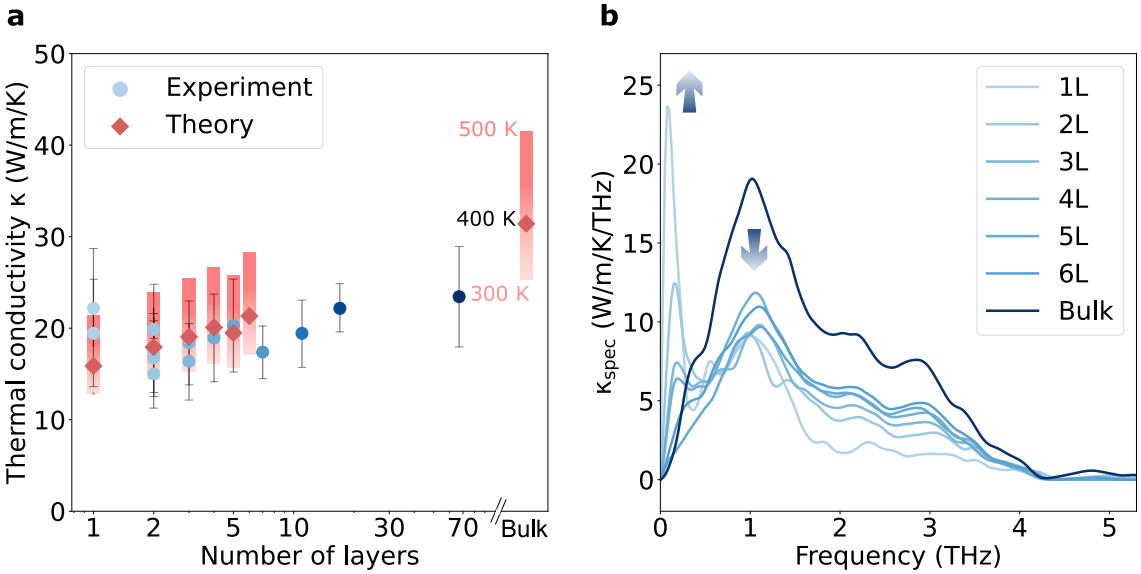


Figure 6.4: Thermal conductivity and microscopic insights into heat transport in $MoSe_2$. **(a)** Variation of in-plane thermal conductivity in $MoSe_2$ crystals with thickness, evaluated using both our experimental data (circles, 70% confidence interval) and DFT calculations (diamonds) between a temperature range of 300 and 500 K (vertical bars). **(b)** Spectrally decomposed thermal conductivity κ_{spec}, as a function of phonon frequency, revealing that with decreasing film thickness, an increasing contribution from a sub-THz mode compensates for the decreasing contribution from modes around 1 THz.

the highest thermal conductivity [13]. This is attributed to the fact that, as the number of graphene layers increases, there are more phonon states available for Umklapp scattering, which reduces the intrinsic thermal conductivity [185].

We also investigate the specific phonon contributions to the total thermal conductivity by creating a spectrally decomposed thermal conductivity plot for $MoSe_2$ (κ_{spec}, as shown in Figure 6.4b). In the case of bulk crystals, the most significant contribution arises from modes with frequencies around 1 THz. However, this contribution gradually diminishes as the crystal thickness decreases. Towards the monolayer limit, we observe that the sub-THz mode starts to play a more substantial role. This suggests that as we approach the monolayer thickness, the decreasing contribution from modes around 1 THz is effectively compensated by the increasing contribution of lower-frequency modes.

From our theoretical calculations, we also observe that in the monolayer (bilayer) $MoSe_2$ case, more than 30% (20%) of the thermal conductivity is carried by low-frequency flexural ones, with a mean free path (MFP) above 1 µm [74]. This finding also underscores the importance of using large hole sizes, as a significant fraction of the thermal conductivity is carried by phonons with MFPs of several microns [74, 186]. Both the experimental and theoretical findings point to a relatively minor effect of $MoSe_2$ thickness on the thermal conductivity.

6.5 Summary

In summary, we have utilized both Raman thermometry and *ab initio* simulations to explore how the thickness of suspended $MoSe_2$ crystals affects their ability to conduct heat within the crystal lattice. We have observed excellent agreement between our experimentally measured and the computed in-plane lattice conductivities. Both methods point to a relatively minor effect of crystal thickness on how efficiently heat is conducted — within a range of about two times. This weak influence of thickness on the thermal conductivity is the result of compensating effects in the phonon contribution to the thermal conductivity. The insights gained from our study hold significance for the design of (sub-)nanometer-thick TMD-based optoelectronic devices. Furthermore, beyond the immediate implications for thermal conductivity, these measurements hold promise for extracting additional thermal properties. Once the thermal diffusivity is quantified from spatiotemporal thermometry measurements, we can obtain the thickness dependence of heat capacity indirectly ($C_\mathrm{v} = \kappa/D$).

Contributions

Sebin Varghese and David Saleta Reig fabricated the samples and performed the Raman thermometry measurements. Sebin Varghese and David Saleta Reig were trained by Dr Marianna Sledzinska and Dr Emidgio Chávez-Ángel to use the Raman thermometry setup. David Saleta Reig analyzed the Raman thermometry data with inputs from Sebin Varghese, Jake Dudley Mehew, and Alexander Block under the supervision of Prof. Klaas-Jan Tielrooij. Roberta Farris performed *ab initio* calculations under the supervision of Prof. Pablo Ordejón, Prof. Zeila Zanolli, Prof. Klaas-Jan Tielrooij, and Prof. Matthieu. J. Verstraete with inputs from Dr Olle Hellman. The experimental and theoretical results were discussed and interpreted together with David Saleta Reig, Dr Jake Dudley Mehew, Dr Alexander Block, Prof. Matthieu. J. Verstraete, and Prof. Klaas-Jan Tielrooij.

7

Heat transport: From diffusive to viscous

"The universe is under no obligation to make sense to you." - Neil deGrasse Tyson

In this Chapter, we explore the heat transport properties of $MoSe_2$ and MoS_2 down to the monolayer limit using the spatiotemporal thermometry technique. We begin by optimizing the key parameters for such measurements and then quantify thermal diffusivity as a function of material thickness. From our experiments, we unravel a remarkable transition from diffusive behaviour to viscous heat transport in ultrathin (1 and 2L) suspended layers of $MoSe_2$ and MoS_2 at room temperature. This phenomenon is manifested by a very narrow spatial temperature profile which also has a negative dip a few microns away from the photogenerated heat source, suggesting a thermal diffusivity that suddenly decreases by more than an order of magnitude. We attribute such a temperature profile to a hydrodynamic type of heat flow, which has never been observed in transition metal dichalcogenides (TMDs) at any temperature.

This Chapter is based on the following work:
S. Varghese, J. Tur Prats, J. D. Mehew, D. Saleta Reig, R. Farris, J. Camacho, J. A. Haibeh, A. Sokolov, P. Ordejón, S. Huberman, A. Beardo, F. X. Alvarez, and K. J. Tielrooij, Non-diffusive heat transport in ultrathin layered semiconductors at room temperature, *In preparation.*

7.1 Introduction

In Chapter 2, we discussed that heat transport can be either diffusive, following Fourier's law, or non-diffusive, which includes ballistic and hydrodynamic behaviours. Several experimental studies have observed such non-diffusive transport phenomena in different material systems. When the mean free path of the system is comparable to the system size or the size of the heat source, quasi-ballistic heat transport behaviour has been observed in various systems [7, 75, 81–87]. On the other hand, in the Ziman regime, where Normal scattering events dominate over resistive scattering events, unique thermal transport phenomena such as second sound [93, 96–99, 106], Knudsen minimum [95, 101], lattice cooling [103], and Poiseuille flow have also been reported [91, 100–102]. These phenomena are manifestations of phonon hydrodynamics, where the collective motion of phonons resembles the behaviour of fluids. Additionally, phonon hydrodynamics at the nanoscale has been reported when there is a slow relaxation of the heat flux relative to the length and time scales of the experiment. As we discussed in Subsection 2.5.3, in such cases, it is not necessary to have Normal scattering to be dominant over Umklaap scattering to observe phonon hydrodynamics [67, 77, 78, 108–112, 114, 115].

Theoretical predictions suggest that phonon hydrodynamic transport can occur in layered 2D materials, including TMDs, over a range of temperatures. This behaviour, specifically the second sound phenomena, extends above room temperature in materials such as graphene, boron nitride, and graphane [68, 105]. For example, Ref. [105] predicted that Normal scattering dominates over Umklapp scattering in several 2D materials, including graphene and MoS_2. In graphene, the second sound contribution is significant (about 40%), resulting in second sound propagation lengths reaching the micron scale at room temperature. In contrast, for MoS_2, the second sound contribution is about 10%, with a shorter propagation length of approximately 100 nm at room temperature. While such behaviour has been predicted in 2D materials, experimental observations are still limited at higher temperatures. Second sound has been observed in multilayer graphene using the transient thermal grating (TTG) technique, but only up to a temperature of 200 K [106]. In contrast, no signatures of hydrodynamic heat flow have been detected in transition metal dichalcogenides at any temperature. These observations of phonon hydrodynamics in graphite were identified by detecting the damped oscillations of the TTG amplitude, with the signal falling below zero, for grating periods ranging from 6 μm at 100 K to 2 μm at 200 K. This suggests that to observe such phenomena at room temperature, a grating period of less than a micron may be required, which is currently challenging to achieve with the spatial (and temporal) resolution of conventional thermometry techniques.

In this Chapter, we take advantage of the high spatial resolution of our spatiotemporal

pump-probe thermometry technique to track such observations in TMD thin films. We present the first-ever experimental evidence of viscous heat transport in monolayer and bilayer $MoSe_2$ and MoS_2, and at room temperature, which we interpret as a hydrodynamic type of heat diffusion.

7.2 Diffusive heat transport with flake thickness, f_{mod} = 240 kHz

For the experiments (in vacuum), we select a modulation frequency f_{mod} of 240 kHz. Our prior measurements motivated this choice, where we obtained similar diffusivity values for thick $MoSe_2$ sample (see Section 5.14) across a range of modulation frequencies. Using high f_{mod} could potentially help in avoiding overheating of the sample caused by pump pulses, given that we only apply ≈160 pump pulses ($0.5 \times f_{rep}/f_{mod}$), where f_{rep} is the laser repetition rate (76 MHz), within a pump-on window (see also Appendix Section A4 and Section A5).

7.2.1 Linearity with pump fluence

As usual, the first step is to investigate the decay dynamics and assess the linearity of the signal with fluence. Figure 7.1a illustrates the decay dynamics of an 8-layer $MoSe_2$ sample

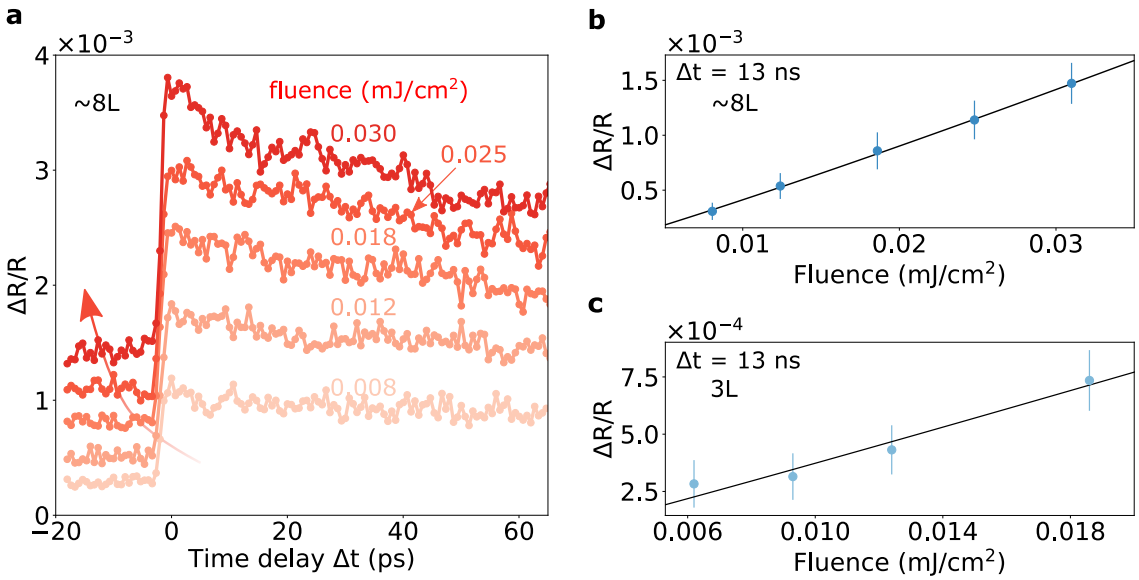


Figure 7.1: Decay dynamics with pump fluence. (a) Fluence-dependent decay dynamics in 8-layer suspended $MoSe_2$. **(b, c)** Analysis of transient reflectivity signal at Δt of 13 ns for (b) 8-layer and (c) 3-layer $MoSe_2$ sample. Solid lines are power-law fit, yielding the exponent of the fit to be around 1.04, suggesting that the relationship is close to linear.

in the suspended region. The signal increases with pump fluence as expected and shows a sharp rise at time-zero (Δt = 0 ps) followed by a gradual decay. Figure 7.1b depicts

the signal ($\Delta t = 13$ ns) plotted against the pump fluence for this 8-layer sample, while a similar measurement on a 3-layer sample is presented in Figure 7.1c (see Appendix A.4 for data on the monolayer and bilayer sample). Notably, the signal is linear with pump fluence and this is a crucial prerequisite for heat transport measurements because it means that we can consider the transient reflectivity $\Delta R/R$ profile as representative of the temperature profile.

To further validate the linear regime, in Figure 7.2a, we present spatial profiles for a 7-layer $MoSe_2$ sample obtained at various pump fluences. We observe that the signal increases with pump fluence. The normalized plot in Figure 7.2b illustrates that these profiles overlap, confirming the linear regime.

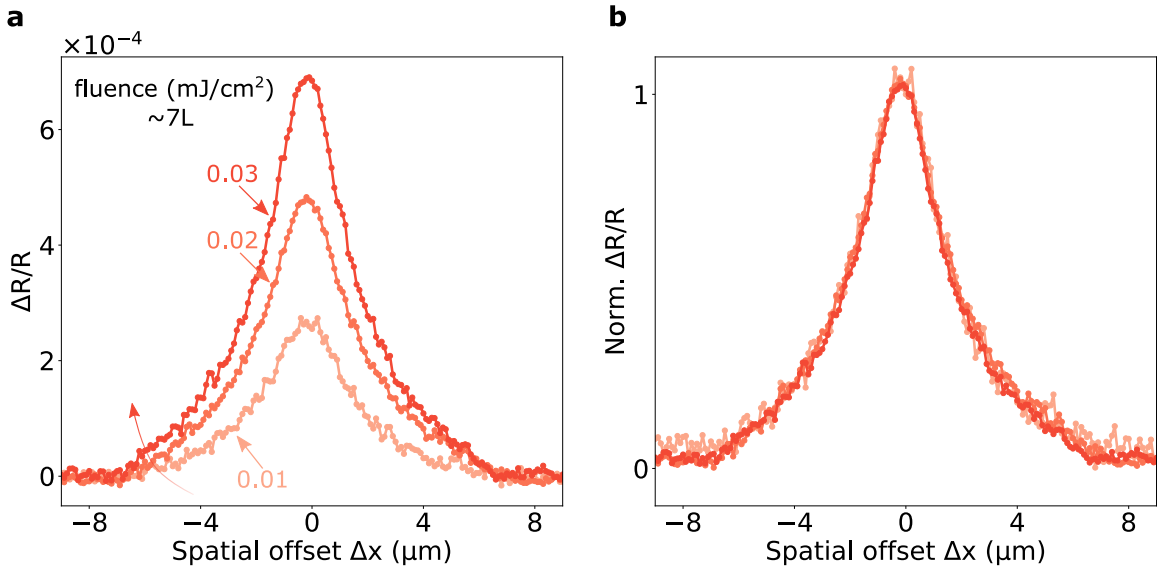


Figure 7.2: Spatial profiles with pump fluence. (a) Fluence-dependent spatial profiles (at $\Delta t = 13$ ns) in 7-layer suspended $MoSe_2$. **(b)** Normalized transient reflectivity signal for the profiles in panel (a) confirming the linear dependence of signal with laser fluence.

7.2.2 Effect of flake thickness

After confirming the linear relationship of the transient reflectivity signal with pump fluence, we proceed to measure the spatial temperature profile of suspended $MoSe_2$ at different thicknesses. In Figure 7.3, we present spatial profiles (in-phase) ranging from trilayer to about 20 layers (see Appendix Figure A.5 for the out-of-phase profiles).

Interestingly, we find that the spatial profiles for flakes with a thickness down to 3 layers look very similar qualitatively. They all exhibit a gradual decrease in the signal towards the heat sink, where $\Delta R/R$ and thus ΔT is zero. Using our simulation based on heat diffusion, we accurately describe these profiles and quantify the in-plane thermal diffusivity. Our model fits well across all the samples, particularly noticeable until the 3-layer thickness, as

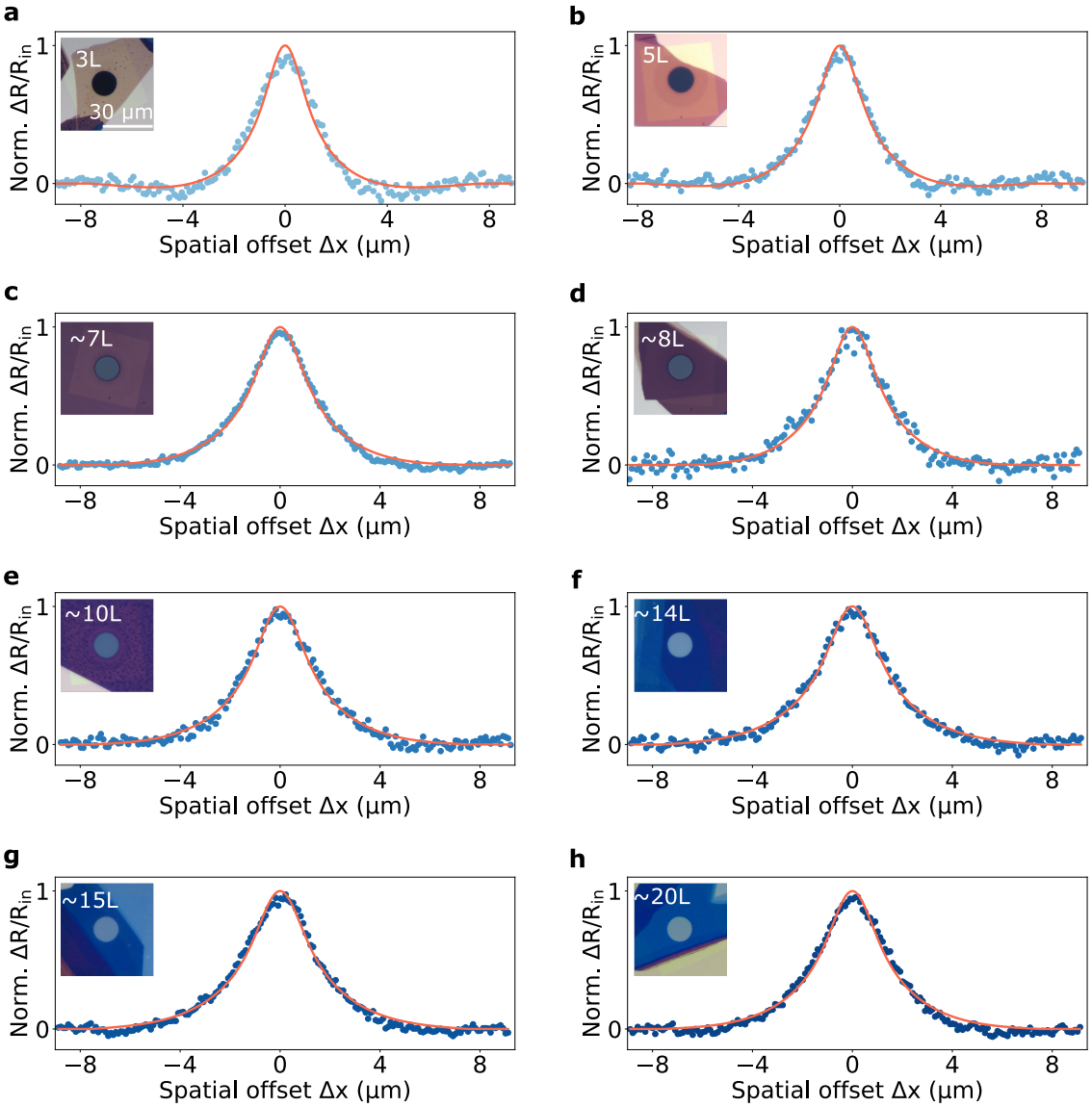


Figure 7.3: Suspended samples and obtained spatial profiles in $MoSe_2$. (a-h) Normalized (to the peak of the fit) transient reflectivity signals (in-phase) measured on suspended $MoSe_2$ flakes of varying thicknesses, ranging from 3 layers to 20 layers. The blue scatters represent the experimental datasets, while the solid lines are the fits obtained using the diffusive heat transport model based on Fourier's law. The insets in each panel display optical images of the $MoSe_2$ samples under investigation. The scale bar in (a) is valid for all the images.

shown in Figure 7.3. Systematically varying the thickness, we find a moderate decreasing trend in the thermal diffusivity from 20 layers down to trilayer thickness, see Figure 7.4.

7.2.3 Comparison with Raman thermometry

To confirm the validity of our results, we conduct a comparison between the obtained thermal diffusivity (in-phase channel) and the thermal conductivity κ data obtained from

Raman thermometry (see Section 6.4) on similar suspended samples. Remarkably, we find that the two sets of data exhibited excellent agreement, demonstrating the efficacy of our novel spatiotemporal thermometry technique (see Figure 7.4). For this comparison, we use the bulk heat capacity of 1.87×10^6 $\mathrm{Jm^{-3}K^{-1}}$ [163] to convert the thermal conductivity to thermal diffusivity. We also observe a similar trend for the diffusivity obtained by fitting the out-of-phase channel (see Appendix Figure A.6).

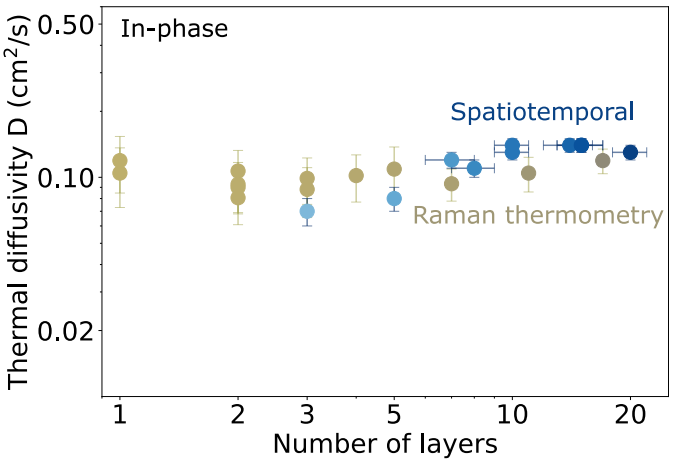


Figure 7.4: Comparison with Raman thermometry. Obtained thermal diffusivities (in-phase) for $MoSe_2$ from spatiotemporal measurements (blue scatters) and Raman thermometry (yellow-green scatters, see also Chapter 6), as a function of flake thickness.

7.3 Viscous heat transport

We will now take a closer look at the experimental profiles (in-phase) obtained for the monolayer and bilayer $MoSe_2$ films. First, we will examine the observations of the viscous heat transport, followed by an exploration into understanding the underlying mechanisms behind this.

7.3.1 Experimental results

To investigate the thermal transport of these ultrathin flakes, we analyze their measured spatial profiles. The thinnest flakes exhibit significantly narrower spatial profiles compared to trilayer and thicker flakes. Furthermore, unlike trilayer and thicker flakes, which exhibit a consistently decreasing spatial profile away from the center (pump spot), the thinnest flakes display a non-monotonic spatial profile. Specifically, the in-phase component of the transient reflectivity signal dips below zero around 2 microns away from the pump spot (see Figure 7.5). This negative signal gradually diminishes towards the suspended

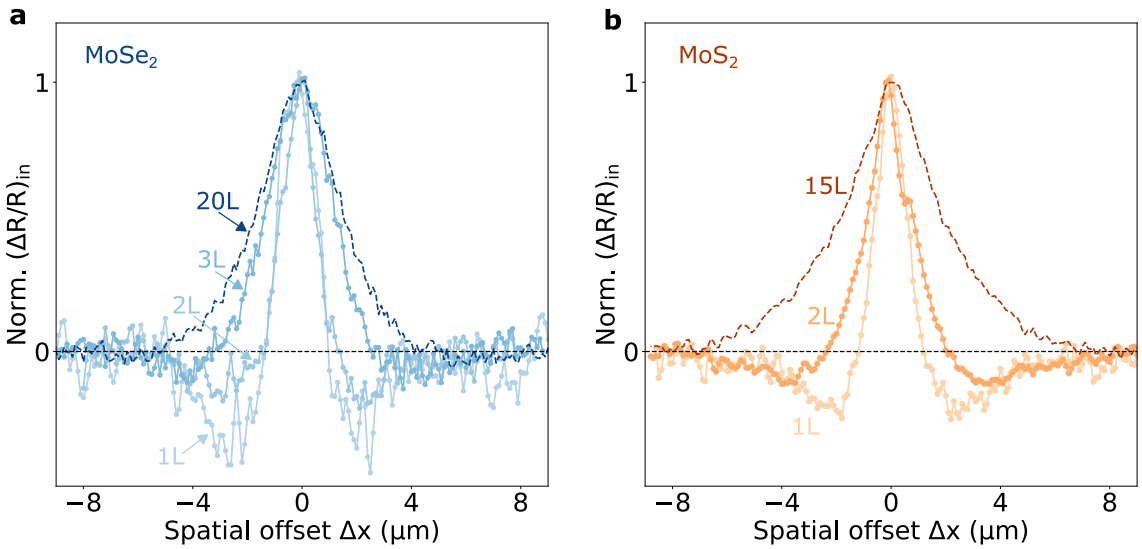


Figure 7.5: Experimental observation of viscous heat transport. (a, b) Comparison of normalized transient reflectivity signals (in-phase) measured on ultrathin samples: (a) $MoSe_2$ and (b) MoS_2, with the spatial profile of a thick sample. The narrow profile for ultrathin flakes and the appearance of a negative amplitude around 2 μm indicate signatures of viscous heat transport.

region's edge. We also observe similar narrow spatial profiles with negative amplitude for monolayer and bilayer MoS_2 (see Figure 7.5b).

7.3.2 Effective Fourier description

To comprehend the underlying cause of the significantly narrow profile with a sign-change observed in ultrathin $MoSe_2$ and MoS_2, we initially investigate whether the Fourier model, as discussed in Sections 5.6 and 5.9, can replicate the experimental findings. In Section 5.9, we demonstrated the Fourier model along with lock-in operation to understand the X (in-phase) and Y (out-of-phase) signals for a diffusivity of 0.20 cm^2/s. Given that the experimental spatial profile for monolayer and bilayers are significantly narrow, we now perform the same simulation with an ultralow diffusivity of 0.01 cm^2/s (f_{mod} = 240 kHz). Figure 7.6a illustrates the temperature dynamics for multiple pump-on and pump-off periods. It is evident that the temperature does not decay during the off state; a significant amount of undecayed signal remains before the second pump-on period. As we previously showed in Section 5.9, this results in a significant amount of out-of-phase signal. Another interesting observation is that at around 2 μm, the temperature rises very slowly during the pump-on window and decreases very slowly during the pump-off window.

The smaller diffusivity causes the heat to arrive during the pump-off period at a location increasingly close to the center. For example, heat arrives at 2 microns when the pump is in the off state. The temperature dynamics is π out-of-phase, resulting in a negative

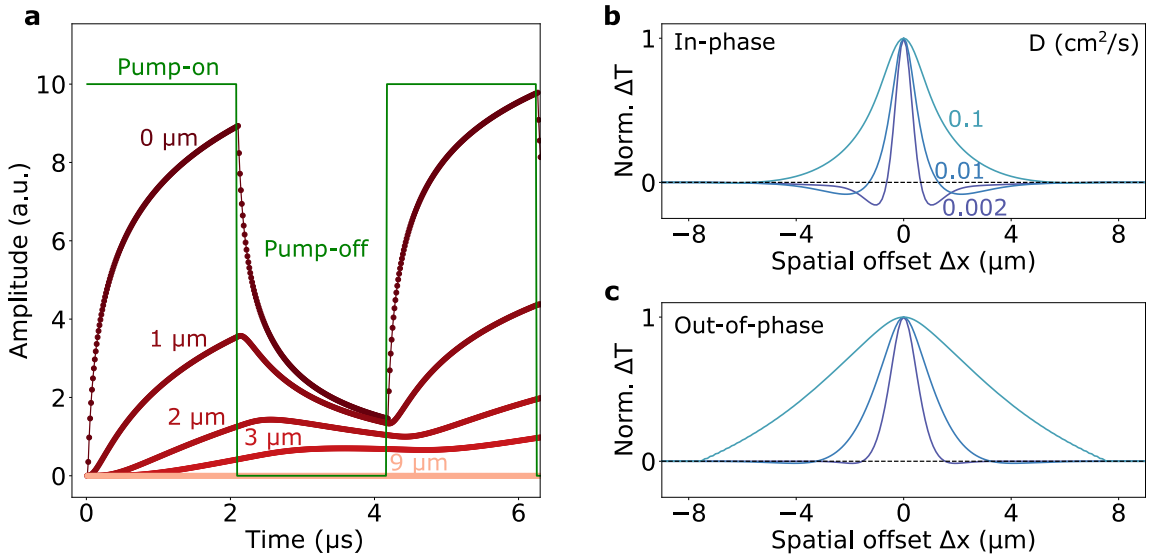


Figure 7.6: Fourier modelling with ultralow diffusivity. (a) Simulated temperature dynamics ($D = 0.01$ cm^2/s) at every $\Delta t = 13$ ns (scatters) during square wave (green line) modulation ($f_{\text{mod}} = 240$ kHz) cycles. **(b, c)** The normalized in-phase and out-of-phase profiles after averaging the sine and cosine multiplied temperature dynamics at different positions.

in-phase signal (the out-of-phase signal is $\pi/2$ out-of-phase). Another way to see this is as follows: when the temperature dynamics are multiplied by the sine wave, a significant portion of the negative part of the sine wave is multiplied by the off-state temperature dynamics. Consequently, when performing the average, regions in the spatial profiles will exhibit negative amplitude. To further understand the behaviour of the non-monotonous temperature profile, we perform simulation for different diffusivities (see Figures 7.6b,c). We observe that the amplitude of the negative dip in the in-phase channel decreases with increasing diffusivity. For a diffusivity of 0.10 cm^2/s, which corresponds to the D of multilayer $MoSe_2$ sample, the simulated profile becomes monotonous, exhibiting no negative dip.

With this understanding, we now attempt to describe the experimental profiles of ultrathin $MoSe_2$ and MoS_2 flakes. The Fourier model successfully captures some key features of the experimental profiles, including a narrow central region with negative signals outside this central part (see Figure 7.7). However, the Fourier model could not accurately describe the amplitude of the dip observed in the experimental data. We can also see that the quality of the fit is significantly poorer compared to that of the thicker flakes (see Figure 7.3). From the fit, we obtain extremely low diffusivity values, between $0.01 - 0.02$ cm^2/s, for monolayer samples. This ultralow diffusivity is inconsistent with both experimental observations [74, 140, 166, 168, 177–179, 187] and theoretical calculations [180, 181, 186] in TMDs. Specifically, the diffusivities for monolayers and bilayers are an order of magnitude lower than that of the 20-layer sample. This discrepancy suggests that there is more

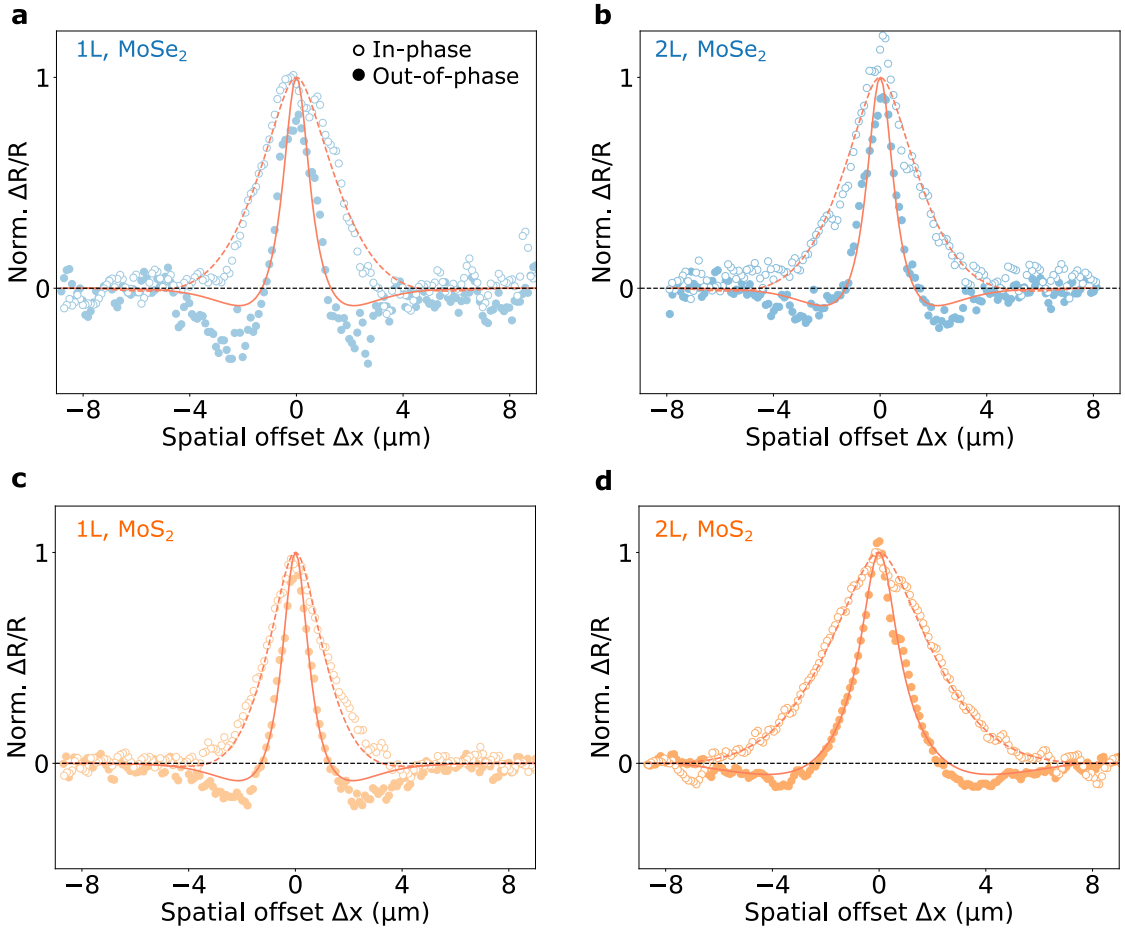


Figure 7.7: Effective Fourier description. (a-d) Normalized in-phase (filled circles) and out-of-phase (open circles) experimental profiles described using the Fourier model (solid red line for in-phase and dashed red line for out-of-phase). The fit yielded a diffusivity of 0.01 cm^2/s (in-phase) and 0.02 cm^2/s) (out-of-phase) for both (a) monolayer and (b) bilayer $MoSe_2$. The diffusivity for MoS_2 is found to be 0.01 cm^2/s for the (c) monolayer and 0.04 cm^2/s for the (d) bilayer.

to understand about heat transport in these materials. The significant reduction in conductivity/diffusivity points to the possibility of a non-diffusive transport mechanism, in particular viscous heat flow.

7.3.3 Discussion

The occurrence of a negative transient reflectivity signal at specific pump-probe delays has been observed in graphitic materials [103], where it was attributed to hydrodynamic lattice cooling. Similar observations were made using transient thermal grating in graphite, where the temperature signal oscillates around zero [93, 106], indicating second sound, a manifestation of hydrodynamic heat transport. However, these observations, including Knudsen minimum and Poiseuille flow, which are signatures of hydrodynamic transport

(see also Subsection 2.5.2), are only seen in materials where momentum-conserving Normal scattering dominates over Umklapp scattering ($N \gg U$). This dominance usually occurs at temperatures well below room temperature, though exceptions exist in 2D materials where it is predicted to persist even above room temperature [105].

In the case of MoS_2 at room temperature, as theoretically calculated [105], although Normal scattering dominates over Umklapp, the scattering rates are comparable, meaning that the Guyer-Krumhansl criteria is not met. This suggests that conventional hydrodynamic transport conditions cannot explain our observations in ultrathin $MoSe_2$ and MoS_2, implying that the less strict formalism of hydrodynamic phonon transport might provide a better explanation. This new hydrodynamic regime (see also Subsection 2.5.3), unlike the Ziman limit ($N \gg U$), does not necessarily require momentum-conserving Normal scattering to be dominant over Umklapp scattering. This regime has been predicted [67] and observed in various materials [110, 113, 115] where the relaxation of heat flux is slow compared to the experimental length and time scales, often resulting in a reduction in thermal conductivity [78].

This hydrodynamic formalism incorporates a non-local term into the heat transport equation (see also Subsection 2.5.3). The non-local length parameter ℓ, represents the extent of the collective or fluid-like thermal transport away from the heat source. Microscopically, ℓ is a phonon mean free path Λ weighted average (see Equation 2.25). As reported previously, for monolayer and bilayer systems, the Λ of flexural modes extends to several microns [186]. These long Λ phonons could contribute to a large non-local length, and thus to hydrodynamic behaviour at these thicknesses. Additionally, the phonon lifetime of these low-frequency, long mean free path modes is quite high, approaching a nanosecond for TMDs and several nanoseconds for monolayer $MoSe_2$ [186]. These modes contribute significantly to κ, with more than 30% of κ in monolayer $MoSe_2$ and 20% in bilayer $MoSe_2$ is attributed to modes with Λ exceeding 1 micron [74, 186].

Another notable aspect of ultrathin TMDs is the variation in their mechanical properties. For example, the thermal expansion coefficient significantly increases as the material thickness decreases. In $MoSe_2$, the thermal expansion coefficient rises from 0.7×10^{-5} K^{-1} for bulk material to 5.4×10^{-5} K^{-1} in bilayer and 10.6×10^{-5} K^{-1} in monolayer [188]. Although the change in thermal expansion coefficient for MoS_2 is not as pronounced as for $MoSe_2$, it still increases by approximately six times from bulk (1.1×10^{-5} K^{-1}) to monolayer (6.5×10^{-5} K^{-1}) [188]. These drastic changes in the thermal expansion coefficient could introduce a thermoelastic contribution to heat transport in these thin layers. This effect was initially introduced in the work by Guyer and Krumhansl [89] and originally derived in Ref. [189]. Such thermoelastic effects can create inhomogeneous strain at the nanoscale [189], potentially modifying the phonon dispersion relation and phonon

velocities and thus affecting heat transport properties. Very recently, it was shown that in silicon nanoribbons, inhomogeneous strain resulted in a 34% reduction in the thermal conductivity [190].
All these considerations suggest that our observations could be due to phonon viscous flow, thermoelastic effects, or a combination of both. Notably, these phenomena have never been observed in TMDs at any temperature before, highlighting the novelty and significance of our findings.

7.4 Summary

In summary, using spatiotemporal thermometry, we have explored the heat transport properties of $MoSe_2$ and MoS_2 as a function of flake thickness. Our results on $MoSe_2$ have shown great consistency with thermal conductivity results obtained through Raman thermometry. We have observed a remarkable transition from conventional diffusive behaviour to viscous heat transport in ultrathin (1 and 2L) suspended layers of $MoSe_2$ and MoS_2 at room temperature. This phenomenon is evidenced by a very narrow spatial temperature profile, featuring a negative dip a few microns away from the photogenerated heat source. We attribute this profile and reduction in thermal diffusivity to a hydrodynamic type of heat transport.

Contributions

Sebin Varghese fabricated the suspended samples (along with David Saleta Reig), performed the spatiotemporal measurements, and analyzed the datasets under the supervision of Prof. Klaas-Jan Tielrooij. The experimental results were discussed and interpreted together with Dr Jake D. Mehew, Jordi Tur Prats, Dr Albert Beardo Ricol, Prof. F. Xavier Alvarez Calafel, and Prof. Klaas-Jan Tielrooij.

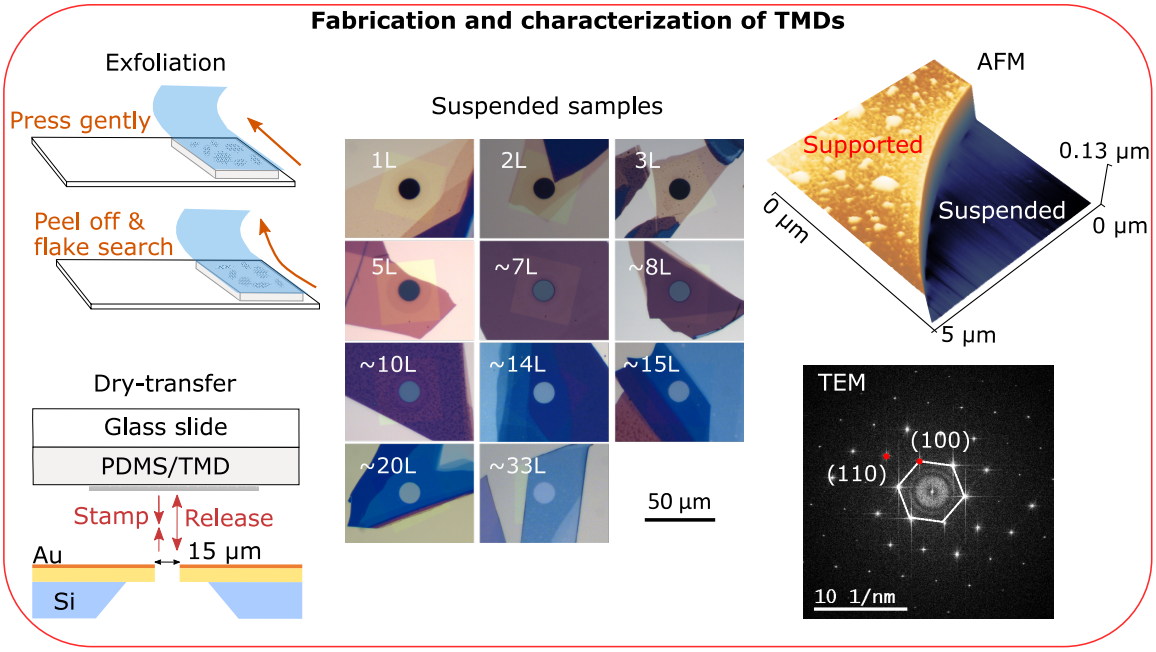
8

Conclusion

"The science of today is the technology of tomorrow."- Edward Teller

8.1 Summary

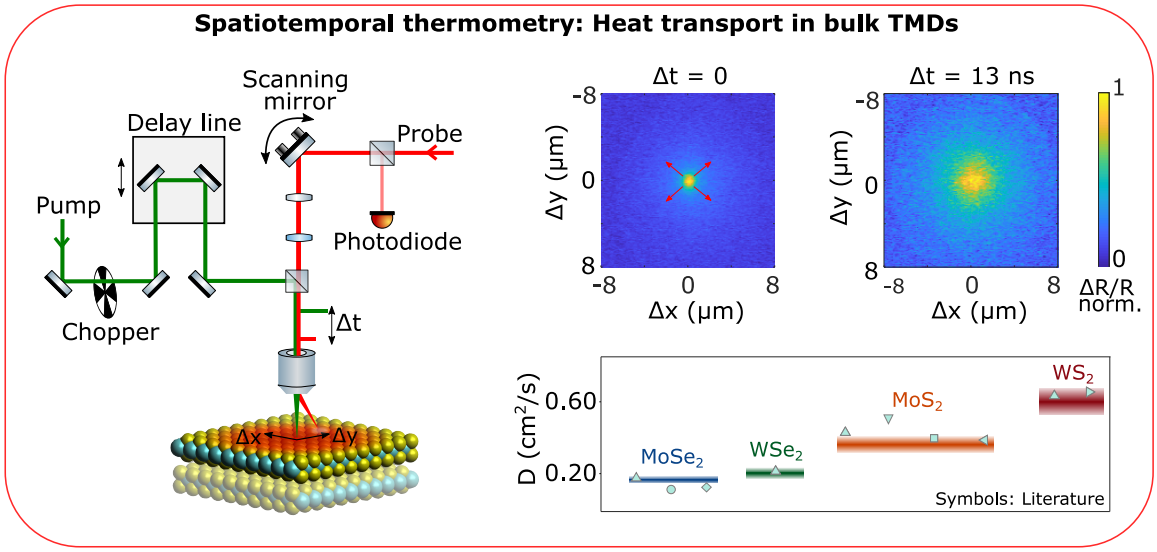
In this thesis, we investigated heat transport in layered semiconductors, aiming to advance our understanding of heat transport phenomena in these materials. The thesis began with the fabrication and characterization of transition metal dichalcogenides (TMDs), developed an experimental technique to study heat transport, and presented specific experimental findings of heat transport peculiarities down to the monolayer limit.



First, we explained the fabrication of suspended flakes of TMDs using mechanical exfoliation and dry transfer techniques. This process involves exfoliating flakes from a bulk crystal and transferring them onto a substrate with a 15 μm diameter hole using a home-built

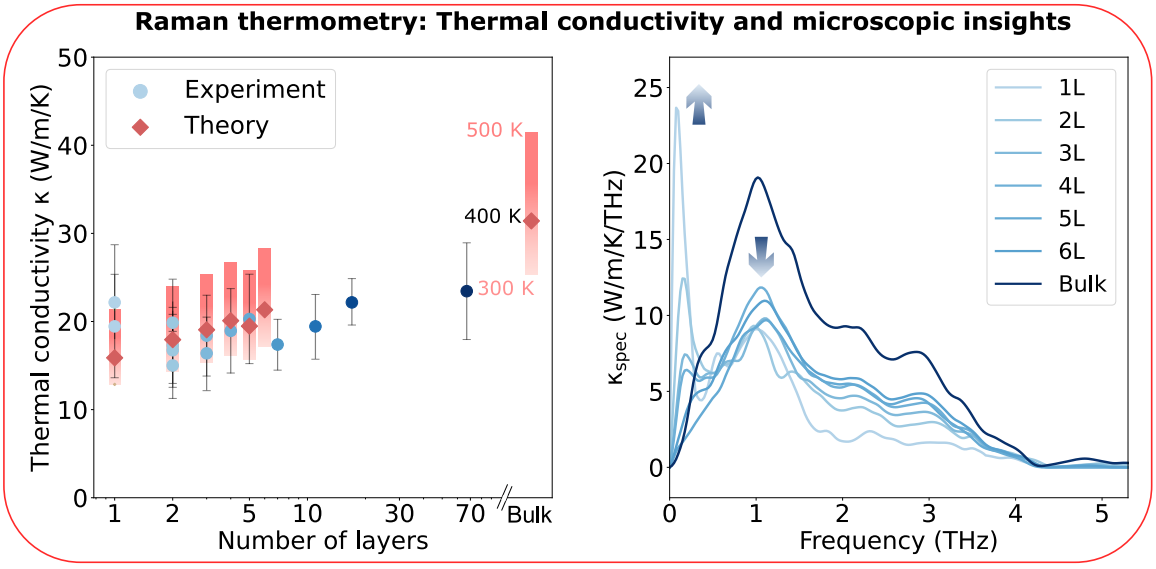
dry transfer stage. We detailed the methods used to characterize these flakes through several techniques, achieving clean, highly crystalline, wrinkle-free, and minimally strained samples, which are essential for accurate heat transport studies.

Second, we have developed a novel experimental setup—spatiotemporal pump-probe thermometry—to study heat diffusion in suspended TMDs. We provided a comprehensive explanation of the experimental setup and the calibration procedures required, such as achieving precise temporal and spatial overlap of the pump and probe pulses. This technique enables probing of in-plane heat (and charge) diffusion with high spatial and temporal resolution. Additionally, we demonstrated the setup's utility by determining the carrier diffusion in gold, validating the accuracy and effectiveness of our approach.

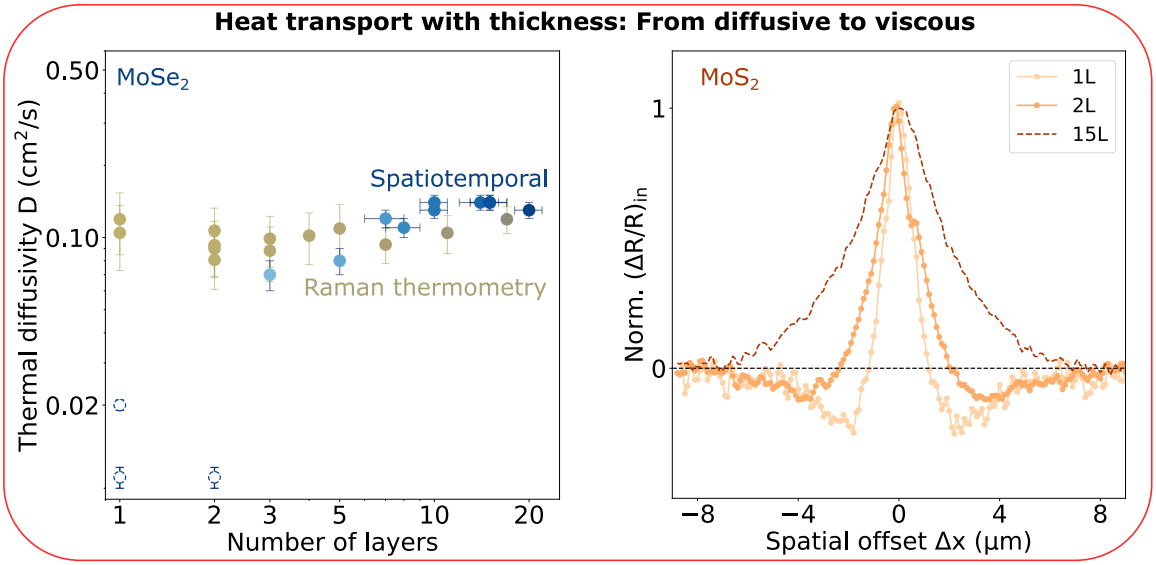


Next, using the spatiotemporal pump-probe thermometry technique, we directly measured the thermal diffusivity of four prototypical TMD materials. By leveraging the undecayed part of the temperature gradient between two pulses, we tracked heat diffusion up to the nanosecond regime. This method, unlike several existing techniques, allows for the quantification of thermal transport without requiring specific material input parameters or causing significant heating. We determined the thermal diffusivity values for $MoSe_2$ (0.18 cm^2/s), WSe_2 (0.20 cm^2/s), MoS_2 (0.35 cm^2/s), and WS_2 (0.59 cm^2/s) directly and for the first time.

Additionally, we used Raman thermometry as a complementary technique to study the thermal conductivity of $MoSe_2$ down to the monolayer limit. Our experimental findings revealed a subtle dependence of thermal conductivity (around 22 W/m/K) on flake thickness, extending from several tens of nanometers to monolayer flakes. This observation was supported by *ab initio* simulations, which highlight the significant role of low-frequency phonon modes, around 0.1 THz. These low-frequency flexural modes compensate for the reduction in thermal conductivity as the thickness approaches the monolayer limit.



When exploring the heat transport properties of layered TMDs as a function of flake thickness using the spatiotemporal pump-probe thermometry technique, we identified a transition from conventional diffusive behaviour to viscous heat transport in ultra-thin suspended $MoSe_2$ and MoS_2 at room temperature. The thermal diffusivity measurements from 20-layer to 3-layer samples aligned well with Raman thermometry results. However, for monolayer and bilayer samples, we observed very narrow spatial profiles along with a sign change around 2 microns away from the heating spot. The thermal diffusivities obtained for ultrathin flakes ($0.01-0.02$ cm^2/s) were an order of magnitude lower compared to the 20-layer flakes. We attributed this sharp decrease in thermal diffusivity to phonon hydrodynamic transport, a phenomenon that had not been observed previously in TMDs at any temperature.



Through these experiments, we significantly advanced the understanding of complex heat

transport processes in layered semiconductors using our novel spatiotemporal thermometry technique and conventional Raman thermometry.

8.2 Outlook

The research presented in this thesis lays the groundwork for several promising avenues of future exploration. The novel spatiotemporal microscopy technique developed in this study is capable of studying heat and charge diffusion dynamics beyond layered semiconductors, including materials such as MXenes, perovskites, and ferroelectrics.

The observation of viscous heat transport in ultrathin layered semiconductors opens up new possibilities for detailed experimental exploration. Future studies could investigate this phenomenon by varying key parameters, such as temperature or strain. Extending these investigations to different two-dimensional materials could provide valuable insights into the universality of viscous and non-diffusive heat transport. Additionally, this technique can be used to study heterostructures and twisted samples, broadening the scope of materials and configurations that can be explored.

In principle, the findings of this research should have implications for various fields, including heat management and thermoelectric energy conversion. For example, the concentration of heat at the hotspot, as observed in the materials studied, suggests that these materials could be used to improve the efficiency of thermoelectric devices by localizing heat where it is most needed for energy conversion. Exploring novel geometries to manipulate heat flow for tailored thermal management solutions could pave the way for innovative heat-spreading materials and directional heat-routing structures, further enhancing efficiency in electronic devices and thermoelectric systems.

A
Appendix

A1. Python script

Click here to get the Python script for solving the heat diffusion equation. You can use this script to perform the lock-in operation to the simulated temperature dynamics. Links to the example data sets to run the lock-in operation script are provided within the script. If you have any questions, please write to to.svarghese@gmail.com.

A2. Experimental beam width calculation

Prior to our spatiotemporal measurements, we characterize the beams by measuring the beam profile with a knife edge method [148], and determine the width of the pump ($\sigma_{\text{ke_pu}}$) and probe beams ($\sigma_{\text{ke_pr}}$), see also Figure 4.4e. To calculate the individual experimental beam widths (σ_{pu} and σ_{pr}), we first fit the time-zero spatial profile (after subtracting $\Delta t < 0$) with a single Gaussian function and obtain the width ($\sigma_{\Delta t=0}$). This shape corresponds to the convoluted pump and the probe profiles. Hence, we solve the following relation,

$$\sigma_{\text{pu}}^2 + \sigma_{\text{pr}}^2 = \sigma_{\Delta t=0}^2 \tag{A.1}$$

to obtain the experimental beam widths by assuming the ratio between experimental beam widths remains identical to the knife-edge measurements ($\frac{\sigma_{\text{ke_pu}}}{\sigma_{\text{ke_pr}}} = \frac{\sigma_{\text{pu}}}{\sigma_{\text{pr}}}$).

A3. Necessity of vacuum in measuring thin films

Initially, we conduct spatiotemporal measurements under ambient conditions to quantify the thermal diffusivity of suspended $MoSe_2$ samples. As described in Chapter 5, our approach involved heating the center of the suspended region and examining the spatial temperature profile at a small negative time delay (equivalent to a pump-probe delay $\Delta t = 13$ ns). By describing these profiles with a diffusive model based on Fourier's law,

we quantify the in-plane thermal diffusivity of the sample under investigation. Figure A.1a shows such profiles for a few different thicknesses of $MoSe_2$. For these measurements, we use a pump wavelength (third harmonic output) between $530 - 537$ nm at a modulation frequency of 4.37 kHz, and a probe wavelength between $795 - 805$ nm (second harmonic output), i.e., tuned to the exciton resonance of the sample. We observe that the spatial profiles become narrower towards the monolayer limit. Intuitively, as explained before (see Section 5.6), this narrow profile means less heat spreading and consequently yields lower diffusivity values. However, it is crucial to note that these obtained diffusivity values, depicted in Figure A.1b, are "apparent diffusivity" (D_{app}). This is because the Fourier model we use (Equation 5.4) inherently neglects any out-of-plane heat transport, including heat transfer to the surrounding environment.

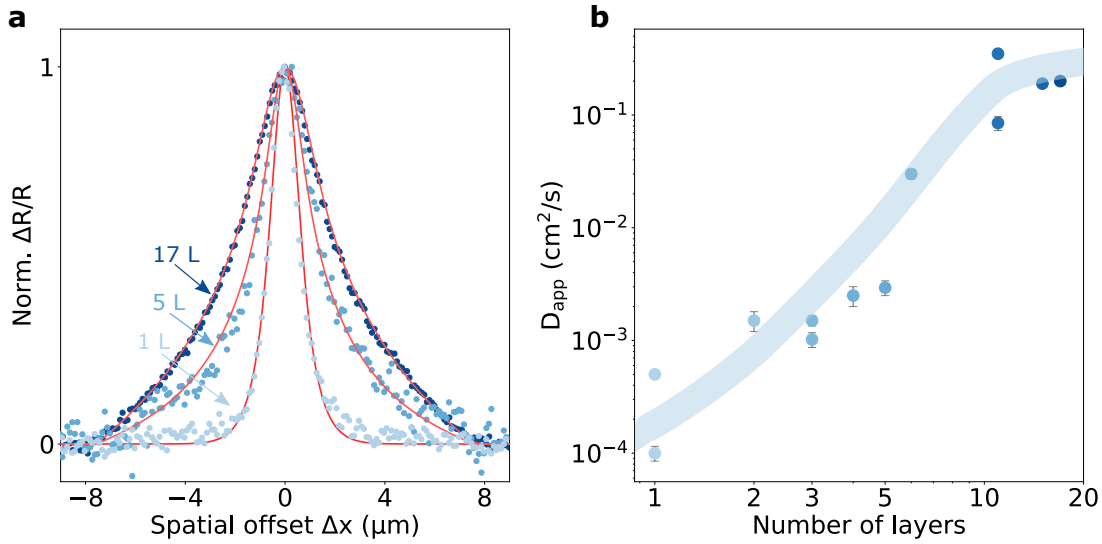


Figure A.1: Transient reflectivity profiles and apparent diffusivity in $MoSe_2$. (a) Normalized (to the peak of the fit) $\Delta R/R$ profiles at $\Delta t = 13$ ns (blue scatters) for $MoSe_2$ sample of three different thicknesses. The solid lines are the fit based on the Fourier model. Pump fluence $f_{\text{pu}} \approx 0.035$ mJ/cm^2. **(b)** Obtained apparent thermal diffusivity over a range of thicknesses. The blue-shaded region is a guide to the eye.

The apparent diffusivity for thin samples notably deviates by orders of magnitude from that of the 20-layer sample and contradicts both literature values [140] and our trends measured using Raman thermometry (see Figure 6.4). This huge decrease in apparent diffusivity is due to the efficient heat transfer of thin $MoSe_2$ flakes to the surrounding atmosphere, resulting in a narrow spatial profile. Similar drastic deviations in thermal properties, becoming more pronounced as the flakes approach the monolayer limit, are also reported in Raman thermometry experiments [74]. These results underscore the critical necessity of conducting thin film heat transport measurements under vacuum conditions to mitigate potential heat transfer to surrounding air molecules.

A4. Measurements in vacuum at f_{mod} = 4.37 kHz

We then proceed to measure the suspended samples under vacuum conditions at the same modulation frequency of 4.37 kHz. Figure A.2a shows decay dynamics of the suspended region for monolayer and bilayer $MoSe_2$ systems.

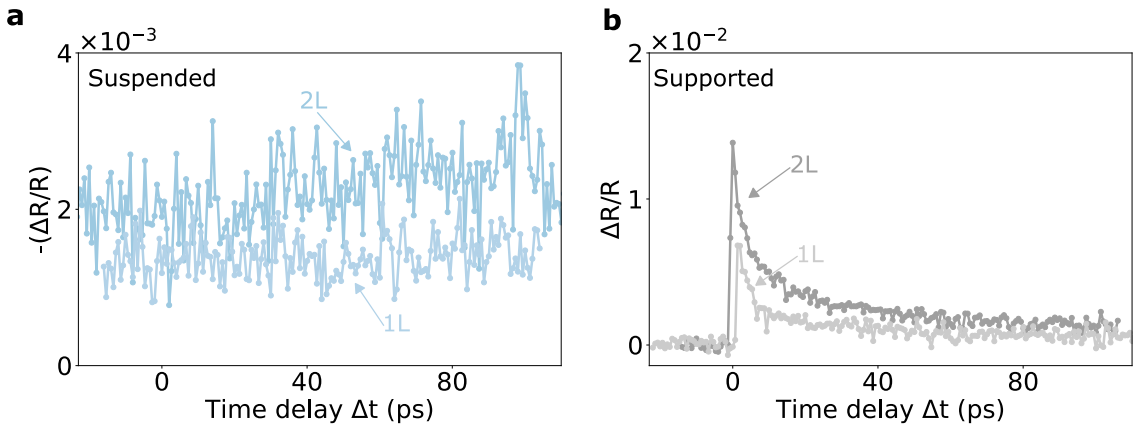


Figure A.2: Decay dynamics in vacuum for $MoSe_2$. **(a)** Temporal dynamics obtained on the suspended region of monolayer and bilayer $MoSe_2$ showing a flat response throughout the delay line. **(b)** Decay dynamics on the supported regions of these samples. Pump fluence $f_{pu} \approx 0.02$ mJ/cm^2.

Interestingly, we don't observe the typical temporal response, with the signal rising at time-zero and gradually decaying, as shown in Figure 5.2, for example. The absence of a sharp rise in the signal at time-zero, combined with the presence of a flat (non-zero) temporal response, indicates that additional heat is permanently present in the system, at least during the pump-on period. The situation occurs when the system has absorbed as much energy as it can from the laser pulses, resulting in a plateau in the response, and indicating that the laser pulses maintain a steady state with a permanently increased temperature. However, we don't see such a flat response from the supported regions, see Figure A.2b. This, as shown before (see Figure 5.2), is because the heat generated by the first pump pulse flows to the substrate and the system reaches equilibrium before the arrival of the next pump pulse.

The spatial profiles on these samples also look considerably different than all the profiles we saw before. We observe a non-monotonous decrease of the transient reflectivity signal from the pump spot, characterized by oscillations in the profiles, for both monolayer and bilayer $MoSe_2$ (see Figure A.3). A possible explanation for this observation could be the overheating of the samples, as in this case, we use about 8700 pump pulses (given by $0.5 \times f_{rep}/f_{mod}$) in a pump-on window. This overheating could result in non-linear effects, such as exciton-halo formation. This occurs at elevated excitation densities, where the initial Gaussian distribution of excitons evolves into long-lived halo shapes. This

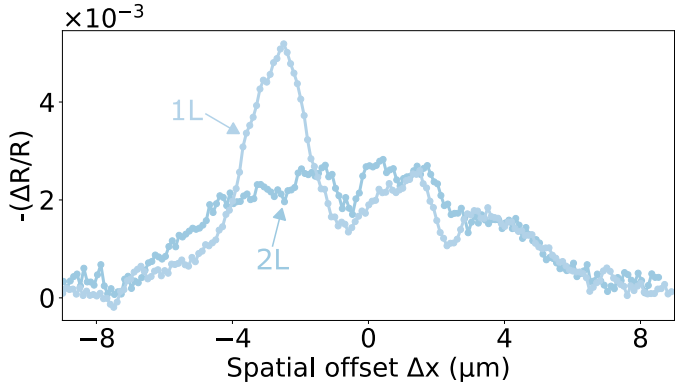


Figure A.3: Spatial profiles in vacuum for $MoSe_2$. Measured spatial profiles (at $\Delta t = 13$ ns) on the suspended regions of monolayer and bilayer $MoSe_2$, showing non-monotonous decay of the signal. Pump fluence $f_{pu} \approx 0.02$ mJ/cm^2.

phenomenon has been observed in WS_2 using time-resolved microphotoluminescence [191]. Importantly, both these results – the flat temporal response and the non-monotonous spatial profiles – suggest that experiments in vacuum at a modulation frequency of 4.37 kHz is not the right measurement configuration for quantifying thermal transport at these thicknesses.

A5. Temporal dynamics of thin $MoSe_2$ flakes

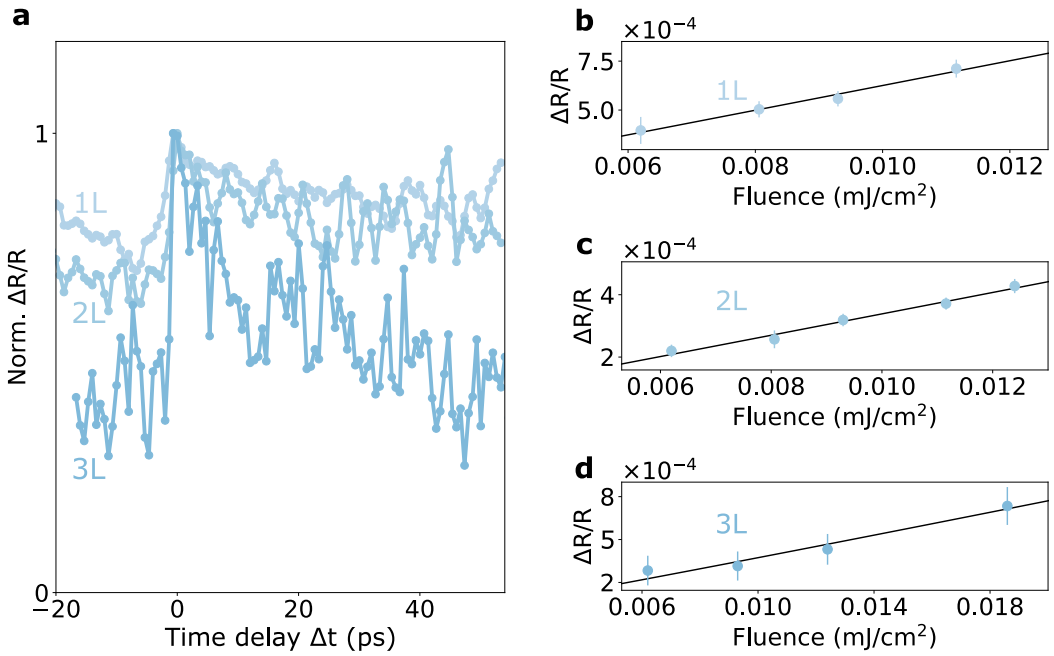


Figure A.4: Decay dynamics and linearity. (a) Normalized decay dynamics on the suspended regions of mono, bi, and trilayer $MoSe_2$. **(b, c, d)** Transient reflectivity signal (at $\Delta t = 13$ ns) plotted against pump fluence demonstrating the linear dependence of the signal. The solid line is a power-law fit to the datasets, yielding the exponent of fit to be around 1.02.

A6. Describing the out-of-phase signal

We also describe the out-of-phase signal using our simulation based on heat diffusion to obtain the in-plane thermal diffusivity D. Figure A.5 shows the out-of-phase profiles along with the fit for 3L to about 20L $MoSe_2$.

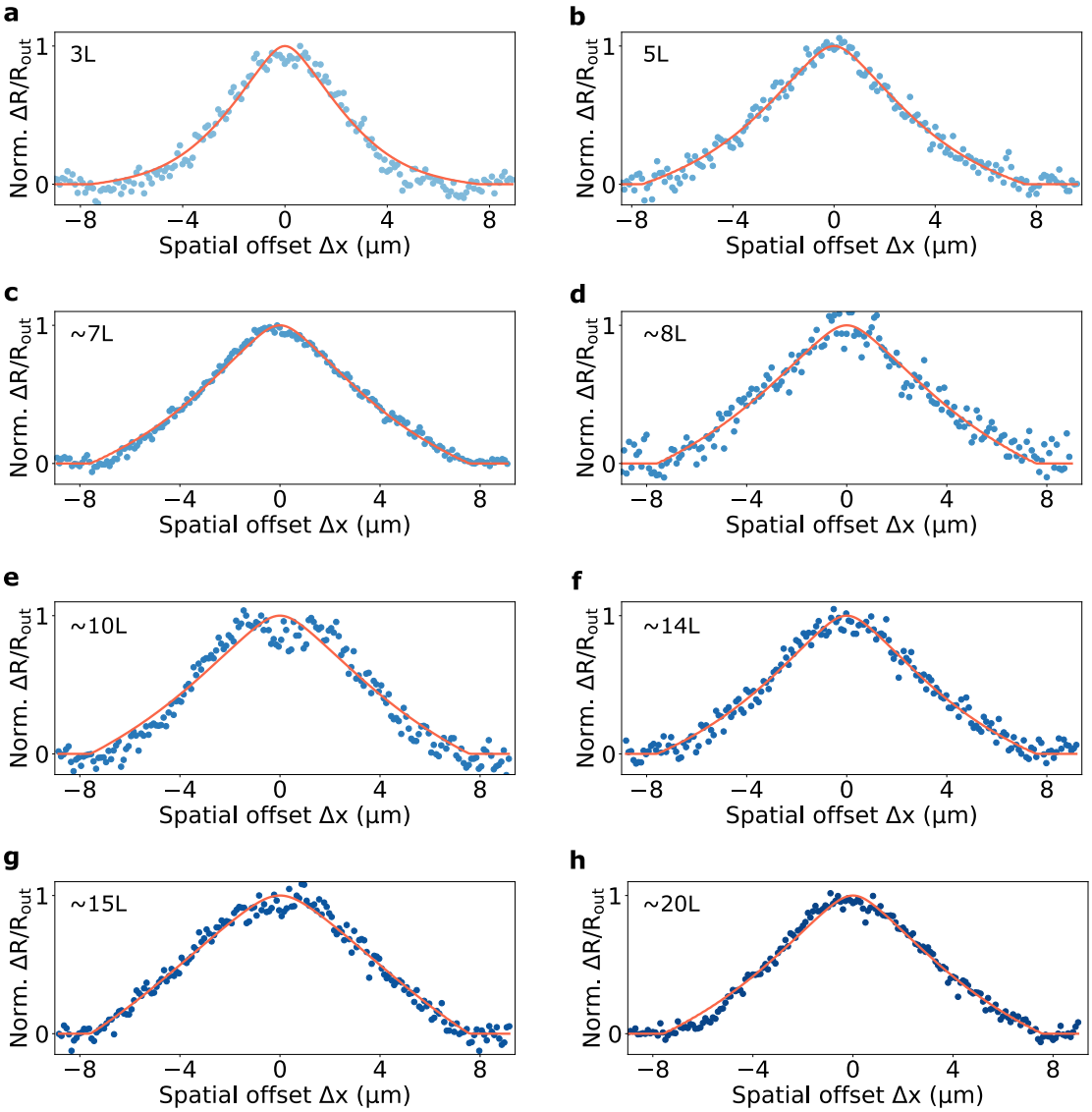


Figure A.5: Out-of-phase spatial profiles in $MoSe_2$. (a-h) Normalized (to the peak of the fit) transient reflectivity signals (out-of-phase) measured on suspended $MoSe_2$ flakes of varying thicknesses (f_{mod} = 240 kHz). The blue scatters represent the experimental datasets, while the solid lines are the fits obtained using the diffusive heat transport model based on Fourier's law. See Figure 7.3 for the in-phase profiles.

We find that the obtained diffusivities align well with our results from Raman thermometry measurements (see Figure A.6). Here, same as our treatment with the in-phase signal, we convert the thermal conductivity κ to D using the following relation: $D = \kappa/C_v$, where

C_v is the heat capacity of bulk $MoSe_2$ from literature [163]. The thermal diffusivity values are very similar to those determined by fitting the in-phase signal (see Figure 7.4).

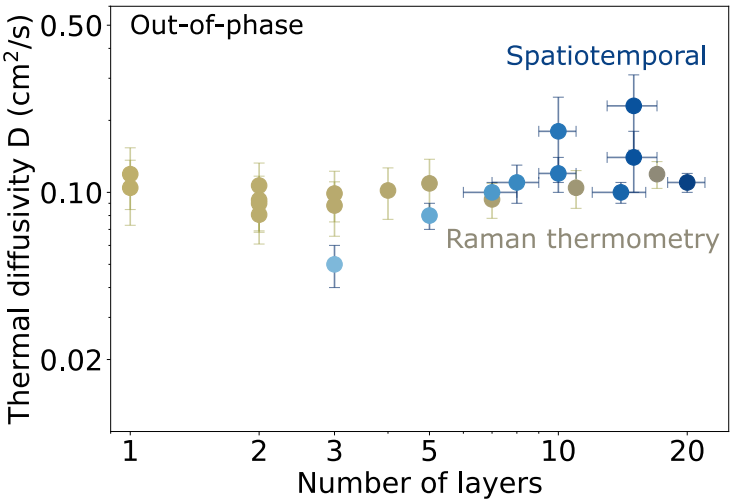


Figure A.6: Comparison with Raman thermometry. Obtained thermal diffusivities (out-of-phase) for $MoSe_2$ from spatiotemporal measurements (blue scatters) and Raman thermometry (yellow-green scatters), as a function of flake thickness.

Acknowledgements

Yes, now we come to the part that everyone actually reads: the acknowledgements. Doing a PhD can often feel quite lonely, especially when you are diving deep into a specialized topic and trying to push the boundaries of knowledge. It involves dealing with a lot of uncertainties, high expectations, and the pressure of deadlines. This can make the PhD journey a challenging one, as I've found out myself. Therefore, I want to thank everyone who supported me through the lows and celebrated the highs.

First and foremost, thank you very much, **Klaas-Jan**, for entrusting me with the opportunity to engage in research. I am immensely thankful for your guidance, patience, and the freedom you granted me. I remember quite a few instances when I told my friends: If Klaas is my supervisor, I could do one more PhD.

Big thanks to **Jake** and **Alexander** for their dedication to teaching, constant support, and willingness to "boss" me around when necessary. Thanks for consistently throwing a life jacket when I felt like drowning.

To **David**, our countless discussions, shared beers, spirited debates, and occasional grievances have left an indelible mark on me. I firmly believe that these experiences pushed us beyond our limits, just as Klaas once said, creating formidable *"four-handed monster"*.

A heartfelt thanks go out to the mechanical workshop team – **Rafa** and **Gustavo**. You both devised simple solutions and fixed many of my technical issues.

To all my previous group members (thanks, **Roberta**, **Michal** and **Afroditi**), and present ones – **Nupur**, **Bohai**, **Ronny**, **Enzo**, **Patricia**, **Loïc**, **Max**, **Bas**, **Francesc**, and **Anand** – your togetherness and support have made this journey immensely fulfilling.

Gratitude extends to individuals outside my immediate circle – **Raúl** for cleanroom assistance, and **Tapas** and **Roque** for our chit-chats in the ICN2 corridors and office. A special mention to the TMB bus service for their excellent support, and to the various AI tools for advancing my knowledge.

Thanks to the guys from the south – **Adara** chechi, **Aishwarya** mol, **Aparna**, **Diya**, **Hussain**, **Jyo** mon, **Namitha**, **Stephy**, **Thomas** chettan, **Vrinda** chechi, and **Sarath** chettan. Many thanks to these three wonderful humans – **Jewel**, **Ashitha**, and **Chitran** – for patiently listening to me for hours. That meant quite a lot to me chicos!

I can't miss this man – **Saptam**; along with David, you made memorable experiences for me (us), both inside and outside the ICN2 campus. I think our company made survival relatively easy for all three!

Finally, my deepest appreciation goes to my parents, whose enormous support and sacrifices have paved the way for my accomplishments. I extend my heartfelt thanks to my brother, his partner, and my loving sister **Anit** for their constant encouragement.

I might have missed names, but if you are here or have received this thesis, you mean something to me, and I – Thank you! Gracias! Dank je wel! നന്ദി!



"No matter how challenging your day has been, every street will eventually lead to the welcoming doors of an Irish pub." - Sebin Varghese

Bibliography

[1] U. Besson, *The history of the cooling law: When the search for simplicity can be an obstacle*, Science & Education **21**, 1085–1110 (2012).

[2] J. B. J. Fourier, *The Analytical Theory of Heat* (The University Press, 1878).

[3] A. Fick, *Ueber diffusion*, Annalen der Physik **170**, 59–86 (1855).

[4] A. K. Krönig, *Grundzüge einer theorie der gase*, Annalen der Physik **175**, 315–322 (1856).

[5] A. Einstein, *Ün the movement of particles suspended in liquids at rest required by the molecular kinetic theory of heat*, Annalen der Physik **4**, 549 (1905).

[6] C. Kittel and P. McEuen, *Introduction to Solid State Physics* (John Wiley & Sons, 2018).

[7] G. Chen, *Non-Fourier phonon heat conduction at the microscale and nanoscale*, Nature Reviews Physics **3**, 555–569 (2021).

[8] J. Maassen and M. Lundstrom, *Steady-state heat transport: Ballistic-to-diffusive with Fourier's law*, Journal of Applied Physics **117**, 035104 (2015).

[9] Y. Guo and M. Wang, *Phonon hydrodynamics and its applications in nanoscale heat transport*, Physics Reports **595**, 1–44 (2015).

[10] K. S. Novoselov, A. K. Geim, S. V. Morozov, D.-e. Jiang, Y. Zhang, S. V. Dubonos, I. V. Grigorieva, and A. A. Firsov, *Electric field effect in atomically thin carbon films*, Science **306**, 666–669 (2004).

[11] J.-H. Chen, C. Jang, S. Xiao, M. Ishigami, and M. S. Fuhrer, *Intrinsic and extrinsic performance limits of graphene devices on SiO_2*, Nature Nanotechnology **3**, 206–209 (2008).

[12] C. Lee, X. Wei, J. W. Kysar, and J. Hone, *Measurement of the elastic properties and intrinsic strength of monolayer graphene*, Science **321**, 385–388 (2008).

[13] A. A. Balandin, S. Ghosh, W. Bao, I. Calizo, D. Teweldebrhan, F. Miao, and C. N. Lau, *Superior thermal conductivity of single-layer graphene*, Nano Letters **8**, 902–907 (2008).

[14] F. Xia, T. Mueller, Y.-m. Lin, A. Valdes-Garcia, and P. Avouris, *Ultrafast graphene photodetector*, Nature Nanotechnology **4**, 839–843 (2009).

[15] F. Koppens, T. Mueller, P. Avouris, A. Ferrari, M. S. Vitiello, and M. Polini, *Photodetectors based on graphene, other two-dimensional materials and hybrid systems*, Nature Nanotechnology **9**, 780–793 (2014).

[16] M. F. El-Kady, V. Strong, S. Dubin, and R. B. Kaner, *Laser scribing of high-performance and flexible graphene-based electrochemical capacitors*, Science **335**, 1326–1330 (2012).

[17] Q. Ke and J. Wang, *Graphene-based materials for supercapacitor electrodes–A review*, Journal of Materiomics **2**, 37–54 (2016).

[18] V. B. Mbayachi, E. Ndayiragije, T. Sammani, S. Taj, E. R. Mbuta, *et al.*, *Graphene synthesis, characterization and its applications: A review*, Results in Chemistry **3**, 100163 (2021).

[19] B. Radisavljevic, A. Radenovic, J. Brivio, V. Giacometti, and A. Kis, *Single-layer MoS_2 transistors*, Nature Nanotechnology **6**, 147–150 (2011).

[20] S. Kim *et al.*, *High-mobility and low-power thin-film transistors based on multilayer MoS_2 crystals*, Nature Communications **3**, 1011 (2012).

[21] K. I. Bolotin, K. Sikes, Z. Jiang, M. Klima, G. Fudenberg, J. Hone, P. Kim, and H. L. Stormer, *Ultrahigh electron mobility in suspended graphene*, Solid State Communications **146**, 351–355 (2008).

[22] A. Splendiani, L. Sun, Y. Zhang, T. Li, J. Kim, C.-Y. Chim, G. Galli, and F. Wang, *Emerging photoluminescence in monolayer MoS_2*, Nano Letters **10**, 1271–1275 (2010).

[23] K. F. Mak, C. Lee, J. Hone, J. Shan, and T. F. Heinz, *Atomically thin MoS_2: a new direct-gap semiconductor*, Physical Review Letters **105**, 136805 (2010).

[24] K. F. Mak and J. Shan, *Photonics and optoelectronics of 2D semiconductor transition metal dichalcogenides*, Nature Photonics **10**, 216–226 (2016).

[25] C. Wang, F. Yang, and Y. Gao, *The highly-efficient light-emitting diodes based on transition metal dichalcogenides: from architecture to performance*, Nanoscale Advances **2**, 4323–4340 (2020).

[26] A. Taffelli, S. Dirè, A. Quaranta, and L. Pancheri, *MoS_2 based photodetectors: a review*, Sensors **21**, 2758 (2021).

[27] G. Wang, A. Chernikov, M. M. Glazov, T. F. Heinz, X. Marie, T. Amand, and B. Urbaszek, *Colloquium: Excitons in atomically thin transition metal dichalcogenides*, Reviews of Modern Physics **90**, 021001 (2018).

[28] A. Srivastava, C. S. P. Tripathi, V. K. Singh, R. R. Srivastava, S. K. Pandey, S. Rai, R. Dutt, and A. K. Patel, *Characterizations of nanoscale two-dimensional materials and heterostructures*, in *2D Nanoscale Heterostructured Materials* (Elsevier, 2020) p. 55–90.

[29] T. N. Theis and H.-S. P. Wong, *The end of Moore's law: A new beginning for information technology*, Computing in science & engineering **19**, 41–50 (2017).

[30] IMEC, *Smaller, better, faster: IMEC presents chip scaling roadmap*, IMEC roadmap (2023).

[31] T. Yamane, S.-i. Katayama, and M. Todoki, *Analysis of ac temperature wave during the measurement of thermal diffusivity of two-layered platelike samples*, Journal of Applied Physics **80**, 2019–2026 (1996).

[32] D. G. Cahill, *Thermal conductivity measurement from 30 to 750 K: the 3ω method*, Review of Scientific Instruments **61**, 802–808 (1990).

[33] P. Kim, L. Shi, A. Majumdar, and P. L. McEuen, *Thermal transport measurements of individual multiwalled nanotubes*, Physical Review Letters **87**, 215502 (2001).

[34] F. Menges, H. Riel, A. Stemmer, C. Dimitrakopoulos, and B. Gotsmann, *Thermal transport into graphene through nanoscopic contacts*, Physical Review Letters **111**, 205901 (2013).

[35] A. El Sachat, F. Könemann, F. Menges, E. Del Corro, J. A. Garrido, C. S. Torres, F. Alzina, and B. Gotsmann, *Crossover from ballistic to diffusive thermal transport in suspended graphene membranes*, 2D Materials **6**, 025034 (2019).

[36] S. Sandell, E. Chávez-Ángel, A. El Sachat, J. He, C. M. Sotomayor Torres, and J. Maire, *Thermoreflectance techniques and Raman thermometry for thermal property characterization of nanostructures*, Journal of Applied Physics **128**, 131101 (2020).

[37] J. S. Reparaz, E. Chávez-Angel, M. R. Wagner, B. Graczykowski, J. Gomis-Bresco, F. Alzina, and S. Torres, *A novel contactless technique for thermal field mapping and*

thermal conductivity determination: two-laser Raman thermometry, Review of Scientific Instruments **85**, 034901 (2014).

[38] H. Malekpour and A. A. Balandin, *Raman-based technique for measuring thermal conductivity of graphene and related materials*, Journal of Raman Spectroscopy **49**, 106–120 (2018).

[39] S. Xu, A. Fan, H. Wang, X. Zhang, and X. Wang, *Raman-based nanoscale thermal transport characterization: A critical review*, International Journal of Heat and Mass Transfer **154**, 119751 (2020).

[40] C. A. Paddock and G. L. Eesley, *Transient thermoreflectance from thin metal films*, Jouranl of Applied Physics **60**, 285–290 (1986).

[41] A. J. Schmidt, R. Cheaito, and M. Chiesa, *A frequency-domain thermoreflectance method for the characterization of thermal properties*, Review of Scientific Instruments **80**, 094901 (2009).

[42] P. Jiang, X. Qian, and R. Yang, *Tutorial: Time-domain thermoreflectance (TDTR) for thermal property characterization of bulk and thin film materials*, Journal of Applied Physics **124**, 205104 (2018).

[43] O. W. Käding, H. Skurk, A. A. Maznev, and E. Matthias, *Transient thermal gratings at surfaces for thermal characterization of bulk materials and thin films*, Applied Physics A **61**, 253–261 (1995).

[44] F. Hofmann, M. P. Short, and C. A. Dennett, *Transient grating spectroscopy: An ultrarapid, nondestructive materials evaluation technique*, MRS Bulletin **44**, 392–402 (2019).

[45] M. Chhowalla, H. S. Shin, G. Eda, L.-J. Li, K. P. Loh, and H. Zhang, *The chemistry of two-dimensional layered transition metal dichalcogenide nanosheets*, Nature Chemistry **5**, 263–275 (2013).

[46] A. Kumar and P. Ahluwalia, *Electronic structure of transition metal dichalcogenides monolayers 1H-MX_2 (M= Mo, W; X= S, Se, Te) from ab-initio theory: new direct band gap semiconductors*, The European Physical Journal B **85**, 1–7 (2012).

[47] P. Tonndorf, R. Schmidt, P. Böttger, X. Zhang, J. Börner, A. Liebig, M. Albrecht, C. Kloc, O. Gordan, D. R. T. Zahn, S. M. de Vasconcellos, and R. Bratschitsch, *Photoluminescence emission and Raman response of monolayer MoS_2, $MoSe_2$, and WSe_2*, Optics Express **21**, 4908–4916 (2013).

[48] E. Malic, R. Perea-Causin, R. Rosati, D. Erkensten, and S. Brem, *Exciton transport in atomically thin semiconductors*, Nature Communications **14**, 3430 (2023).

[49] T. C. Berkelbach, M. S. Hybertsen, and D. R. Reichman, *Theory of neutral and charged excitons in monolayer transition metal dichalcogenides*, Physical Review B **88**, 045318 (2013).

[50] Z. Li, T. Wang, S. Miao, Z. Lian, and S.-F. Shi, *Fine structures of valley-polarized excitonic states in monolayer transitional metal dichalcogenides*, Nanophotonics **9**, 1811–1829 (2020).

[51] K. M. McCreary, A. T. Hanbicki, S. V. Sivaram, and B. T. Jonker, *A-and B-exciton photoluminescence intensity ratio as a measure of sample quality for transition metal dichalcogenide monolayers*, APL Materials **6**, 111106 (2018).

[52] M. Selig, G. Berghäuser, A. Raja, P. Nagler, C. Schüller, T. F. Heinz, T. Korn, A. Chernikov, E. Malic, and A. Knorr, *Excitonic linewidth and coherence lifetime in monolayer transition metal dichalcogenides*, Nature Communications **7**, 13279 (2016).

[53] X. Jiang, Q. Zheng, Z. Lan, W. A. Saidi, X. Ren, and J. Zhao, *Real-time GW-BSE*

investigations on spin-valley exciton dynamics in monolayer transition metal dichalcogenide, Science Advances **7**, eabf3759 (2021).

[54] E. Malic, M. Selig, M. Feierabend, S. Brem, D. Christiansen, F. Wendler, A. Knorr, and G. Berghäuser, *Dark excitons in transition metal dichalcogenides*, Physical Review Materials **2**, 014002 (2018).

[55] T. Mueller and E. Malic, *Exciton physics and device application of two-dimensional transition metal dichalcogenide semiconductors*, npj 2D Materials and Applications **2**, 29 (2018).

[56] Y. Yang, Y. Han, and R. Li, *Raman studies of two-dimensional group-VI transition metal dichalcogenides under extreme conditions*, Crystals **13**, 929 (2023).

[57] W. Parker, R. Jenkins, C. Butler, and G. Abbott, *Flash method of determining thermal diffusivity, heat capacity, and thermal conductivity*, Journal of Applied Physics **32**, 1679–1684 (1961).

[58] J. A. King, *Materials Handbook for Hybrid Microelectronics* (Artech House, 1988).

[59] H. Shanks, P. Maycock, P. Sidles, and G. Danielson, *Thermal conductivity of silicon from 300 to 1400 K*, Physical Review **130**, 1743 (1963).

[60] J. Crank, *The Mathematics of Diffusion* (Oxford University Press, 1979).

[61] J. M. Ziman, *Principles of the Theory of Solids* (Cambridge University Press, 1972).

[62] R. Peierls, *Zur kinetischen theorie der wärmeleitung in kristallen*, Annalen der Physik **395**, 1055–1101 (1929).

[63] L. Boltzmann, *Weitere studien über das wärmegleichgewicht unter gasmolekülen*, Kinetische Theorie II , 115–225 (1970).

[64] B. Vermeersch, J. Carrete, N. Mingo, and A. Shakouri, *Superdiffusive heat conduction in semiconductor alloys. I. theoretical foundations*, Physical Review B **91**, 085202 (2015).

[65] A. J. Minnich, G. Chen, S. Mansoor, and B. Yilbas, *Quasiballistic heat transfer studied using the frequency-dependent Boltzmann transport equation*, Physical Review B **84**, 235207 (2011).

[66] V. Chiloyan, S. Huberman, Z. Ding, J. Mendoza, A. A. Maznev, K. A. Nelson, and G. Chen, *Green's functions of the Boltzmann transport equation with the full scattering matrix for phonon nanoscale transport beyond the relaxation-time approximation*, Physical Review B **104**, 245424 (2021).

[67] L. Sendra, A. Beardo, P. Torres, J. Bafaluy, F. X. Álvarez, and J. Camacho, *Derivation of a hydrodynamic heat equation from the phonon Boltzmann equation for general semiconductors*, Physical Review B **103**, L140301 (2021).

[68] S. Lee, D. Broido, K. Esfarjani, and G. Chen, *Hydrodynamic phonon transport in suspended graphene*, Nature Communications **6**, 6290 (2015).

[69] J. Callaway, *Model for lattice thermal conductivity at low temperatures*, Physical Review **113**, 1046 (1959).

[70] B. K. Agrawal and G. Verma, *Lattice thermal conductivity at low temperatures*, Physical Review **126**, 24 (1962).

[71] J. Ma, W. Li, and X. Luo, *Examining the Callaway model for lattice thermal conductivity*, Physical Review B **90**, 035203 (2014).

[72] N. Malviya and N. K. Ravichandran, *Failure of the Callaway description of heat flow in boron arsenide and boron antimonide driven by phonon scattering selection rules*, Physical Review B **108**, 155201 (2023).

[73] K. Esfarjani, G. Chen, and H. T. Stokes, *Heat transport in silicon from first-principles calculations*, Physical Review B—Condensed Matter and Materials Physics **84**, 085204 (2011).

[74] D. Saleta Reig *et al.*, *Unraveling heat transport and dissipation in suspended $MoSe_2$ from bulk to monolayer*, Advanced Materials **34**, 2108352 (2022).

[75] D. Li, Y. Wu, P. Kim, L. Shi, P. Yang, and A. Majumdar, *Thermal conductivity of individual silicon nanowires*, Applied Physics Letters **83**, 2934–2936 (2003).

[76] R. Kovács and P. Ván, *Generalized heat conduction in heat pulse experiments*, International Journal of Heat and Mass Transfer **83**, 613–620 (2015).

[77] P. Torres, A. Ziabari, A. Torelló, J. Bafaluy, J. Camacho, X. Cartoixà, A. Shakouri, and F. Álvarez, *Emergence of hydrodynamic heat transport in semiconductors at the nanoscale*, Physical Review Materials **2**, 076001 (2018).

[78] A. Beardo, M. Calvo-Schwarzwälder, J. Camacho, T. Myers, P. Torres, L. Sendra, F. Álvarez, and J. Bafaluy, *Hydrodynamic heat transport in compact and holey silicon thin films*, Physical Review Applied **11**, 034003 (2019).

[79] B. McBennett, A. Beardo, E. E. Nelson, B. Abad, T. D. Frazer, A. Adak, Y. Esashi, B. Li, H. C. Kapteyn, M. M. Murnane, and J. L. Knobloch, *Universal behavior of highly confined heat flow in semiconductor nanosystems: From nanomeshes to metalattices*, Nano Letters **23**, 2129–2136 (2023).

[80] H. Casimir, *Note on the conduction of heat in crystals*, Physica **5**, 495–500 (1938).

[81] K. E. Goodson and Y. S. Ju, *Heat conduction in novel electronic films*, Annual Review of Materials Science **29**, 261–293 (1999).

[82] J. Heron, T. Fournier, N. Mingo, and O. Bourgeois, *Mesoscopic size effects on the thermal conductance of silicon nanowire*, Nano Letters **9**, 1861–1865 (2009).

[83] J. A. Johnson, A. Maznev, J. Cuffe, J. K. Eliason, A. J. Minnich, T. Kehoe, C. M. S. Torres, G. Chen, and K. A. Nelson, *Direct measurement of room-temperature nondiffusive thermal transport over micron distances in a silicon membrane*, Physical Review Letters **110**, 25901 (2013).

[84] A. Sood, F. Xiong, S. Chen, R. Cheaito, F. Lian, M. Asheghi, Y. Cui, D. Donadio, K. E. Goodson, and E. Pop, *Quasi-ballistic thermal transport across MoS_2 thin films*, Nano Letters **19**, 2434–2442 (2019).

[85] G. Mahan and F. Claro, *Nonlocal theory of thermal conductivity*, Physical Review B **38**, 1963 (1988).

[86] G. Chen, *Nonlocal and nonequilibrium heat conduction in the vicinity of nanoparticles*, Journal of Heat Transfer **118**, 539–545 (1996).

[87] Y. Hu, L. Zeng, A. J. Minnich, M. S. Dresselhaus, and G. Chen, *Spectral mapping of thermal conductivity through nanoscale ballistic transport*, Nature Nanotechnology **10**, 701–706 (2015).

[88] S. Harris, *An introduction to the Theory of the Boltzmann Equation* (Courier Corporation, 2004).

[89] R. A. Guyer and J. Krumhansl, *Solution of the linearized phonon Boltzmann equation*, Physical Review **148**, 766 (1966).

[90] H. E. Jackson and C. T. Walker, *Thermal conductivity, second sound, and phonon-phonon interactions in NaF*, Physical Review B **3**, 1428 (1971).

[91] A. Smontara, J. C. Lasjaunias, and R. Maynard, *Phonon Poiseuille flow in quasi-one-*

dimensional single crystals, Physical review letters **77**, 5397 (1996).

[92] W. Li, J. Carrete, N. A. Katcho, and N. Mingo, *Shengbte: A solver of the Boltzmann transport equation for phonons*, Computer Physics Communications **185**, 1747–1758 (2014).

[93] S. Huberman, R. A. Duncan, K. Chen, B. Song, V. Chiloyan, Z. Ding, A. A. Maznev, G. Chen, and K. A. Nelson, *Observation of second sound in graphite at temperatures above 100 K*, Science **364**, 375–379 (2019).

[94] R. J. Hardy and D. L. Albers, *Hydrodynamic approximation to the phonon Boltzmann equation*, Physical Review B **10**, 3546 (1974).

[95] Z. Ding, J. Zhou, B. Song, V. Chiloyan, M. Li, T.-H. Liu, and G. Chen, *Phonon hydrodynamic heat conduction and Knudsen minimum in graphite*, Nano letters **18**, 638–649 (2018).

[96] C. T. Lane, H. A. Fairbank, and W. M. Fairbank, *Second sound in liquid helium II*, Physical Review **71**, 600 (1947).

[97] V. Narayanamurti and R. Dynes, *Observation of second sound in bismuth*, Physical Review Letters **28**, 1461 (1972).

[98] H. E. Jackson, C. T. Walker, and T. F. McNelly, *Second sound in NaF*, Physical Review Letters **25**, 26 (1970).

[99] A. Koreeda, R. Takano, and S. Saikan, *Second sound in $SrTiO_3$*, Physical Review Letters **99**, 265502 (2007).

[100] V. Martelli, J. L. Jiménez, M. Continentino, E. Baggio-Saitovitch, and K. Behnia, *Thermal transport and phonon hydrodynamics in strontium titanate*, Physical Review Letters **120**, 125901 (2018).

[101] Y. Machida, A. Subedi, K. Akiba, A. Miyake, M. Tokunaga, Y. Akahama, K. Izawa, and K. Behnia, *Observation of Poiseuille flow of phonons in black phosphorus*, Science Advances **4**, eaat3374 (2018).

[102] X. Huang, Y. Guo, Y. Wu, S. Masubuchi, K. Watanabe, T. Taniguchi, Z. Zhang, S. Volz, T. Machida, and M. Nomura, *Observation of phonon Poiseuille flow in isotopically purified graphite ribbons*, Nature Communications **14**, 2044 (2023).

[103] J. Jeong, X. Li, S. Lee, L. Shi, and Y. Wang, *Transient hydrodynamic lattice cooling by picosecond laser irradiation of graphite*, Physical Review Letters **127**, 085901 (2021).

[104] M.-Y. Shang, C. Zhang, Z. Guo, and J.-T. Lü, *Heat vortex in hydrodynamic phonon transport of two-dimensional materials*, Scientific Reports **10**, 8272 (2020).

[105] A. Cepellotti, G. Fugallo, L. Paulatto, M. Lazzeri, F. Mauri, and N. Marzari, *Phonon hydrodynamics in two-dimensional materials*, Nature Communications **6**, 6400 (2015).

[106] Z. Ding, K. Chen, B. Song, J. Shin, A. A. Maznev, K. A. Nelson, and G. Chen, *Observation of second sound in graphite over 200 K*, Nature Communications **13**, 285 (2022).

[107] R. J. Hardy, *Phonon Boltzmann equation and second sound in solids*, Physical Review B **2**, 1193 (1970).

[108] Y. Guo and M. Wang, *Phonon hydrodynamics for nanoscale heat transport at ordinary temperatures*, Physical Review B **97**, 035421 (2018).

[109] A. Beardo, M. Hennessy, L. Sendra, J. Camacho, T. Myers, J. Bafaluy, and F. Álvarez, *Phonon hydrodynamics in frequency-domain thermoreflectance experiments*, Physical Review B **101**, 075303 (2020).

[110] A. Beardo, J. L. Knobloch, L. Sendra, J. Bafaluy, T. D. Frazer, W. Chao, J. N. Hernandez-Charpak, H. C. Kapteyn, B. Abad, M. M. Murnane, F. X. Álvarez, and J. Camacho,

A general and predictive understanding of thermal transport from 1D-and 2D-confined nanostructures: Theory and experiment, ACS Nano **15**, 13019–13030 (2021).

[111] S. Alajlouni, A. Beardo, L. Sendra, A. Ziabari, J. Bafaluy, J. Camacho, Y. Xuan, F. X. Álvarez, and A. Shakouri, *Geometrical quasi-ballistic effects on thermal transport in nanostructured devices*, Nano Research **14**, 945–952 (2021).

[112] Z. Xiang, P. Jiang, and R. Yang, *Time-domain thermoreflectance (TDTR) data analysis using phonon hydrodynamic model*, Journal of Applied Physics **132**, 205104 (2022).

[113] A. Ruiz-Clavijo, O. Caballero-Calero, C. V. Manzano, X. Maeder, A. Beardo, X. Cartoixà, F. X. Álvarez, and M. Martín-González, *3D Bi_2Te_3 interconnected nanowire networks to increase thermoelectric efficiency*, ACS Applied Energy Materials **4**, 13556–13566 (2021).

[114] A. Ziabari, P. Torres, B. Vermeersch, Y. Xuan, X. Cartoixà, A. Torelló, J.-H. Bahk, Y. R. Koh, M. Parsa, P. D. Ye, F. X. Álvarez, and A. Shakouri, *Full-field thermal imaging of quasiballistic crosstalk reduction in nanoscale devices*, Nature Communications **9**, 255 (2018).

[115] A. Beardo *et al.*, *Observation of second sound in a rapidly varying temperature field in Ge*, Science Advances **7**, eabg4677 (2021).

[116] S. Varghese, D. S. Reig, J. D. Mehew, A. Block, A. E. Sachat, E. Chávez-Ángel, M. Sledzinska, B. Ballesteros, C. M. S. Torres, and K.-J. Tielrooij, *Fabrication and characterization of large-area suspended $MoSe_2$ crystals down to the monolayer*, Journal of Physics: Materials **4**, 046001 (2021).

[117] T. Ando, *Screening effect and impurity scattering in monolayer graphene*, Journal of the Physical Society of Japan **75**, 074716 (2006).

[118] M. L. Trolle, T. G. Pedersen, and V. Véniard, *Model dielectric function for 2D semiconductors including substrate screening*, Scientific Reports **7**, 39844 (2017).

[119] X.-L. Li, W.-P. Han, J.-B. Wu, X.-F. Qiao, J. Zhang, and P.-H. Tan, *Layer-number dependent optical properties of 2D materials and their application for thickness determination*, Advanced Functional Materials **27**, 1604468 (2017).

[120] A. Principi, M. B. Lundeberg, N. C. Hesp, K.-J. Tielrooij, F. H. Koppens, and M. Polini, *Super-planckian electron cooling in a van der waals stack*, Physical Review Letters **118**, 126804 (2017).

[121] S. Lippert *et al.*, *Influence of the substrate material on the optical properties of tungsten diselenide monolayers*, 2D Materials **4**, 025045 (2017).

[122] Y. Zhang, Q. Lv, A. Fan, L. Yu, H. Wang, W. Ma, R. Lv, and X. Zhang, *Reduction in thermal conductivity of monolayer WS_2 caused by substrate effect*, Nano Research **15**, 9578–9587 (2022).

[123] Y. Sun, R. Wang, and K. Liu, *Substrate induced changes in atomically thin 2-dimensional semiconductors: Fundamentals, engineering, and applications*, Applied Physics Reviews **4** (2017), 10.1063/1.4974072.

[124] A. Castellanos-Gomez, M. Buscema, R. Molenaar, V. Singh, L. Janssen, H. S. Van Der Zant, and G. A. Steele, *Deterministic transfer of two-dimensional materials by all-dry viscoelastic stamping*, 2D Materials **1**, 011002 (2014).

[125] R. Frisenda, E. Navarro-Moratalla, P. Gant, D. P. De Lara, P. Jarillo-Herrero, R. V. Gorbachev, and A. Castellanos-Gomez, *Recent progress in the assembly of nanodevices and van der waals heterostructures by deterministic placement of 2D materials*, Chemical Society Reviews **47**, 53–68 (2018).

[126] S. B. Desai *et al.*, *Gold-mediated exfoliation of ultralarge optoelectronically-perfect monolayers*, Advanced Materials **28**, 4053–4058 (2016).

[127] D. Bing, Y. Wang, J. Bai, R. Du, G. Wu, and L. Liu, *Optical contrast for identifying the thickness of two-dimensional materials*, Optics Communications **406**, 128–138 (2018).

[128] C. A. Schneider, W. S. Rasband, and K. W. Eliceiri, *NIH Image to ImageJ: 25 years of image analysis*, Nature Methods **9**, 671–675 (2012).

[129] F. Crameri, G. E. Shephard, and P. J. Heron, *The misuse of colour in science communication*, Nature Communications **11**, 5444 (2020).

[130] Y. Sun, D. Wang, and Z. Shuai, *Indirect-to-direct band gap crossover in few-layer transition metal dichalcogenides: a theoretical prediction*, The Journal of Physical Chemistry C **120**, 21866–21870 (2016).

[131] D. Nečas and P. Klapetek, *Gwyddion: an open-source software for SPM data analysis*, Central European Journal of Physics **10**, 181 (2012).

[132] S. J. Cartamil-Bueno, M. Cavalieri, R. Wang, S. Houri, S. Hofmann, and H. S. J. van der Zant, *Mechanical characterization and cleaning of CVD single-layer h-BN resonators*, npj 2D Materials and Applications **1**, 16 (2017).

[133] C. Palacios-Berraquero, D. M. Kara, A. R.-P. Montblanch, M. Barbone, P. Latawiec, D. Yoon, A. K. Ott, M. Loncar, A. C. Ferrari, and M. Atatüre, *Large-scale quantum-emitter arrays in atomically thin semiconductors*, Nature Communications **8**, 15093 (2017).

[134] V. Babacic, D. Saleta Reig, S. Varghese, T. Vasileiadis, E. Coy, K.-J. Tielrooij, and B. Graczykowski, *Thickness-dependent elastic softening of few-layer free-standing $MoSe_2$*, Advanced Materials **33**, 2008614 (2021).

[135] Z. Chen, H. Liu, X. Chen, G. Chu, S. Chu, and H. Zhang, *Wafer-size and single-crystal $MoSe_2$ atomically thin films grown on gan substrate for light emission and harvesting*, ACS Applied Materials & Interfaces **8**, 20267–20273 (2016).

[136] S. Larentis, B. Fallahazad, and E. Tutuc, *Field-effect transistors and intrinsic mobility in ultra-thin $MoSe_2$ layers*, Applied Physics Letters **101**, 223104 (2012).

[137] S. Horzum, H. Sahin, S. Cahangirov, P. Cudazzo, A. Rubio, T. Serin, and F. M. Peeters, *Phonon softening and direct to indirect band gap crossover in strained single-layer $MoSe_2$*, Physical Review B **87**, 125415 (2013).

[138] Y. Niu *et al.*, *Thickness-dependent differential reflectance spectra of monolayer and few-layer MoS_2, $MoSe_2$, WS_2 and WSe_2*, Nanomaterials **8**, 725 (2018).

[139] H. Arwin, M. Poksinski, and K. Johansen, *Total internal reflection ellipsometry: principles and applications*, Applied Optics **43**, 3028–3036 (2004).

[140] X. Zhang, D. Sun, Y. Li, G.-H. Lee, X. Cui, D. Chenet, Y. You, T. F. Heinz, and J. C. Hone, *Measurement of lateral and interfacial thermal conductivity of single-and bilayer MoS_2 and $MoSe_2$ using refined optothermal Raman technique*, ACS Applied Materials & Interfaces **7**, 25923–25929 (2015).

[141] A. R. Beal, J. C. Knights, and W. Y. Liang, *Transmission spectra of some transition metal dichalcogenides. II. Group VIA: trigonal prismatic coordination*, Journal of Physics C **5**, 3540 (1972).

[142] N. Dong, Y. Li, Y. Feng, S. Zhang, X. Zhang, C. Chang, J. Fan, L. Zhang, and J. Wang, *Optical limiting and theoretical modelling of layered transition metal dichalcogenide nanosheets*, Scientific Reports **5**, 14646 (2015).

[143] W. Zhao, Z. Ghorannevis, L. Chu, M. Toh, C. Kloc, P.-H. Tan, and G. Eda, *Evolution*

of electronic structure in atomically thin sheets of WS_2 and WSe_2, ACS Nano **7**, 791–797 (2013).

[144] R. Frisenda, Y. Niu, P. Gant, A. J. Molina-Mendoza, R. Schmidt, R. Bratschitsch, J. Liu, L. Fu, D. Dumcenco, A. Kis, D. Perez De Lara, and A. Castellanos-Gomez, *Micro-reflectance and transmittance spectroscopy: a versatile and powerful tool to characterize 2D materials*, Journal of Physics D **50**, 074002 (2017).

[145] G. D. B. Vazquez, G. L. G. Morganti, A. Block, N. F. van Hulst, M. Liebel, and K.-J. Tielrooij, *Spatiotemporal microscopy: Shining light on transport phenomena*, Advanced Electronic Materials **10**, 2300584 (2024).

[146] J. Li, J. Lu, A. Chew, S. Han, J. Li, Y. Wu, H. Wang, S. Ghimire, and Z. Chang, *Attosecond science based on high harmonic generation from gases and solids*, Nature Communications **11**, 2748 (2020).

[147] A. Block, *Quantifying nanoscale carrier diffusion with ultrafast optical and photocurrent microscopy* (PhD Thesis, Universitat Politècnica de Catalunya, 2019).

[148] Y. Suzaki and A. Tachibana, *Measurement of the μm sized radius of Gaussian laser beam using the scanning knife-edge*, Applied Optics **14**, 2809–2810 (1975).

[149] S. Sundaram and E. Mazur, *Inducing and probing non-thermal transitions in semiconductors using femtosecond laser pulses*, Nature Materials **1**, 217–224 (2002).

[150] M. Wahl, *Time-Correlated Single Photon Counting*, Tech. Rep. (PicoQuant GmbH, 2009).

[151] J. W. Goodman, *Introduction to Fourier Optics* (Roberts and Company publishers, 2005).

[152] R. Paschotta, *ABCD matrix*, RP Photonics Encyclopedia (Accessed July 2024), Available online at RP Photonics Encyclopedia.

[153] A. Block, M. Liebel, R. Yu, M. Spector, Y. Sivan, F. García de Abajo, and N. F. van Hulst, *Tracking ultrafast hot-electron diffusion in space and time by ultrafast thermomodulation microscopy*, Science Advances **5**, eaav8965 (2019).

[154] M. Segovia and X. Xu, *High accuracy ultrafast spatiotemporal pump–probe measurement of electrical thermal transport in thin film gold*, Nano Letters **21**, 7228–7235 (2021).

[155] S. Varghese, J. D. Mehew, A. Block, D. S. Reig, P. Woźniak, R. Farris, Z. Zanolli, P. Ordejón, M. J. Verstraete, N. F. van Hulst, and K.-J. Tielrooij, *A pre-time-zero spatiotemporal microscopy technique for the ultrasensitive determination of the thermal diffusivity of thin films*, Review of Scientific Instruments **94**, 034903 (2023).

[156] H. Wang and M. Sen, *Analysis of the 3-omega method for thermal conductivity measurement*, International Journal of Heat and Mass Transfer **52**, 2102–2109 (2009).

[157] L. Shi, D. Li, C. Yu, W. Jang, D. Kim, Z. Yao, P. Kim, and A. Majumdar, *Measuring thermal and thermoelectric properties of one-dimensional nanostructures using a microfabricated device*, Journal of Heat and Mass Transfer **125**, 881–888 (2003).

[158] N. Kumar, Q. Cui, F. Ceballos, D. He, Y. Wang, and H. Zhao, *Exciton diffusion in monolayer and bulk MoS_2*, Nanoscale **6**, 4915–4919 (2014).

[159] Q. Cui, F. Ceballos, N. Kumar, and H. Zhao, *Transient absorption microscopy of monolayer and bulk WSe_2*, ACS Nano **8**, 2970–2976 (2014).

[160] M.-F. Lin, V. Kochat, A. Krishnamoorthy, L. Bassman Oftelie, C. Weninger, Q. Zheng, X. Zhang, A. Apte, C. S. Tiwary, X. Shen, *et al.*, *Ultrafast non-radiative dynamics of atomically thin $MoSe_2$*, Nature Communications **8**, 1745 (2017).

[161] N. B. Mohamed, H. E. Lim, F. Wang, S. Koirala, S. Mouri, K. Shinokita, Y. Miyauchi, and K. Matsuda, *Long radiative lifetimes of excitons in monolayer transition-metal dichalco-*

genides MX_2 (M= Mo, W; X= S, Se), Applied Physics Express **11**, 015201 (2017).

[162] A. Beal and H. Hughes, *Kramers-kronig analysis of the reflectivity spectra of 2H-MoS_2, 2H-$MoSe_2$ and 2H-$MoTe_2$*, Journal of Physics C: Solid State Physics **12**, 881 (1979).

[163] A. Blinder, A. Bolgar, and Z. A. Trofimova, *Thermodynamic properties of selenides of transition metals*, Powder metallurgy and metal ceramics **32**, 234–239 (1993).

[164] P. O'hare, W. Hubbard, G. Johnson, and H. Flotow, *Calorimetric measurements of the low-temperature heat capacity, standard molar enthalpy of formation at 298.15 K, and high-temperature molar enthalpy increments relative to 298.15 K of tungsten disulfide (WS_2), and the thermodynamic properties to 1500 K*, The Journal of Chemical Thermodynamics **16**, 45–59 (1984).

[165] P. Jiang, X. Qian, X. Gu, and R. Yang, *Probing anisotropic thermal conductivity of transition metal dichalcogenides MX_2 (M= Mo, W and X= S, Se) using time-domain thermoreflectance*, Advanced Materials **29**, 1701068 (2017).

[166] H. Zobeiri, R. Wang, T. Wang, H. Lin, C. Deng, and X. Wang, *Frequency-domain energy transport state-resolved Raman for measuring the thermal conductivity of suspended nm-thick $MoSe_2$*, International Journal of Heat and Mass Transfer **133**, 1074–1085 (2019).

[167] J. Liu, G.-M. Choi, and D. G. Cahill, *Measurement of the anisotropic thermal conductivity of molybdenum disulfide by the time-resolved magneto-optic kerr effect*, Journal of Applied Physics **116**, 233107 (2014).

[168] P. Yuan, R. Wang, T. Wang, X. Wang, and Y. Xie, *Nonmonotonic thickness-dependence of in-plane thermal conductivity of few-layered MoS_2: 2.4 to 37.8 nm*, Physical Chemistry Chemical Physics **20**, 25752–25761 (2018).

[169] R. Wang, T. Wang, H. Zobeiri, P. Yuan, C. Deng, Y. Yue, S. Xu, and X. Wang, *Measurement of the thermal conductivities of suspended MoS_2 and $MoSe_2$ by nanosecond ET-Raman without temperature calibration and laser absorption evaluation*, Nanoscale **10**, 23087–23102 (2018).

[170] A. Pisoni, J. Jacimovic, R. Gaál, B. Náfrádi, H. Berger, Z. Révay, and L. Forró, *Anisotropic transport properties of tungsten disulfide*, Scripta Materialia **114**, 48–50 (2016).

[171] L. Volovik, V. Fesenko, A. Bolgar, S. Drozdova, L. Klochkov, and V. Primachenko, *Enthalpy and heat capacity of molybdenum disulfide*, Soviet Powder Metallurgy and Metal Ceramics **17**, 697–702 (1978).

[172] D. O. Lindroth and P. Erhart, *Thermal transport in van der Waals solids from first-principles calculations*, Physical Review B **94**, 115205 (2016).

[173] A. A. Balandin, S. Ghosh, W. Bao, I. Calizo, D. Teweldebrhan, F. Miao, and C. N. Lau, *Superior thermal conductivity of single-layer graphene*, Nano Letters **8**, 902–907 (2008).

[174] K. Xu, J. Guo, G. Raciti, A. R. Goni, M. I. Alonso, X. Borrisé, I. Zardo, M. Campoy-Quiles, and J. S. Reparaz, *In-plane thermal diffusivity determination using beam-offset frequency-domain thermoreflectance with a one-dimensional optical heat source*, International Journal of Heat and Mass Transfer **214**, 124376 (2023).

[175] X. Xu, L. F. Pereira, Y. Wang, J. Wu, K. Zhang, X. Zhao, S. Bae, C. T. Bui, R. Xie, J. T. Thong, B. Hee Hong, K. Ping Loh, D. Donadio, B. Li, and B. Özyilmaz, *Length-dependent thermal conductivity in suspended single-layer graphene*, Nature Communications **5**, 3689 (2014).

[176] S. Varghese, J. D. Mehew, H. I. Wang, M. Wuttke, Y. Zhou, K. Müllen, A. Narita, A. W. Cummings, and K.-J. Tielrooij, *Ultrafast charge and exciton diffusion in monolayer films of 9-armchair graphene nanoribbons*, Under Review (2024).

[177] Y. Zhao, Y. Cai, L. Zhang, B. Li, G. Zhang, and J. T. Thong, *Thermal transport in 2D semiconductors—considerations for device applications*, Advanced Functional Materials **30**, 1903929 (2020).

[178] E. Easy, Y. Gao, Y. Wang, D. Yan, S. M. Goushehgir, E.-H. Yang, B. Xu, and X. Zhang, *Experimental and computational investigation of layer-dependent thermal conductivities and interfacial thermal conductance of one-to three-layer WSe_2*, ACS Applied Materials & Interfaces **13**, 13063–13071 (2021).

[179] J. J. Bae, H. Y. Jeong, G. H. Han, J. Kim, H. Kim, M. S. Kim, B. H. Moon, S. C. Lim, and Y. H. Lee, *Thickness-dependent in-plane thermal conductivity of suspended MoS_2 grown by chemical vapor deposition*, Nanoscale **9**, 2541–2547 (2017).

[180] B. Peng, H. Zhang, H. Shao, Y. Xu, X. Zhang, and H. Zhu, *Thermal conductivity of monolayer MoS_2, $MoSe_2$, and WS_2: interplay of mass effect, interatomic bonding and anharmonicity*, RSC advances **6**, 5767–5773 (2016).

[181] X. Gu and R. Yang, *Phonon transport in single-layer transition metal dichalcogenides: A first-principles study*, Applied Physics Letters **105**, 131903 (2014).

[182] W. Cai, A. L. Moore, Y. Zhu, X. Li, S. Chen, L. Shi, and R. S. Ruoff, *Thermal transport in suspended and supported monolayer graphene grown by chemical vapor deposition*, Nano Letters **10**, 1645–1651 (2010).

[183] S. Chen *et al.*, *Raman measurements of thermal transport in suspended monolayer graphene of variable sizes in vacuum and gaseous environments*, ACS Nano **5**, 321–328 (2011).

[184] A. García *et al.*, *SIESTA: Recent developments and applications*, The Journal of Chemical Physics **152**, 204108 (2020).

[185] S. Ghosh, W. Bao, D. L. Nika, S. Subrina, E. P. Pokatilov, C. N. Lau, and A. A. Balandin, *Dimensional crossover of thermal transport in few-layer graphene*, Nature Materials **9**, 555–558 (2010).

[186] R. Farris, O. Hellman, Z. Zanolli, D. Saleta Reig, S. Varghese, P. Ordejón, K.-J. Tielrooij, and M. J. Verstraete, *Microscopic understanding of the in-plane thermal transport properties of 2H transition metal dichalcogenides*, Physical Review B **109**, 125422 (2024).

[187] R. J. Dolleman, D. Lloyd, M. Lee, J. S. Bunch, H. S. Van Der Zant, and P. G. Steeneken, *Transient thermal characterization of suspended monolayer MoS_2*, Physical Review Materials **2**, 114008 (2018).

[188] X. Hu, P. Yasaei, J. Jokisaari, S. Öğüt, A. Salehi-Khojin, and R. F. Klie, *Mapping thermal expansion coefficients in freestanding 2D materials at the nanometer scale*, Physical Review Letters **120**, 055902 (2018).

[189] R. Kronig, *On the hydrodynamics of non-viscous fluids and the theory of helium ii. part III*, Physica **19**, 535–544 (1953).

[190] L. Yang, S. Yue, Y. Tao, S. Qiao, H. Li, Z. Dai, B. Song, Y. Chen, J. Du, D. Li, and P. Gao, *Suppressed thermal transport in silicon nanoribbons by inhomogeneous strain*, Nature **629**, 1021–1026 (2024).

[191] M. Kulig, J. Zipfel, P. Nagler, S. Blanter, C. Schüller, T. Korn, N. Paradiso, M. M. Glazov, and A. Chernikov, *Exciton diffusion and halo effects in monolayer semiconductors*, Physical review letters **120**, 207401 (2018).

Curriculum Vitae



Born on January 5, 1996, in Ambunadu, Kerala, India, Sebin Varghese completed his Bachelor's degree in Physics in 2016 from Union Christian College, Cochin, and earned a Master's degree in Applied Physics in 2018 from Mahatma Gandhi University, Kottayam, where his thesis focused on light-matter interaction in graphene oxide thin films. In May 2019, he joined the Ultrafast Dynamics in Nanoscale Systems group at the Catalan Institute of Nanoscience and Nanotechnology in Barcelona as a research assistant, and by September 2019, he began his PhD as the group's first PhD student. His research involved studying the heat transport properties of layered materials using a novel spatiotemporal pump-probe thermometry technique and Raman thermometry.